Chapter 1: Introduction

Surface active agents (Surfactants) are molecules with a hydrophilic part called the head group and a hydrophobic part, called the tail. The head group may be ionic, zwitterionic or nonionic, while the tail is typically a linear hydrocarbon 10 to 18 carbons long. Examples of common, conventional surfactants are given in Figure 1.1. In recent years novel forms of surfactants consisting of two conventional surfactants joined chemically at the head group have generated much interest.[1-4] These surfactants, called gemini (or dimeric) surfactants, display enhanced surface activity and lower critical micelle concentrations,[1-4] which are desirable properties for many industrial applications.

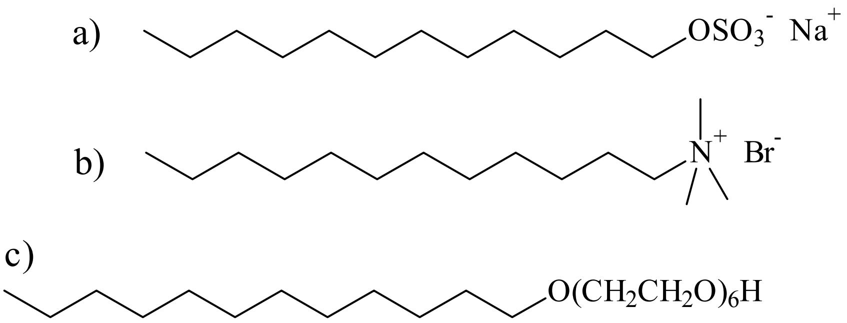

Figure 1.1: Examples of conventional surfactants, a) anionic surfactant sodium dodecyl sulphate (SDS), b) cationic surfactant dodecyl trimethyl ammonium bromide (DTAB) and c) nonionic surfactant hexaethylene glycol monododecyl ether ($C_{12}E_6$).

The original motivation for this project was the application of novel surfactant technology to emulsion polymerisation, specifically for the production of acrylic paints, during which surfactants serve the dual purpose of stabilising the emulsion and the polymer latex. The aim of industrial researchers in this field is to improve the properties of paints by reducing the amount of surfactant used whilst maintaining the same degree of stabilisation. However, reducing the amount of surfactant in paints is not the main aim of this thesis. In fact, the blind application of novel surfactant technology, without understanding its fundamental physical chemistry, can work against this goal.

The aim of this project was to study the physical chemistry of a series of nonionic gemini surfactants with possible applications to the paint industry. More specifically the aims are:

i. the systematic study of the solution properties of a series of nonionic gemini surfactants and

ii. comparison of their properties with conventional surfactants.

This second aim is especially important in determining the nature and extent of any advantage of gemini surfactants over conventional surfactants for industrial applications.

1.1 Conventional surfactant Behaviour

When dispersed in aqueous solution surfactants adsorb at interfaces and self-assemble in bulk solution. Adsorption is the concentration of surfactants at an interface, while self-assembly is the aggregation of surfactants into structures called micelles. Both these processes are driven by the hydrophobic tails being expelled from solution. For example, adsorption at the air/solution interface occurs when the tails are driven from solution into air with the head groups remain in solution, whilst in micelle formation the tails are driven together into a hydrophobic “core” with the head groups again remaining in solution.

Adsorption lowers interfacial tension making it useful for many industrial applications such as detergency and emulsification. It also stabilises colloidal interfaces making it useful in applications such as flotation and foaming. Micelles in contrast can dissolve water insoluble molecules, such as oil, in the micelle core (a process called solubilization), which is used industrially in many applications such as detergent formulations and shampoos.

1.2 The Critical Micelle Concentration

Micelles only form above a characteristic concentration called the Critical Micelle Concentration (CMC). Below the CMC surfactants exist as separate molecules (or monomers). At the CMC the concentration of surfactant as monomers becomes approximately constant and all additional surfactant added forms micelles.

The CMC is the most widely studied quantity of surfactants,[5] due to its usefulness. This is because micelles first form at the CMC and adsorption reaches its maximum. For applications using adsorption the concentration should be less than or slightly above the CMC to prevent surfactant wastage. For applications requiring micelles the concentration should be much greater than the CMC to ensure a sufficient concentration of micelles.

The value of the CMC depends on the surfactant structure, especially the tail. Because the driving force for self-assembly is the hydrophobic effect, more hydrophobic tails produce lower CMCs. Thus, surfactants with hexadecyl tails ($C_{16}H_{33}$) have much lower CMCs than surfactants with much less hydrophobic dodecyl tails ($C_{12}H_{25}$).[6]

In contrast, the head group opposes micelle formation because it is energetically favourable for them to remain in solution than be forced together in micelles. As a general rule ionic surfactants have much higher CMCs than nonionic surfactants. For example, the CMC of SDS (Figure 1.1) is ~8 mM,[5] compared with 0.8 mM for $C_{12}E_6$.[5] Although the hydrophobic tail is the same for both these surfactants, the CMCs are one order of magnitude different.

1.3 Gemini surfactants

Nonionic surfactants were chosen for this project because of the extensive use of conventional nonionic surfactants in industry.[7] Gemini surfactants where chosen because of their low CMCs and enhanced surface activity reported in the literature.[1-4]

Direct comparison between gemini and conventional surfactants is made by considering gemini surfactant as two conventional surfactants joined together. For example, CMCs are compared by expressing all concentrations in moles of tail per litre, rather than moles of surfactant per litre.[8] That is, for there to be an advantage the CMC must form at less than half the conventional surfactant CMC when expressed in conventional molar units.

The majority of gemini surfactant studies have been on ionic systems. In particular, gemini surfactants have been based on the conventional alkyl trimethylammonium bromide and chloride surfactants. Although nonionic gemini surfactants have also been studied they typically contain atoms in the tail that prevent easy comparison to conventional surfactants. Further, the majority of studies have concentrated on synthesis and the physical chemistry is typically not explored in detail.

With these considerations in mind the surfactants synthesised for this work were nonionic gemini surfactants with a purely hydrocarbon tail and spacer, and with polyethylene oxide head groups. The purely hydrocarbon moiety allows much easier comparison to conventional nonionic surfactants with linear hydrocarbon tails, which have been studied extensively. The polyethylene oxide head groups have been synthesised with varying degrees of polymerisation to allow the systematic study of properties as a function of head group size. Their structure is represented in Figure 1.2 and will be described in more detail in the next chapter.

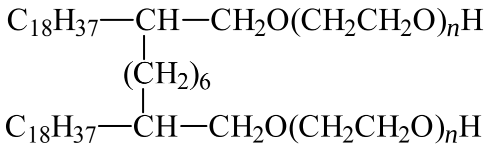

$$\begin{array}{l} C_{18}H_{37}\text{—}\underset{|}{C}H\text{—}CH_2O(CH_2CH_2O)_nH \\ \qquad\quad\;\; (CH_2)_6 \\ C_{18}H_{37}\text{—}\overset{|}{C}H\text{—}CH_2O(CH_2CH_2O)_nH \end{array}$$

Figure 1.2: Nonionic gemini surfactants used in this work.

1.4 Organization of this thesis

This thesis is organised into four main sections: Introduction (Chapter 2), Experimental Methods (Chapter 3), Results and Discussion (Chapters 4–6), and Conclusions (Chapter 7). The Introduction is a basic review of surfactant behaviour and gemini surfactants. It also includes current theories of self-assembly, the phase behaviour of surfactants and the thermodynamics of micelle formation that will be used later. The Materials and Methods section contains a brief summary of the theories, limitations and experimental techniques used for this project, leaving the results and discussion sections free for the presentation and interpretation of experimental results.

The Results and Discussion sections concentrate on micelle and mesophase formation with comparison to the behaviour of conventional nonionic surfactants. Chapter 3 deals with the CMCs in raw and mixed surfactant systems. Chapter 4 deals with the morphology of nonionic gemini surfactant micelles in dilute solution. Chapter 5 deals with the behaviour of the gemini surfactants as a function of concentration and temperature, especially when micelle concentrations become large enough that micelle interactions significantly affect the macroscopic properties of solutions. Finally, the Conclusions chapter reiterates the main results and makes a final comparison between conventional nonionic and gemini nonionic surfactants.

Chapter 2: Solution Behaviour of Surfactants

2.1 Nonionic Gemini Surfactants

Gemini surfactants, as mentioned previously, are two conventional surfactants joined chemically together. More commonly, they are surfactants with two head groups and two tails; a chemical linker is not always necessary. Gemini surfactants have created great interest mainly because of their low CMCs and enhanced surface tension reducing ability. For both of these properties, studies have even shown synergism in special cases between ionic gemini surfactants and some conventional surfactants,[9-13] where, mixing a gemini surfactant with a conventional surfactant produced lower CMCs and lower surface tensions than either of the unmixed surfactants.

The two head groups of a gemini surfactant can be ionic, zwitterionic or nonionic as with conventional surfactants. Gemini surfactants have been synthesised with head groups such as sulphate,[14] carboxylate,[15,16] phosphate,[2,17,18] dimethylammonium,[19-22] and polyoxyethylene[23-28] to name a few. Some gemini surfactants have even been synthesised with two different head groups, for example, one head group is sodium sulphonate and the other a polyoxyethylene.[29]

The chemical linker that joins the two halves of the gemini surfactant can be synthesised with a variety of structures. It can be hydrophilic or hydrophobic, rigid or flexible, long or short. The effect of the linker on the properties of gemini surfactants has been studied extensively, particularly the CMCs of gemini alkyldimethylammonium bromide surfactants (see Figure 2.1), where *n* is the number of carbon atoms per tail and *X* is the chemical linker.

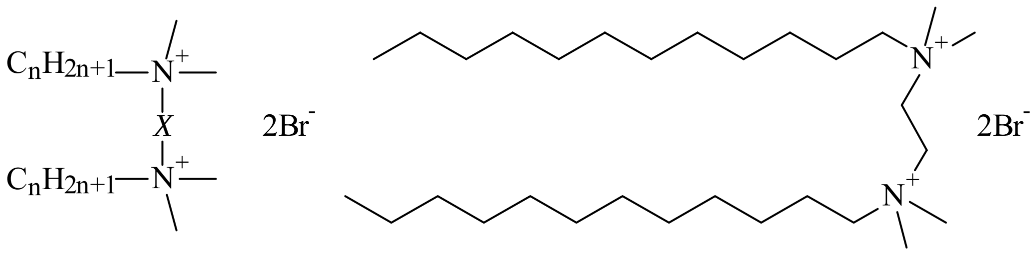

Figure 2.1: Alkyldimethylammonium bromide gemini surfactants (general formula) and an example (12-2-12). *X* is the linker group and *n* is the number of carbons in the linear hydrocarbon tail.

Devínsky *et al.*[19] studied the effect of changing the *hydrophobicity of a short linker*, where (in order of increasing hydrophobicity) X = O, NCH_3, CH_2 and S. They found very little difference in the CMCs and thus, hydrophobicity has little effect on the CMC if the linker is short.

The effect *of rigid linkers* have been studied by Song and Rosen,[30] (for $X = -CH_2C_6H_4CH_2-$) and Menger *et al.*[22] (for $X = -CH_2C{\equiv}CCH_2-$). These studies found that gemini surfactants with rigid linkers have slightly higher CMCs, sometimes by a factor of two. However, this difference is small when the CMC of the gemini surfactant is compared to the CMC of the conventional analogue. It can thus be concluded that, although the rigidity of the spacer makes a small increase in the CMC, its overall affect on the CMC is insignificant.

Zana *et al.*[20] studied the effect of *length of a hydrophobic linker* on CMCs, where $X = -(\mathrm{CH2})_x-$ and $x = 2$ to 16. As the length of the linker increased so did the CMC to a maximum at about $x = 5 \pm 1$. As the spacer length was increased further, the CMC decreased and for lengths greater than $x = 12$ the CMC drops rapidly. However, the variation in the CMC was small up to $x = 10$. For example, when $n = 12$ the maximum CMC was 1.2 mM for $x = 4$ and dropped to only 0.6 mM for $x = 10$. That is, the CMC dropped by only a factor of two when the spacer was more than doubled in size. While this may seem a large change it is small when compared to the conventional surfactant with the same tail length ($C_{12}H_{25}N(CH_3)_3Br$), which has a CMC of 14.5 mM.[5] That is, the CMC of the conventional surfactant is more than ten times the gemini surfactant CMC. Thus, the CMC changes little with the length of the linker when it is reasonably short (less than about 10 CH_2 units).

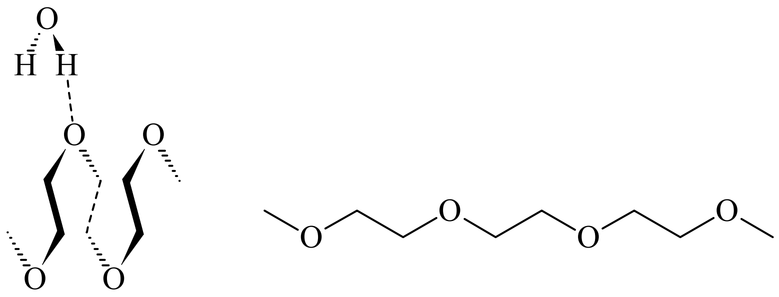

Figure 2.2: Schematic representation of water bonding to one of the lone electron pairs on the ether oxygen atom. On small length scales the polyoxyethylene chain is most probably in a meander conformation[32] (left) as opposed to the zigzag conformation (right). The meander conformation should be more soluble in water because the distance between the ether oxygen atoms is closer to the distance between the water oxygen atoms.

2.1.1 Conventional Nonionic Surfactants

Nonionic surfactants are excellent emulsifiers and are almost totally insensitive to the presence of most electrolytes.[7] For these reason they are used in many industrial applications, especially when exact control of electrolyte concentration is difficult. They can be synthesised with a variety of head groups, such as sugar esters, alkanol amides and amine oxides.[7] However, the most commonly studied nonionic surfactants are the alkylphenol(ethylene oxide) ethers and the alkylpolyethylene glycol ethers. The alkylphenol(ethylene oxide) ethers consist of either a linear or branched alkyl chain attached to a phenol ring and a polyoxyethylene head group. The alkylpolyethylene glycol ethers consist of a linear alcohol tail and a polyoxyethylene head group. Their general formula, $C_nH_{2n+1}O(CH_2CH_2O)_mH$, is abbreviated to C_nE_m for simplicity. Vast studies of their physical chemical properties have been published by many researchers.[31]

The solution properties of nonionic surfactants depend on the length of the hydrocarbon tail (*n*) and the number of ethylene oxides per head group, also called the ethoxylation number (*m*). Much of their physical chemistry depends on the behaviour of the polyoxyethylene head group in solution. Polyoxyethylene is soluble in water because water forms hydrogen bonds to its ether oxygen atoms (Figure 2.2).[32] The chain itself is not straight but behaves like a coil to maximise the interaction with water.

2.1.2 Nonionic Gemini Surfactants

Many nonionic gemini surfactants have been reported in the literature over the last 20 years. A large number of these have been synthesised with sugar based head groups, such as glucamine,[33-35] glucoside[36,37] and many others[38,39] (see Figure 2.3 for examples). There have also been many patents dating back to at least 1986[40] with many possible applications[41-44] such as cleaning agents,[45] personal care products,[46] and photographic emulsions.[47] Most of these studies have focused on synthesis and usually CMC or surface tension studies. Some micelle shape determination has also been conducted using Electron Microscopy[39] and phase studies have been conducted by Eastoe *et al.*[33,34] using a combination of optical microscopy and Nuclear Magnetic Resonance.

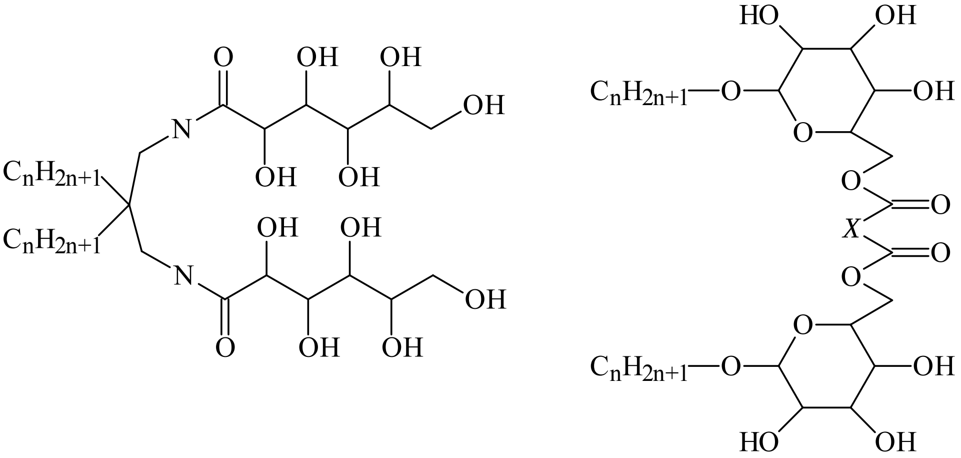

Figure 2.3: Examples of sugar based nonionic gemini surfactants.

Polyoxyethylene gemini surfactants have been studied to a lesser degree than sugar based nonionic gemini surfactants. Tracy *et al.*[25,27,48-51] of Rhodia Inc. have published several patents for the synthesis of many polyoxyethylene gemini surfactants. Noteworthy are a nonyl phenol gemini surfactant (Figure 2.4a)[27] and a linear alkane gemini surfactant with various linkers (Figure 2.4b).[50] They have reported low CMCs and excellent emulsification capabilities, however, the physical chemical properties have not been studied beyond this. Paddon-Jones *et al.*[52] have synthesised a polyoxyethylene nonionic gemini with a dodecylamide tail and a $-CH_2CH_2-$ linker as well as the corresponding monomer (Figure 2.5a and b). They studied the surface tension, CMC and micelle sizes in aqueous solution. Their results provide the first

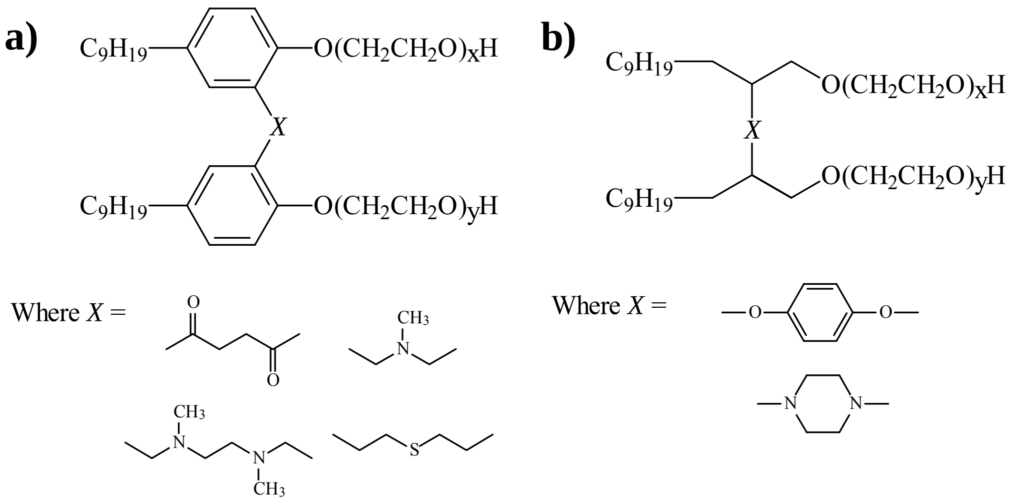

Figure 2.4: Polyoxyethylene surfactants in the literature. a) A nonyl phenol gemini surfactant and b) a linear alkyl gemini surfactant with various linkers.[27,50]

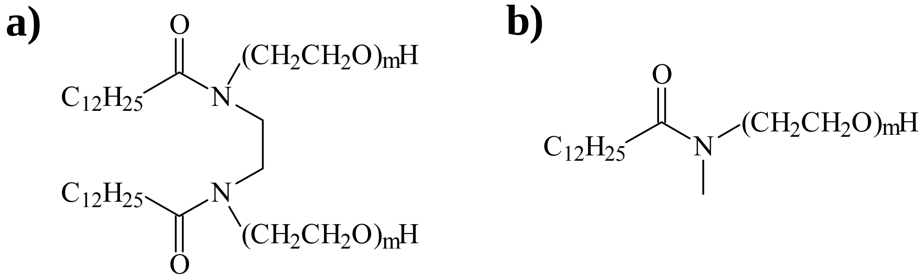

Figure 2.5: a) Nonionic gemini surfactant synthesised and studied by Paddon-Jones *et al.* and b) the corresponding monomer used for comparison.

real comparison between conventional and gemini nonionic surfactants. They found the gemini surfactant had a lower CMC, larger micelles and was more effective at lowering the surface tension.

2.1.3 Surfactants for This Project

The general structure of the nonionic gemini surfactants for this thesis are given in Figure 2.6. There are 20 carbon atoms in each tail (counted from the terminal methyl group to the carbon atom before the first oxygen in the head group). The spacer is six methylene groups and the average ethoxylation number (m) of the head groups is 10, 15, 20 and 30. The nomenclature, for example for m = 15, is 2,9-dioctadecyl-1,10-decanediyl bis(pentadecaethoxylate). This is abbreviated to $Gem_{20}E_m$.

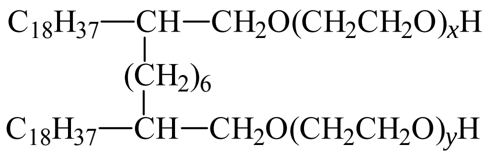

$$\begin{array}{l} C_{18}H_{37}\text{—}\underset{|}{C}H\text{—}CH_2O(CH_2CH_2O)_xH \\ \qquad\quad\;(CH_2)_6 \\ C_{18}H_{37}\text{—}\overset{|}{C}H\text{—}CH_2O(CH_2CH_2O)_yH \end{array}$$

Figure 2.6: The general structure of the surfactants used in this thesis. The ethoxylation number (*m*) is the average of ½(*x* + *y*).

The marked difference between these surfactants and previous nonionic gemini surfactants is that the hydrophobic portion is purely hydrocarbon and contains no heteroatoms such as oxygen or nitrogen. This allows direct comparison to conventional alkyl polyoxyethylene surfactants.

The gemini surfactants were synthesised by Dr Algi Serelis[*] and the synthesis is given in Appendix A1. Two points about the synthesis deserve mention. Firstly, the polyoxyethylene head groups were produced by base catalysed ethylene oxide condensation directly onto the hydrophobic part of the surfactant in the form of a diol.[53] This produces a distribution in the ethoxylation number, as for commercial nonionic surfactants.[53] The average number of ethylene oxide units per head group is calculated from the mole fraction of ethylene glycol added to the reaction. Dr Serelis measured the distribution using mass spectroscopy with matrix assisted laser desorption ionisation (MALDI) and found the experimental average to be very close to the mole fraction added for synthesis. The second point is that the linker is attached to the second carbon from the head group instead of the first. This was necessary because the ethoxylation process requires a primary alcohol for efficiency.

2.2 Micelle Geometries and the Surfactant Packing Parameter

The shape of micelles has a profound affect on the bulk properties of the solution, such as its flow properties and phase stability. Also, different applications require different micelle shapes, for example biochemists require planar aggregates to simulate biological membranes.[54] Many shapes have been proposed for surfactant micelles, such as spheres, rods, ellipsoids, disks and vesicles. In general, though,

---

[*] Dr Serelis was working for Dulux when he performed the synthesis.

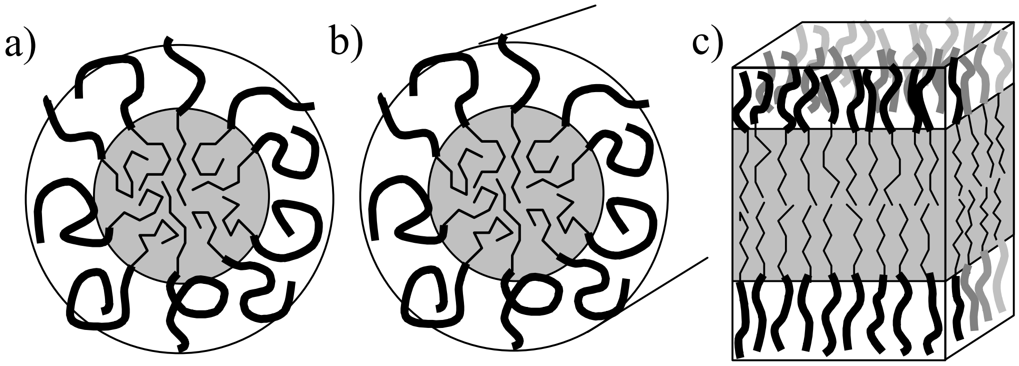

Figure 2.7: Cross-sectional views of the three basic aggregate geometries; a) spherical micelles b) rod-like or cylindrical micelles and c) bilayers.

surfactants aggregate into one of three basic shapes: spheres, rods or bilayers (Figure 2.7).[54] Other micelle shapes can be thought of as distortions or modifications of these three shapes.

The shape of a micelle is highly dependent on the type of surfactant and the conditions in solution, such as electrolyte concentration and temperature. This shape can be rationalised using only three parameters and some simple geometric constraints.[54] The parameters are the length of the hydrocarbon tail, the volume of the hydrocarbon tail and the optimal area per head group. Each of these is discussed below.

Firstly, the length of a surfactant tail determines the radius of a micelle. The radius of a micelle must be less than the fully extended tail of the surfactant. This is because only one fully extended hydrocarbon tail can extend to the centre of a micelle. In fact, spherical micelles will have a radius close to, but slightly less than, the fully extended tail. Thus, as the surfactant tail is increased so is the radius of the micelle, as for example when going from a surfactant with a dodecyl tail ($C_{12}H_{25}$) at ~16.7 Å to a tetradecyl tail ($C_{14}H_{29}$) at ~19.2 Å. This maximum radius is called the critical tail length (l_c). Tanford[55] has calculated l_c for an all trans alkyl tail:

$$l_c = 1.5 + 1.265 n_c \qquad 2.1$$

where n_c is the number of carbon atoms. l_c is practically invariant for any surfactant, regardless of solution conditions such as temperature and electrolyte concentration.

The restriction of the radius being ≤ l_c for spherical micelles is also imposed on rod-like micelles and planar aggregates for at least one dimension. For rod-like micelles the cross-sectional radius is ≤ l_c and for bilayers the thickness is ≤ $2l_c$.

Secondly, the volume of a micelle core is very similar to liquid alkane. The volume of a surfactant tail (v) can thus be calculated from the densities of liquid alkanes. Tanford[55] has calculated v for a linear hydrocarbon tail:

$$v = 27.5 + 26.9n_c \qquad 2.2$$

The value of v, like l_c, is constant for all solution conditions; this is due to the incompressibility of liquid alkanes.

Finally, the optimal area per head group (a_o) is the area that a surfactant occupies at the surface of a micelle. a_o is highly dependent on the type of head group and solution conditions. The value of a_o is the only one of the three parameters that is not constant.

Returning to the question of micelle shapes these three parameters can be combined to give a dimensionless ratio:[54]

$$\frac{v}{a_o l_c} \qquad 2.3$$

called the surfactant packing parameter. The relationship between the packing parameter and micelle shape can be understood by considering some simple geometry. Firstly, the total volume of a micelle is $V=Nv$ and the total area is $A=Na_o$, where N is the number of surfactants per micelle. Combining these two equations gives:

$$\frac{v}{V} = \frac{a_o}{A} \qquad 2.4$$

For a spherical micelle $V = \frac{4}{3}\pi R^3$ and $A = 4\pi R^2$, where R is the radius of the micelle (which is ≤ a critical length, l_c). Substituting these into Equation 2.4 and rearranging gives:

$$\frac{\frac{4}{3}\pi R^3}{v} = \frac{4\pi R^2}{a_o}$$

$$\frac{v}{a_o R} = \frac{1}{3}$$

applying the condition $R \le l_c$ gives the condition for spheres:

$$\frac{v}{a_o l_c} \le \frac{1}{3} \qquad 2.5$$

Thus, if the packing parameter is less than or equal to one third then spherical micelles will form.

For rod-like micelles (ignoring the ends) $V = \pi R^2 L$ and $A = 2\pi RL$, where R is the cross-sectional radius (also $\le l_c$) and L is the length. Substituting these into Equation 2.4 and rearranging gives:

$$\frac{\pi R^2 L}{v} = \frac{2\pi RL}{a_o}$$

$$\frac{v}{a_o R} = \frac{1}{2}$$

applying the condition $R \le l_c$ and considering the result for spheres gives the condition for rods:

$$\frac{1}{3} < \frac{v}{a_o l_c} \le \frac{1}{2} \qquad 2.6$$

Thus, if the packing parameter is greater than one third and less than or equal to one half then rod-like micelles will form. Finally for bilayers (again ignoring the edges) the volume is $V = \frac{1}{2}At$, where t is the thickness of the bilayer ($t \le 2l_c$). Substituting into Equation 2.4 and rearranging gives:

$$\frac{v}{\frac{1}{2}At} = \frac{a_o}{A} \qquad 2.7$$

applying the condition $t \le 2l_c$ and considering the result for rods gives the condition for bilayers:

$$\frac{1}{2} < \frac{v}{a_o l_c} \le 1$$

Thus, if the packing parameter is greater than one half and less than or equal to one, bilayers will form.

2.2.1 Micelle Shape Transitions

Applying the packing parameter to micelle shape transitions changes in micelle shape are determined solely by a_o, since l_c and v are constant. When a_o is reduced the packing parameter increases from *one third* (spherical micelles) to *one half* (rod-like micelles) to eventually *one* (bilayers). This transition from spherical micelles to bilayers can also be rationalised by considering the aggregate curvature. As a_o decreases, the curvature at the surface of the aggregate is decreases, forcing a transition from spheres to rods to bilayers.

2.2.2 Self-Assembly of Nonionic Surfactants

To understand what conditions give rise to changes in micelle shape it is only necessary to understand what conditions change a_o. Since the focus of this work is polyoxyethylene nonionic surfactants, it is necessary to consider what controls a_o in these systems.

For nonionic surfactants a_o is determined by steric repulsions between head groups. As the steric repulsion increases so does a_o. There is no formal theory relating the structure of a polyoxyethylene head group to a_o, however, experimental measurements on conventional nonionic surfactants show that the area per head group increases with ethoxylation number (m) as shown in Figure 2.8a. This relationship is easily rationalised by considering that a larger value of m corresponds to a physically larger head group.

For nonionic surfactants a_o is insensitive to many solution conditions that drastically change its value for cationic surfactants, such as electrolyte concentration and counterion binding. However, it does decrease with increased temperature as seen in Figure 2.8b. The temperature dependence is complex but often explained in terms of a polymer solubility model. As the temperature increases the head group dehydrates and shrinks.[58]

2.3 Thermodynamics of Micelle Formation

The thermodynamics of micelle formation is predominantly concerned with the concentration at which micelles form (i.e. the CMC). Thermodynamics also allows the derivation of several thermodynamic relationships necessary for the interpretation

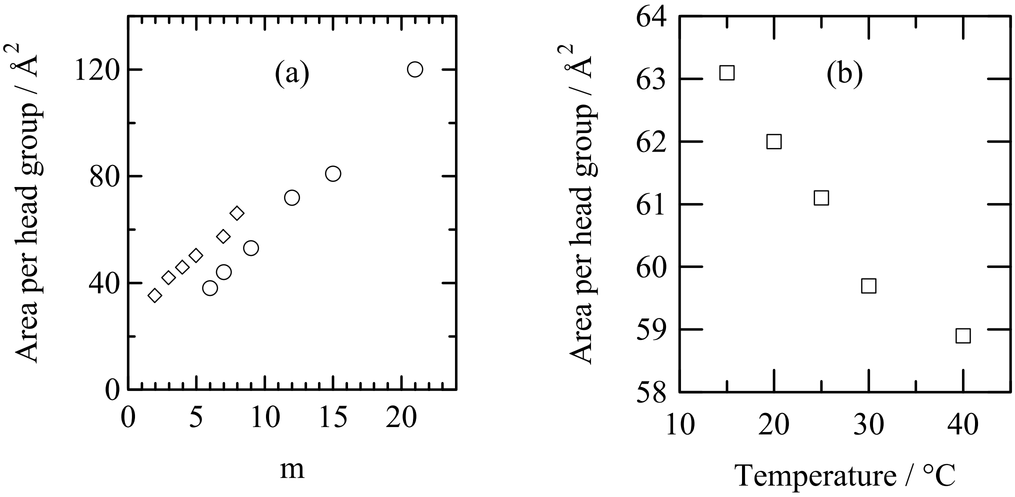

Figure 2.8: a) Area per head group (Å^2) vs *m* for two conventional nonionic surfactants at 25 °C. The diamonds[56] are $C_{12}E_m$ and the circles[31,57] are $C_{16}E_m$. b) Area per head group (Å^2) vs temperature for $C_{12}E_8$.[31,57] The areas are measured at the air/solution interface rather than the micelle/solution interface but still provide useful insight into the behaviour of a_0 under various conditions.

of experimental data. Of interested are: (i) why gemini surfactants have lower CMCs than conventional, analogues surfactants and (ii) how is the CMC affected when two surfactants are mixed.

The derivations require the standard free energy of micelle formation ($\Delta G^{\mathrm{o}}_{\mathrm{mic}}$), which is the energy required to take one mole of surfactant from solution and place it into micelles. At equilibrium $\Delta G^{\mathrm{o}}_{\mathrm{mic}}$ is:[59]

$$\Delta G^{\mathrm{o}} = \mu^{\mathrm{o}}_{\mathrm{B}} - \mu^{\mathrm{o}}_{\mathrm{A}} \qquad 2.8$$

where $\mu^{\mathrm{o}}_{\mathrm{A}}$ and $\mu^{\mathrm{o}}_{\mathrm{B}}$ are the standard state chemical potentials for a surfactant in state A and B respectively. For multi component systems it is more convenient to use:[59]

$$\Delta G^{\mathrm{o}} = -RT \ln K \qquad 2.9$$

where K is the equilibrium constant.

$\Delta G^{\mathrm{o}}_{\mathrm{mic}}$ can be derived by one of two methods; these are the micelle equilibrium model[60-64] and the pseudo phase model.[65-67] Both models have assumptions and restrictions that need to be clearly understood if further theories are to be developed from them. Both theories are presented below.

2.3.1 The Micelle Equilibrium Model

The micelle equilibrium model assumes that surfactants aggregate into micelles with a single, well-defined aggregation number in a reversible equilibrium process:[60-63]

$$NS^{+} + MC^{-} \rightleftharpoons \text{micelle}^{(N\text{-}M)+} \qquad 2.10$$

where S^{+} is a surfactant molecule, C^{-} is a counterion, N is the number of surfactants per micelle and M is the number of counterions that bind to the micelle surface. M is always less than N and is zero for nonionic surfactants (since they have no counterions).

The equilibrium constant for this process is:

$$K_{\text{mic}} = \frac{[\text{micelle}]}{[S^{+}]^{N}[C^{-}]^{M}} \qquad 2.11$$

where the square brackets represent concentration. From this equation the relationship between monomer concentration and surfactant in micelles can be plotted. Figure 2.9 shows the concentration of surfactant in solution versus the total surfactant concentration and the concentration of surfactant in micelles versus total surfactant concentration (for a typically observed large $N \approx 100$).[67] The monomer concentration (solid line) increases almost linearly until the CMC, after which it becomes almost constant. The micelle concentration (dashed line) is almost zero until the CMC after which all additional surfactant goes into micelles.

Substitution of K_{mic} into Equation 2.9 gives:

$$\begin{aligned}\Delta G^{\circ}_{\text{mic}} &= -\frac{RT}{N}\ln\left(\frac{[\text{micelle}]}{[S^{+}]^{N}[C^{-}]^{M}}\right) \\ &= -\frac{RT}{N}\left(\ln[\text{micelle}] - N\ln[S^{+}] - M\ln[C^{-}]\right)\end{aligned} \qquad 2.12$$

where the factor $1/N$ is so the reference state is 1 M of *surfactant molecules*. Figure 2.9 shows that at the CMC, [micelle] ≈ 0 and $[S^{+}] \approx [C^{-}] \approx CMC$. Substituting these values into Equation 2.12 gives:[63]

$$\Delta G^{\circ}_{\text{mic}} = RT(1+\beta)\ln CMC \qquad 2.13$$

where $\beta = M/N$ is the fraction of charge bound to the surface of the micelle. For

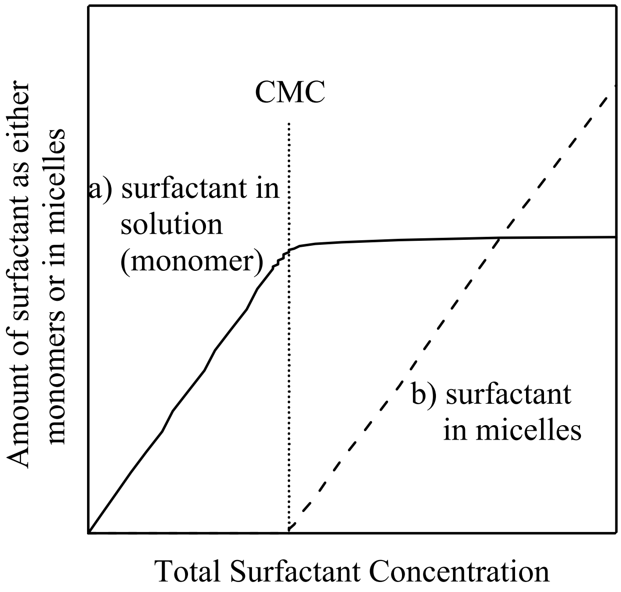

Figure 2.9: Concentration of a) free surfactant vs total surfactant concentration and b) surfactant in micelles vs total surfactant concentration, plotted according to Equation 2.11. Note the sharp change at the CMC after which the concentration of surfactant in solution becomes almost constant and almost all additional surfactant forms micelles.

nonionic surfactants $\beta = 0$ giving:[64]

$$\Delta G^{\mathrm{o}}_{\mathrm{mic}} = RT \ln CMC \qquad 2.14$$

Of significance here is that $\Delta G^{\mathrm{o}}_{\mathrm{mic}}$ is proportional to ln*CMC* and not *CMC*. Thus, the CMC decreases exponentially with an increase in the absolute value of $\Delta G^{\mathrm{o}}_{\mathrm{mic}}$.

The equilibrium model can be used for both ionic and nonionic surfactants. It requires only the CMC and the fractional charge for ionic surfactants, which are both easily accessible from experiment. The disadvantage of the equilibrium model is that it becomes too complicated when trying to deal with mixed surfactants.

2.3.2 The Pseudo Phase Model

The pseudo phase model assumes that micelles can be treated as a separate phase from the micelle solution.[65-67] At equilibrium the chemical potential of a surfactant in a micelle is equal to the chemical potential of a surfactant in solution:[67]

$$\mu_{\mathrm{mic}} = \mu_{\mathrm{mon}} \qquad 2.15$$

From ideal solution thermodynamics (assuming no interactions) the chemical potentials can be written (see Appendix A2):[6]

$$\mu_{\mathrm{mic}} = \mu^{\mathrm{o}}_{\mathrm{mic}}$$

$$\mu_{\mathrm{mon}} = \mu^{\mathrm{o}}_{\mathrm{mon}} + RT \ln x_{\mathrm{mon}}$$

Substituting into Equation 2.15 gives:

$$\mu^{\mathrm{o}}_{\mathrm{mic}} = \mu^{\mathrm{o}}_{\mathrm{mon}} + RT \ln CMC$$

$$\mu^{\mathrm{o}}_{\mathrm{mic}} - \mu^{\mathrm{o}}_{\mathrm{mon}} = RT \ln CMC \qquad 2.16$$

where the left hand side of this equation is $\Delta G^{\mathrm{o}}_{\mathrm{mic}}$ (Equation 2.8) giving the same result as the equilibrium model for nonionic surfactants (c.f. Equation 2.14):

$$\Delta G^{\mathrm{o}}_{\mathrm{mic}} = RT \ln CMC$$

The pseudo phase model is much simpler than the micelle equilibrium model but still provides the same expression for nonionic surfactants. Due to its simplicity it will allow the treatment of mixed surfactant systems, which is not possible with the micelle equilibrium model. The limitation of this model is that it is only valid for nonionic surfactants.

2.3.3 Thermodynamics of Gemini Surfactants (Simple Theory)

A simple thermodynamic treatment of micelle formation can be used to produce a relationship between a gemini surfactant CMC and the corresponding conventional surfactant CMC. Assuming the gemini surfactant is two conventional surfactants chemically linked (and the chemical linker does not affect the CMC) significantly then the free energy of placing *one* gemini surfactant in a micelle is the same as placing *two* conventional surfactants in a micelle. Thus, the standard free energy of micelle formation for a gemini surfactant is twice that for a conventional surfactant:

$$\Delta G^{\mathrm{o}}_{\mathrm{gem}} = 2\Delta G^{\mathrm{o}}_{\mathrm{conv}}$$

Substituting in Equation 2.14 for the standard free energies of nonionic surfactants gives:

$$RT\ln\left(\frac{CMC_{\mathrm{gem}}}{2}\right) = 2RT\ln\left(CMC_{\mathrm{conv}}\right)$$

where CMC_{conv} and CMC_{gem} are respectively the CMCs of the conventional and the gemini surfactant in *moles of tail per litre*. These units produce the factor of one half for CMC_{gem} as explained below. Cancelling terms in the above equation gives:

$$CMC_{\mathrm{gem}} = 2CMC_{\mathrm{conv}}^{2} \qquad 2.17$$

The units of *moles of tail per litre* make no difference to the single tailed conventional surfactants but effectively double the concentration of gemini surfactants. This is required for comparison reasons, since a gemini surfactant is equivalent to two conventional surfactants.[8] Without these units the affect of the gemini surfactant would be overstated by a factor of two.

The CMC drop predicted for the gemini surfactants is quite large. For example, if a conventional nonionic surfactant has a CMC of ~10^{-3} M the gemini surfactant would have a CMC of ~ 2×10^{-6} M. This simple theory predicts an enormous advantage when going from a conventional to a gemini surfactant. It will be seen in Chapter 4 that this prediction is ambitious when compared to experimental data. However, it provides a useful theoretical limit and is used for comparison to ideal behaviour.

2.3.4 Thermodynamics of Mixing (Ideal Solutions)

When two surfactants with different CMCs are mixed the system usually acquires a single new CMC. Depending on the interactions between the two surfactants this mixed CMC (designated $\mathrm{CMC}_{\mathrm{mixed}}$) is usually either between the CMCs of the two raw surfactants or at some value less than this. The simplest theory to treat mixed CMCs is the ideal mixing equation,[68] which will be presented below.

Assuming ideal mixing, the chemical potentials for a surfactant molecule *i* in a micelle and a surfactant in solution can be written as (see Appendix A2):

$$\mu_{mic,i} = \mu^{\mathrm{o}}_{mic,i} + RT\ln m_i$$
$$\mu_{mon,i} = \mu^{\mathrm{o}}_{mon,i} + RT\ln x_i$$

where m_i is the mole fraction of surfactant *i* in a mixed micelle and x_i is the mole fraction of surfactant *i* in solution. At equilibrium the chemical potentials are equal:

$$\mu_{mic,i} = \mu_{mon,i}$$

and substitution of the chemical potentials gives:

$$\mu^{\text{o}}_{mic,i} + RT\ln m_i = \mu^{\text{o}}_{mon,i} + RT\ln x_i$$

$$\mu^{\text{o}}_{mic,i} - \mu^{\text{o}}_{mon,i} = RT\ln\left(\frac{x_i}{m_i}\right)$$

where the left hand side of this expression is the same as in Equation 2.16. Equating these two expressions and rearranging gives:

$$RT\ln CMC_i = RT\ln\left(\frac{x_i}{m_i}\right)$$

$$x_i = m_i CMC_i$$

where CMC_i is the CMC of pure surfactant *i*. Now at the mixed CMC (CMC_{mixed}) almost all surfactant is still in solution and the mole fraction of surfactant *i* may be written:

$$x_i = \alpha_i CMC_{\text{mixed}}$$

where α_i is the fraction of surfactant *i* with respect to the other surfactant. Equating these last two expressions, rearranging and then summing both sides gives:

$$\frac{1}{CMC_{\text{mixed}}}\sum m_i = \sum\frac{\alpha_i}{CMC_i}$$

CMC_{mixed} is a constant and can be removed from the summation. $\Sigma m_i = 1$, since this is just the sum of all surfactant in a mixed micelle (in fractional units). For a two surfactant system the ideal mixing equation reduces to:[68]

$$\frac{1}{CMC_{\text{mixed}}} = \frac{\alpha_1}{CMC_1} + \frac{1-\alpha_1}{CMC_2} \qquad 2.18$$

where CMC_1 and CMC_2 are the CMCs of the pure surfactants and α_1 is the mole fraction of surfactant 1. There are no synergistic effects with ideal mixing, since these require favourable interactions between the mixed surfactants.

2.4 Phase Behaviour

The study of phase behaviour seeks to answer three basic problems about a system.[69] How many phases does a system form? What is the composition of these phases with temperature, pressure and composition? And what is the structure of these phases?

The phase behaviour of a system depends only on the temperature, pressure, volume and composition of the components. In this work, only the binary phase behaviour of surfactant and water is of interest. In this case the phase behaviour can be represented on a "phase diagram" with only two axes. By convention the ordinate is surfactant composition in weight percent (wt%) and the abscissa is temperature (°C). The pressure does not affect the phase diagram much and is assumed to be roughly constant at one atmosphere[69] while the volume is uniquely determined by all the other variables and does not need to be considered.

2.4.1 The Cloud Temperature and Solubility

Figure 2.10 shows the idealised phase behaviour of a micelle-forming surfactant in the solubility region.[69] The solid line is the solubility curve, below which a surfactant is insoluble. A sample in this region consists of solid surfactant coexisting with dilute surfactant solution. For real systems there are also usually mesophases present and the solid surfactant may even be coexisting with one of these.

The dashed line in Figure 2.10 shows the temperature dependence of the CMC with concentration. For nonionic surfactants the CMC decreases as the temperature is increased.[70]

As the temperature of a nonionic surfactant is increased, the polyoxyethylene head group becomes less soluble. Eventually the surfactant becomes insoluble and separates into two solutions:[71] a surfactant lean solution (W) and a surfactant rich solution (L_1). With time these two phases will separate, although in practice the densities are usually very similar and separation is very slow. As a result the sample goes "cloudy" as the two phases nucleate as droplets and begin to separate. Therefore, the temperature at which the surfactant begins to separate is called the cloud temperature. This behaviour, which is almost unique to nonionic surfactants, is shown for the conventional surfactant $C_{12}E_6$ in Figure 2.11.[72] The cloud temperature is the lowest temperature of the two phase region. As the temperature is increased the two phases separate further, as will be discussed later. The cloud temperature increases with larger ethoxylation numbers and decreases with larger alkyl tails.[71]

Error! Objects cannot be created from editing field codes.

Figure 2.10: The idealised solubility behaviour of surfactants.[69] Tie lines are shown between surfactant solution and solid surfactant. The dashed line is the CMC dependence, showing a decrease with increasing temperature.[70]

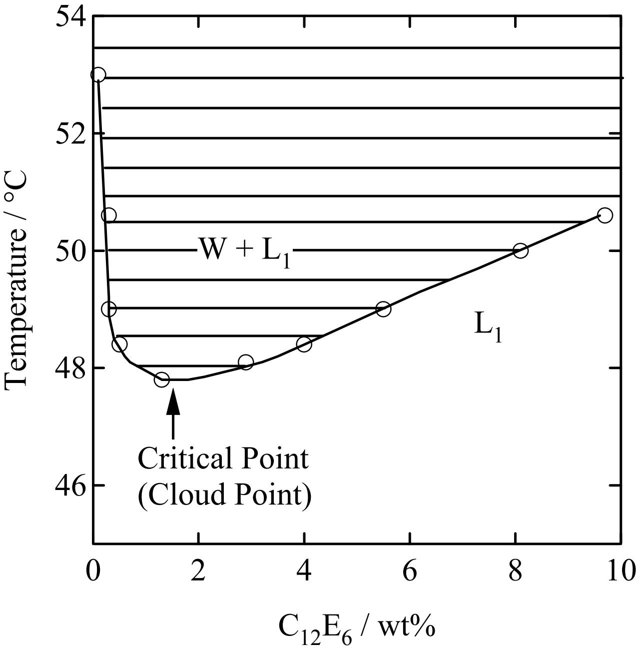

Figure 2.11: Partial phase diagram of $C_{12}E_6$ showing the critical point (cloud point), where phase separation into a dilute surfactant solution (W) and a concentrated micelle solution (L_1) occurs.[72] Tie lines are shown between the two phases W and L_1.

2.4.2 Mesophases

Matter at its most basic level is often thought of as existing in one of three states; these are solid, liquid or gas. However, other phases exist, especially in surfactant-water systems. These phases have structures in between that of crystalline solids and simple liquids and are called mesomorphic phases (from the Greek word 'mesos' meaning 'middle') or just mesophase. They are also called *lyotropic* liquid crystals, meaning a liquid crystal that requires a solvent.

Surfactant mesophases, at a molecular level, are constructed of one of the three basic self-assembly structures presented previously (i.e. spheres, rods or bilayers). These structures are highly ordered at a local level producing an almost crystal like structure in some cases. This structure can extend for great distances but is never as well defined as a true crystal solid.

2.4.3 Surfactant Mesophases

Surfactants form many different mesophase structures but the two most common are the hexagonal phase and the lamellar phase. The hexagonal phase (H_1) consists of long, rod-like micelles arranged in a hexagonal structure (as in Figure 2.12a). The lamellar phase (L_α) consists of surfactant bilayers stacked in ordered layers with a constant distance between them (as in Figure 2.12b).

Two other common phases are the micellar cubic phase (I_1) and the bicontinuous cubic phase (V_1). The micellar cubic phase is a close packed arrangement of spherical, or short rod-like micelles. The micelles are packed in either a body centred or a face centred arrangement (as in Figure 2.13a). The V_1 bicontinuous cubic phase is formed from interconnected branched rods as, for example, in Figure 2.13b.

There are many other mesophases formed by different surfactant systems but these are much less frequently observed than the four phases mentioned above. Further, other phases that form are almost always distortions of the four phases already mentioned, with either a distortion in the arrangement of the micelle packing or with distortions to the actual shape of the micelles. These will be discussed as they arise.

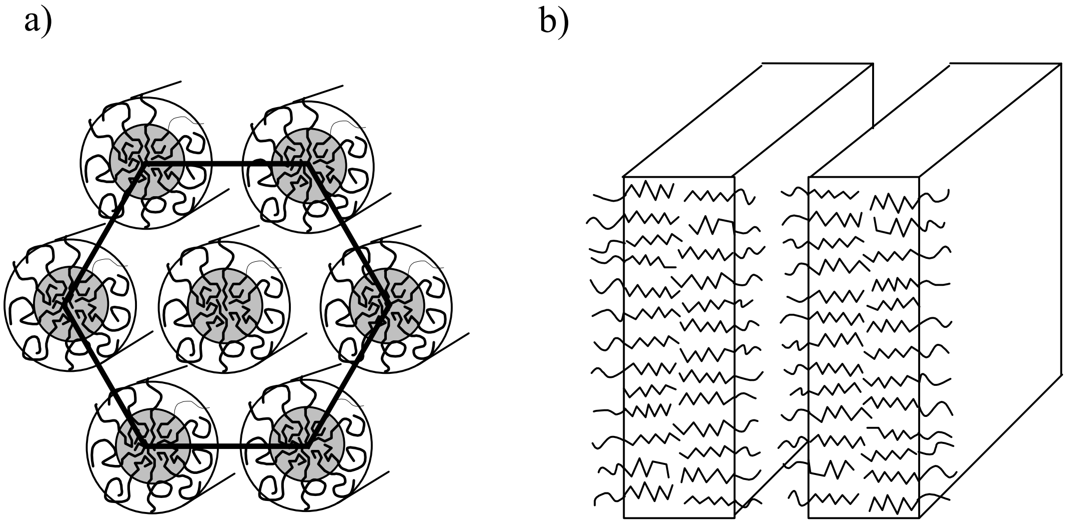

Figure 2.12: The micellar structure of (a) a Hexagonal phase (H_1) and (b) a lamellar phase (L_α).

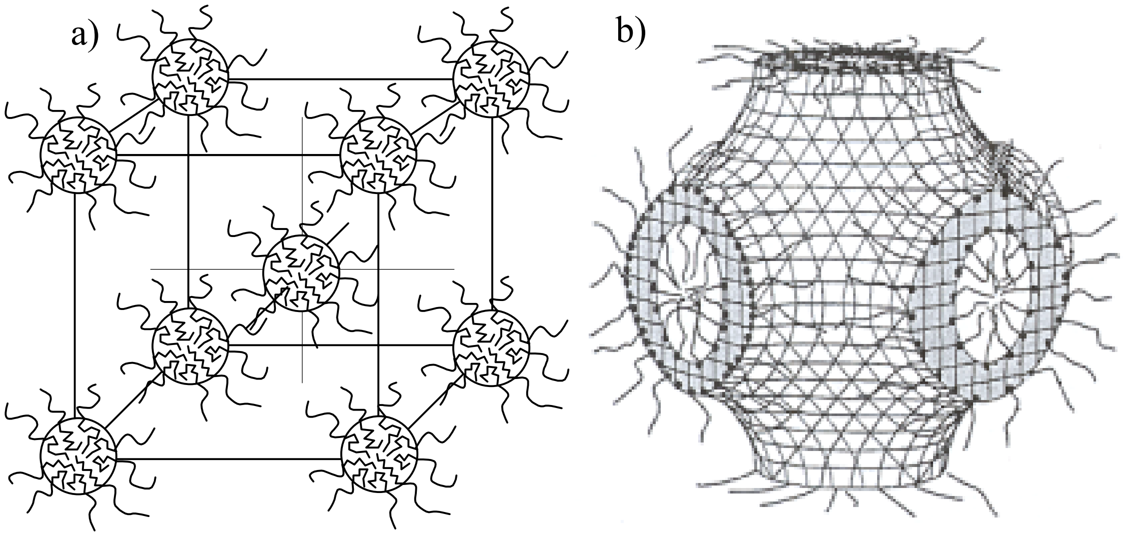

Figure 2.13: (a) The micellar structure of micellar cubic phases (I_1) in either a body centred or face centred arrangement and (b) an example of a bicontinuous cubic phase (V_1) demonstrating the segregation of two water channels by the curved surfactant bilayer.[73]

2.4.4 Phase Behaviour of Conventional Nonionic Surfactants

2.4.4.1 The Order of Mesophases with Concentration

Consider the phase behaviour of $C_{12}E_8$ in Figure 2.14.[71] As the concentration is increased, at 15°C, the phases form in the order: micelle solution (L_1), cubic phase (I_1), hexagonal phase (H_1), bicontinuous cubic phase (V_1) and finally a lamellar phase (L_α). As the concentration is increased, the aggregates making up the mesophases go from spherical, in micelle solution and cubic phase, to rod-like (hexagonal phase) and finally to planar (lamellar phase). That is, the aggregates become less curved. The order that mesophases form with increased concentration can be summarised as:[74]

Cubic → Hexagonal → Bicontinuous Cubic → Lamellar although not all of these phases must form.

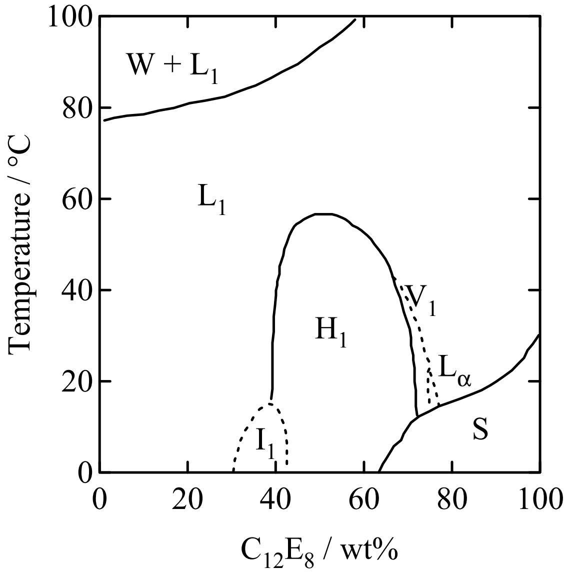

Figure 2.14: The phase diagram of $C_{12}E_8$ showing, with increasing concentration, cubic phase (I_1), Hexagonal phase (H_1), bicontinuous cubic phase (V_1), lamellar phase (L_α) and solid surfactant (S).[71]

The reasons for this behaviour are complex and are discussed in Chapter 6, when discussing the phase behaviour of the gemini surfactants.

2.4.4.2 Transitions Between Phases

A point that is not obvious in Figure 2.14 but deserves mention is the nature of the phase transitions. The thermodynamics of this is dealt with by Laughlin[69] and will only be treated very briefly here. It is first necessary to understand the concept of miscibility gaps. A miscibility gap is a composition range where no *single* phase is stable. A system in this region will separate into two stable phases. Two examples of this have already been presented; they are the solubility region (Figure 2.10), where pure surfactant coexists with surfactant solution, and the clouding region (Figure 2.11), where dilute surfactant coexists with surfactant rich solution.

Phase transitions in surfactant systems are first order phase transitions. This means phase boundaries are discontinuous and that coexistence regions must exist between all phases. In practice this is not always observed (as seen in Figure 2.14) especially for nonionic surfactants where the coexistance region is very narrow and difficult to detect. However, it is important to understand that a phase does not slowly transform from one phase to another but that the transition is abrupt and discontinuous.

The composition of a two-phase coexistence region can be calculated using a simple mass balance called the Lever Rule.[69] For a binary system the region between two phases (say phase A and phase B) can be represented as in Figure 2.15. The lines joining the two phases are called tie lines. Any sample along the tie line will consist of phase A with a composition at point *a* coexisting with phase B with a composition at point *b*. The fraction of the two phases in this region is determined by the position along the tie line. If the sample is at point *c* then the fraction of phase A will be the ratio of cb/ab and the fraction of phase B will be the ratio of ac/ab. Thus at point *a* the sample will be 100% phase A and at point *b* it will be 100% phase B.

2.4.4.3 Dependence of Phase Behaviour on Surfactant Structure

As the head group size of a surfactant is increased it will favour more curved aggregates and thus give rise more readily to cubic phases. Decreasing the head group size will have the opposite effect and give rise more readily to lamellar phases. For example, $C_{12}E_6$, which has a smaller head group than $C_{12}E_8$ in Figure 2.14 does not form a micellar cubic phase. Further, $C_{12}E_{12}$, which has a much larger head group than $C_{12}E_8$ forms a cubic phase and a hexagonal phase but does not form a lamellar phase.[71]

As the tail of a surfactant is increased in size this will favour less curved

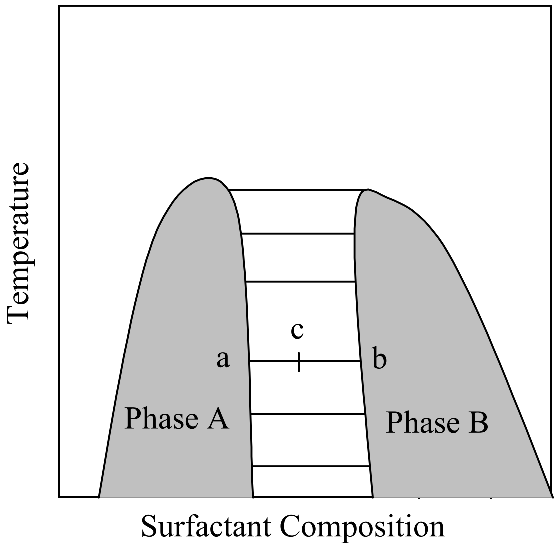

Figure 2.15: Schematic of the coexistence region between two phases (A and B). The composition of each phase at a point c along a tie-line can be calculated from the composition at points a and b using the lever rule (see text).

aggregates and thus give rise more readily to lamellar phases. This is seen when comparing the melting temperature of $C_{12}E_8$ and $C_{16}E_8$.[71] The L_α phase melts at 22 °C for $C_{12}E_8$ but is stable up to 100 °C for the longer tailed $C_{16}E_8$.

Chapter 3: Experimental Methods

3.1 Critical Micelle Concentrations (CMCs)

At the CMC the concentration of free surfactant becomes almost constant and any additional surfactant added to the solution forms micelles. To measure the CMC it is then necessary to measure some property of the solution that behaves differently with the presence of micelles.

CMCs are measured by measuring some bulk solution property as a function of surfactant concentration. At the CMC there is often a sharp change corresponding to the formation of micelles. Some examples are shown in Figure 3.1.

Many solution properties change with the onset of micelle formation and so the CMC can be determined by many different techniques. Some solution properties that have been used are osmotic pressure, conductivity, surface tension, dye solubilization and interfacial tension – although many, many more are reported in the literature.[5] However a few techniques have become standard such as conductivity and surface tension. The exact technique that is chosen depends on many factors such as (i) the type of surfactant being studied, (ii) ease of use and (iii) additional information that the technique may provide.

For ionic surfactant the method most often employed is conductivity because it is fast, easy and fairly insensitive to impurities. Conductivity measurements also allow an estimation of β,[77] which is an important thermodynamic parameter necessary for calculating the free energy of micelle formation of ionic surfactants (see Equation 2.13).

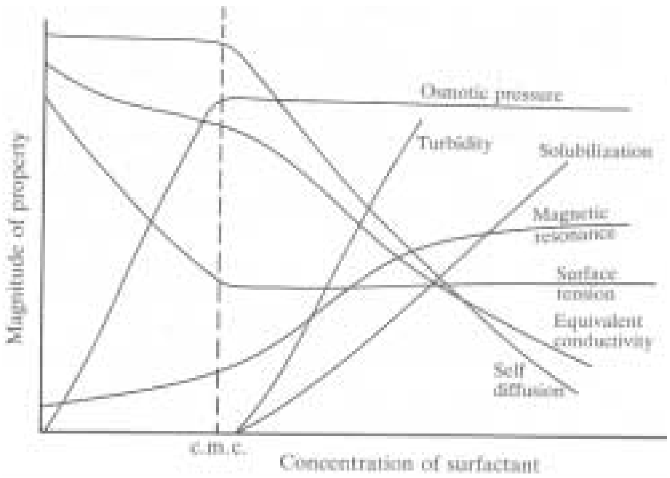

Figure 3.1: A schematic representation of some CMC measurements. Following Lindman and Wennerström,[75] and reproduced from Hunter.[76]

For nonionic surfactants the method most often employed is surface tension. In contrast to conductivity, surface tension is slow, difficult and very sensitive to trace amounts of surface-active impurities. Despite the difficulties it is used because it is highly accurate and may be used to measure the area per head group at the air-solution interface,[78] which is an approximation to a_o.

3.1.1 CMC Measurement using a Fluorescence Probe

For reasons given in Chapter 4, the CMCs were measured in this work using a pyrene fluorescence method.[79] Surfactants with an alkyl tail have micelle cores that behave much like a bulk hydrocarbon. As such, non-polar molecules, which are otherwise insoluble in solution, will be taken into the micelle core. This property of surfactants is called solubilization and is the basis for CMC measurement using a fluorescent probe.

Solubilization only occurs when micelles are present and thus only above the CMC. The fluorescence spectrum of a probe is recorded as a function of surfactant concentration, at the CMC micelles form and the probe is solubilized. A change in the peak intensity or a shift in the peak position occurs.

3.1.1.1 Experimental Equipment

Pyrene was used as the probe in this work. The fluorescence spectra of pyrene in water and pyrene in micelles is shown in Figure 3.2a and Figure 3.2b respectively. The ratio of the first and third peak intensity is used. In Figure 3.2 the ratio is obviously different for each environment and has a value of approximately 1.8 in solution and 1.2 in micelles.

The solubility of pyrene in water is 6x10^{-7} M[80] and approximately 7x10^{-2} M in liquid alkanes.[81] A saturated solution of pyrene was made by placing a crystal in pure water and stirring vigorously for several hours. This solution was diluted by approximately a factor of two and used to make a series of surfactant solutions. The concentration range was logarithmic and covered at least three orders of magnitude.

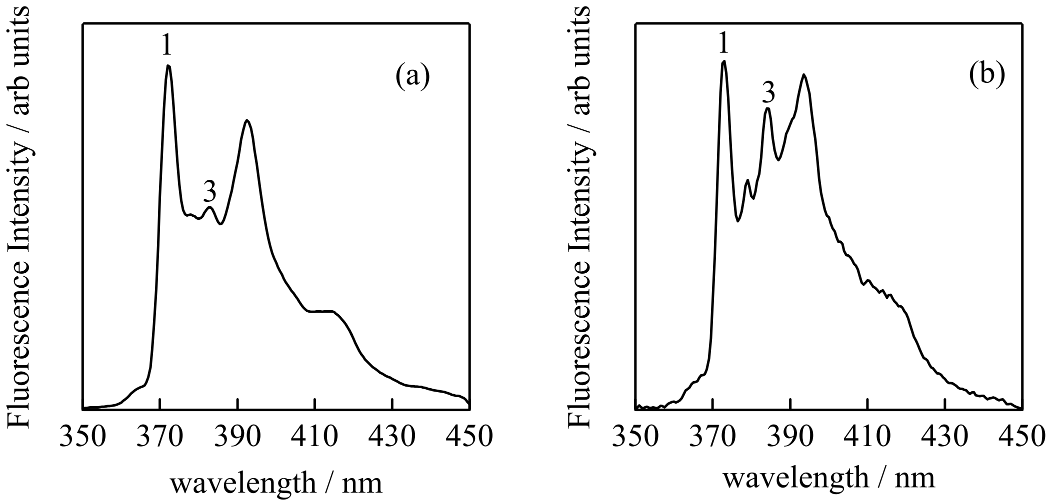

Figure 3.2: Fluorescence spectrum of pyrene a) in aqueous solution and b) in micelles. The ratio of Peak 1 to Peak 3 ($I_{1/3}$) is 1.8 in water and below the CMC. Above the CMC $I_{1/3}$ drops to ~1.2 as shown in b.

The fluorescence spectra were collected using a Perkin Elmer LS 50B fluorimeter. An excitation wavelength of 238 nm was used with a slit width of 15.0 nm. The emission spectra were collected by scanning from 350 nm to 450 nm at 100 nm/minute with a slit width of 2.5 nm. The maximum intensity of the first and third peak was obtained using the peak assignment software supplied by Perkin Elmer. The first peak was always in the range 371 nm to 375 nm and the third peak was always in the range 382 nm to 386 nm, although the value changed slightly as the pyrene moved from solution into micelles. The average intensities of 10 spectra where used for each concentration and the standard deviation was taken as the instrumental error.

3.1.1.2 Problems and Complications

The main disadvantage of the fluorescent probe technique is that it adds an impurity into the system. This raises the possibility of micelles being nucleated at low concentrations and artificially lowering the CMC. However, CMCs measured by surface tension with and without pyrene show no significant difference.[82]

3.2 Small Angle Neutron Scattering (SANS)

In Small Angle Neutron Scattering (SANS) a beam of monochromatic neutrons is passed through a sample and the intensity of scattered neutrons is recorded as a function of angle, as shown in Figure 3.3. The size, shape and interactions of micelles in solution determine the form of the scattering pattern and fitting it to appropriate models recovers this information. In fact, this is the reason for doing SANS in the first place, to determine the size, shape and interaction of micelles in solution.

Error! Objects cannot be created from editing field codes.

Figure 3.3: Schematic of a neutron scattering experiment. Monochromatic neutrons are passed through the sample and the scattered neutrons measured as a function of angle.

The great advantages of SANS is that relatively little sample preparation is required and micelles can be studied in solution. Current SANS instruments elucidate information on length scales of 10 – 1000 Å, which is of the order of micelle sizes.[83]

The scattering produced by SANS is due to the wave-like properties of neutrons. Neutrons interact with atomic nuclei and are either absorbed or scattered. At the energies used in SANS there is usually little absorption and it will be ignored. The scattering of neutrons from two nuclei j and k in a particle is shown schematically in Figure 3.4a. The two waves have to travel different distances to the detector, which creates a path difference between them. This produces either constructive or destructive interference at the detector. The total scattering pattern is obtained by adding all scattering contributions between all scattering nuclei. This addition is between all pairs of nuclei in a micelle *and* for all pairs of nuclei between different micelles. This creates a great deal of mathematical complexity, which will be reduced with a few simplifying assumptions.

Error! Objects cannot be created from editing field codes.

Figure 3.4: a) Neutron scattering from the two points i and j in a particle and b) the scattering vector for scattering angle θ.

Recovering the size, shape and interactions of micelles from SANS data is called the inverse scattering problem. It is not possible, however, to do a direct transform of SANS data to obtain the original micelle parameters. The method most often used to recover information is to fit the experimental data using mathematically derived scattering functions for several different micelle shapes. These functions are typically analytical equations that depend on parameters such as radius for a sphere, or length and diameter for a rod, or diameter and thickness for a disc etc. Therefore, SANS is a data fitting technique and often requires some chemical intuition and insight to ensure that a physically reasonable interpretation is made.

The following is a brief review of (i) what gives rise to the scattering patterns, (ii) how information is extracted from the scattering patterns and (iii) how it is measured experimentally. More detailed information is contained in the references used throughout this chapter and in the books and reviews by Guinier & Fournet,[84] Kostorz,[85] Gatter & Kratky,[86] Hayter,[87] and Lindner & Zemb.[83]

3.2.1 Basic Scattering Theory

For mathematical simplicity it is convenient to describe the motion of neutrons using wave vectors ($\boldsymbol{k}$), which are in the direction of neutron motion and have magnitude $2\pi/\lambda$, where λ is the wavelength of the neutrons. We only require the wave vectors for the incident neutrons, $\boldsymbol{k}_\mathbf{0}$ (which is in the direction of the incident beam) and for the scattered neutrons, $\boldsymbol{k}_\mathrm{S}$ (which is in the direction of scattering). The scattering equations are all formulated as a function of the scattering vector, $\boldsymbol{Q}$, which is the difference between $\boldsymbol{k}_\mathbf{0}$ and $\boldsymbol{k}_\mathrm{S}$ (i.e. $\boldsymbol{Q} = \boldsymbol{k}_\mathbf{0} - \boldsymbol{k}_\mathrm{S}$). For quasi-elastic neutron scattering, which was used for this thesis, the magnitude of $\boldsymbol{k}_\mathbf{0}$ and $\boldsymbol{k}_\mathrm{S}$ are approximately equal and so the magnitude of $\boldsymbol{Q}$ can be calculated using simple geometry, as shown in Figure 3.4b, to give:

$$Q = \frac{4\pi}{\lambda}\sin\left(\frac{\theta}{2}\right) \qquad 3.1$$

where λ is the wavelength of the incident neutrons and θ is the scattering angle. In practice λ is typically kept constant for SANS experiments so Q is simply a function of the scattering angle θ. With this in mind the following treatment of SANS will refer to scattering as a function of Q and not as a function of angle.

Before continuing with the task of scattering from micelles it is necessary to define some notation with regards to scattering from atomic nuclei. Scattering is defined in terms of the total scattering cross section per nucleus, σ, which has units of area:[88]

$$\sigma = \frac{S}{\Phi_o}$$

where S is the number of neutrons absorbed or scattered per second (neutrons.s^{-1}.nucleus^{-1}) and Φ_o is the number of neutrons striking the sample per second per unit area (neutrons.m^{-2}.s^{-1}). The scattering cross section is sometimes thought of as the probability that a nucleus will scatter radiation. It is the total scattering from a nucleus over all values of Q, where larger values of σ correspond to a larger quantity of scattering.

The scattering cross section is composed of absorption, incoherent scattering and coherent scattering:[88]

$$\sigma = \sigma_{\mathrm{abs}} + \sigma_{\mathrm{incoh}} + \sigma_{\mathrm{coh}}$$

Absorption (σ_{abs}) is typically small and will be ignored as stated before. The incoherent scattering (σ_{incoh}) is constant over all values of Q, which adds a constant background to the scattering. Only the coherent scattering (σ_{coh}) is of use and is characterised by the scattering length, b, which has units of length:

$$\sigma_{\mathrm{coh}} = 4\pi b^2$$

The scattering length can be thought of as how well a neutron is scattered from an atomic nucleus. There is no theoretical means to calculate it for a given nucleus and it must be measured experimentally. Table 3.1 has scattering lengths for hydrogen, carbon and oxygen, which are the component elements in the non-ionic surfactants used in this work. Column one also lists the isotopes of hydrogen, and column two their natural abundances. Also listed are the coherent scattering in column four and the incoherent scattering in column five. The absorption cross-sections for neutrons with a wavelength of 1.5 Å are listed in column six. Note the small value of the absorption scattering cross section compared to the coherent scattering cross section, which justifies ignoring it in calculations. Note also the large incoherent scattering for ^{1}H (i.e. 80.27) compared with its coherent scattering (i.e. 1.757). The large relative abundance of ^{1}H in nature (i.e. 99.985 %) means hydrogen rich systems such as water and hydrocarbons will have a very large background signal that can easily swamp the signal being measured. This problem is overcome by using solvents where the hydrogen has been replaced with ^{2}H, which has a much lower incoherent scattering than ^{1}H (i.e. 2.05 compared to 80.27). For this reason deuterium oxide (^2H_2O) was always used as the solvent instead of normal water.

Returning to the problem of scattering from a solution of micelles the coherent scattering function produced by all pairs of nuclei j and k (Figure 3.4a) can be written:[87]

$$\frac{\partial\sigma}{\partial\Omega}(\boldsymbol{Q}) = \left\langle \sum_{\mathrm{jk}} b_{\mathrm{j}} b_{\mathrm{k}} \exp(i\boldsymbol{Q}\cdot\boldsymbol{R}_{\mathrm{jk}}) \right\rangle \qquad 3.2$$

where b_{j} and b_{k} are the scattering lengths for nuclei j and k, $\mathrm{i} = \sqrt{-1}$, $\boldsymbol{R}_{\mathrm{jk}}$ is the position vector for points j and k (i.e. $\boldsymbol{R}_{\mathrm{k}} - \boldsymbol{R}_{\mathrm{j}}$ with reference to some arbitrary origin) and Ω is the solid angle of the detector. Equation 3.2 is called the differential scattering cross section and is the scattering intensity as a function of $\boldsymbol{Q}$. The triangular brackets indicate an average over all orientations in solution and the sum is for all pairs of scattering nuclei in a micelle *and* between micelles. The differential scattering cross section is obtained from experiment and Equation 3.2 is the starting point for deriving SANS functions. In practice, it is never possible to use Equation 3.2 directly and it

Element	**Percentage Abundance**	**b (10^{-15} m)**	**σ_{coh} (barn)**	**σ_{incoh} (barn)**	**σ_{abs} (barn)**
H	—	–3.739	1.757	80.26	0.333
1H	99.985	–3.740	1.758	80.27	0.333
2H	0.015	6.671	5.592	2.05	0.001
C	—	6.646	5.550	0.001	0.004
O	—	5.803	4.232	0.000	0.000

Table 3.1: Scattering values for Hydrogen, Carbon and Oxygen.[87,89]

must be simplified to specific models. This will be done in the next section for several common micelle shapes.

3.2.2 Scattering Models for Common Micelle Shapes

Assuming no interactions between micelles, the scattering between atomic nuclei in different micelles can be ignored and Equation 3.2 becomes:[87]

$$\frac{\partial\sigma}{\partial\Omega}(\boldsymbol{Q}) = N_P\left\langle\left|\sum_{\mathrm{j}} b_{\mathrm{j}}\exp(i\boldsymbol{Q}\cdot\boldsymbol{R}_{\mathrm{j}})\right|^2\right\rangle \qquad 3.3$$

where N_P is the number of micelles and $\boldsymbol{R}_{\mathrm{j}}$ is the position vector of scattering element j. The sum is for all scattering nuclei in a micelle and the average is for all micelle orientations. The mathematics is simplified if the micelle and the solvent are assumed to be a continuous medium rather than made from discrete nuclei. This approximation is valid in typical SANS experiments where the smallest measured length scale is much larger than the distance between atoms. The discrete sum in Equation 3.3 can now be replaced by a continuous integral over the volume of a micelle:[87]

$$\begin{aligned}\frac{\partial\sigma}{\partial\Omega}(\boldsymbol{Q}) &= N_P\left\langle\left|\int_{V_{\mathrm{P}}}\left(\rho(\boldsymbol{r})-\rho_{\mathrm{solv}}\right)\exp(i\boldsymbol{Q}\cdot\boldsymbol{r})d\boldsymbol{r}\right|^2\right\rangle \\ &= N_P\left\langle F^2(\boldsymbol{Q})\right\rangle\end{aligned} \qquad 3.4$$

where $\rho(\boldsymbol{r}) = \sum b_{\mathrm{j}}/V$ is called the scattering length density, ρ_{solv} is the scattering length density of the solvent, V_{P} is the volume of a micelle and $F(\boldsymbol{Q})$ is called the single-particle form factor. The sum in $\rho(\boldsymbol{r})$ is over all nuclei in a volume V. Its value can be calculated using the scattering lengths in Table 3.1 and molecular volumes, which are typically obtained from the molecular density. Scattering length densities for D_2O, poly(ethylene oxide) and the gemini hydrophobic part are given in Table 3.2. It should be noted that the ethylene oxide head groups will be hydrated in a non-ionic micelle and thus the value in Table 3.2 is only a lower bound. The real value will lie somewhere between this and the value for D_2O.

Molecule	Volume / Å^3	$\sum b_j$ / Å	Scattering length density / Å^{-2}
D_2O	30.0	1.914×10^{-4}	6.37×10^{-6}
$–CH_2CH_2O–$	64.7	4.139×10^{-5}	6.39×10^{-7}
$C_{46}H_{92}$	1299.8*	$–3.827 \times 10^{-4}$	$–3.03 \times 10^{-7}$

* See Appendix A10 for calculation of the volume.

Table 3.2: Scattering length densities from molecular densities and atomic scattering lengths.

The single-particle form factor can be solved analytically for several micelle shapes. The only two used in this work are spheres and rods as these are the two most common forms. These are given below. Models for non-ionic surfactants were approximated as core-shell morphologies where the core is assumed to be liquid hydrocarbon and the shell is hydrated polyoxyethylene.

3.2.2.1 Core-Shell Spheres

Solving Equation 3.4 for core-shell spheres gives the analytical SANS function:[84,90]

$$I_{\text{sphere}}(Q) = \frac{N_{\text{P}}}{V_{\text{tot}}} F^2(Q) \qquad 3.5$$

where $I(Q)$ is the normalised scattering intensity (related to Equation 3.4 by the total

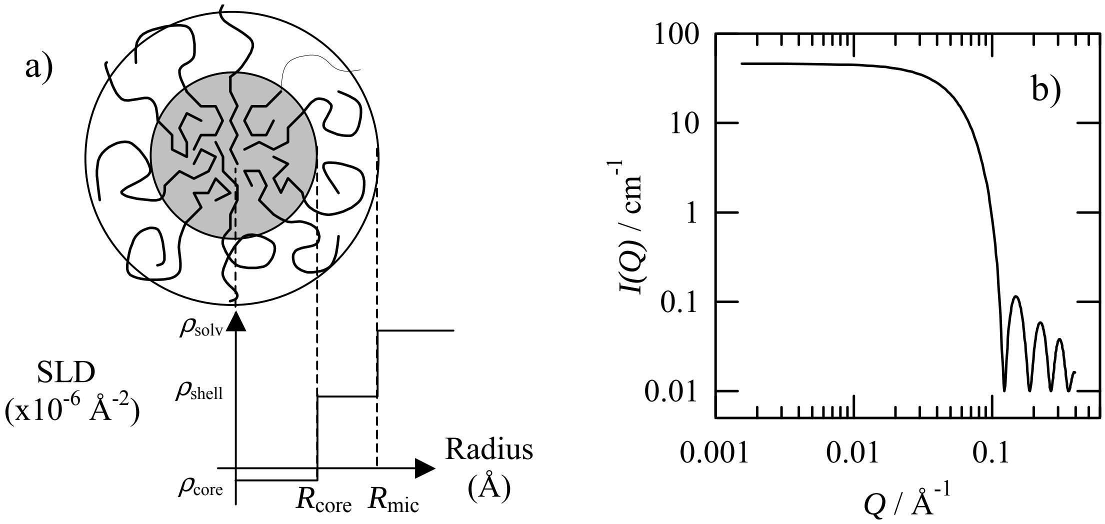

Figure 3.5: a) SLD profile for a Core-shell sphere and b) Its scattering function from Equation 3.5.

sample volume: $I(Q)=1/V_{\text{tot}}\left(\partial\sigma/\partial\Omega\right)=\left(\partial\Sigma/\partial\Omega\right)$). For spheres:

$$F(Q)=\frac{3V(\rho_{\text{sphere}}-\rho_{solv})\,j_1(QR)}{QR}$$

and for core-shell spheres:

$$F(Q)=\frac{3V_{\text{core}}(\rho_{\text{core}}-\rho_{\text{shell}})\,\mathrm{j}_1(QR_{\text{core}})}{QR_{\text{core}}}+\frac{3V_{\text{micelle}}(\rho_{\text{shell}}-\rho_{\text{solv}})\,\mathrm{j}_1(QR_{\text{micelle}})}{QR_{\text{micelle}}}$$

where $\mathrm{j}_1(x)=(\sin x+x\cos x)/x^2$, $V_{\text{i}}=4\pi R_{\text{i}}^3/3$ is the volume of either the core (i = core) or the entire micelle (i = micelle), V_{tot} is the volume of the entire sample and all other variables are shown in Figure 3.5a. Equation 3.5 is a function of the number of micelles, the core radius, the shell thickness and the scattering length densities of the core, the shell and the solvent. Equation 3.5 is shown in Figure 3.5b. Note the sudden drop in intensity at $Q \approx 0.1$ Å^{-1}. This occurs at a length scale of ~4.5/diameter and is a general indication of the length scale being probed.[83]

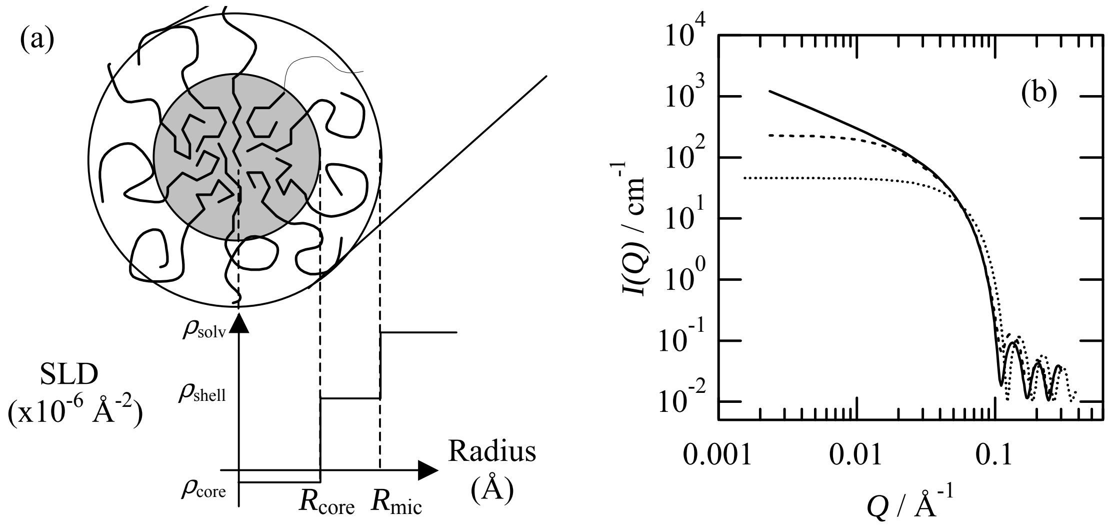

Figure 3.6: a) SLD profile for a Core-shell rod-like micelle and b) The corresponding scattering functions for rod-like micelles with lengths of 200 Å (dashed line) and 2000 Å (solid line). The core-shell sphere from Figure 3.5 is included for comparison (dotted line).

3.2.2.2 Core-Shell Rods

Solving Equation 3.4 for rigid rods gives the analytical SANS function:[84]

$$I_{\text{rod}}(Q)=\frac{N_{\text{p}}}{V_{\text{tot}}}\int_0^{\pi/2}\text{F}^2(Q)\sin\alpha d\alpha \qquad 3.6$$

where α is the angle between the axis of the rod and the scattering vector Q. For rods with a single scattering length density:

$$\text{F}(Q)=2(\rho_{\text{rod}}-\rho_{\text{solv}})V\,\text{j}_{\text{o}}(QH\cos\alpha)\frac{\text{j}_1(QR\sin\alpha)}{QR\sin\alpha}$$

where $\text{j}_{\text{o}}=\sin x/x$, H is half the length, R is the cross sectional radius, ρ_{solv} is the SLD of the solvent. For core-shell rods:

$$\begin{aligned}\text{F}(Q)=&\,2(\rho_{\text{core}}-\rho_{\text{shell}})V_{\text{core}}\,\text{j}_{\text{o}}(QH\cos\alpha)\frac{\text{j}_1(QR_{\text{core}}\sin\alpha)}{QR_{\text{core}}\sin\alpha}\\&+2(\rho_{\text{shell}}-\rho_{\text{solv}})V_{\text{micelle}}\,\text{j}_{\text{o}}(QH\cos\alpha)\frac{\text{j}_1(QR_{\text{micelle}}\sin\alpha)}{QR_{\text{micelle}}\sin\alpha}\end{aligned}$$

The integral is for all α, which is all orientations of the rod with respect to Q. The integral is necessary because rod-like micelles are randomly oriented in solution with no preferred alignment to the beam. Equation 3.6 is shown in Figure 3.6b on the same graph as the core-shell sphere from Equation 3.5. Note that the scattering of the sphere begins to level off at $Q \approx 0.05$, while the scattering from the rod continues to increase to lower values of Q. This is an indication that there is long range order, caused in this case by the length of the rods.

3.2.2.3 Polydisperse particles

The total scattering from a solution of polydisperse micelles is simply the sum of scattering from all micelles. For example, if a solution has spherical micelles, where 40% have a radius of 50 nm and 60% have a radius of 70 nm, then the scattering is simply the average:

$$\begin{aligned} I_{\text{poly}}(Q) &= 0.4 \times I(Q, R = 50\text{nm}) + 0.6 \times I(Q, R = 70\text{nm}) \\ &= \sum P(R) I(Q, R) \end{aligned}$$

where $P(R)$ is the normalised probability that a micelle will have radius R, and $I(Q, R)$ is the scattering from a micelle with radius R. The summation is performed for all values of R. For a continuous distribution the integral form is required:[87]

$$I_{\text{poly}}(Q) = \int_0^\infty P(R) I(Q, R) dR \qquad 3.7$$

Equation 3.7 can be applied equally well to rods, disks and any other micelle shape that has a polydispersity described by a single parameter. Although it is possible to have polydispersity in more than one dimension, many problems arise with interpretation. For example, for core-shell micelles both the core and the shell may be polydispersity or possibly only the shell and not the core. From SANS data there is no method to distinguish between these alternatives and in such cases some *a priori* chemical insight is necessary to make a physically realistic interpretation of the data.

The functional form of $P(R)$ also requires some chemical insight to make a reasonable interpretation of SANS data. For spherical micelles the asymmetric Schulz distribution is often used.[87] The Schulz distribution provides a numerical solution for the scattering function and has only two parameters, which are the average radius of the sphere and the variance of the distribution (or polydispersity). It

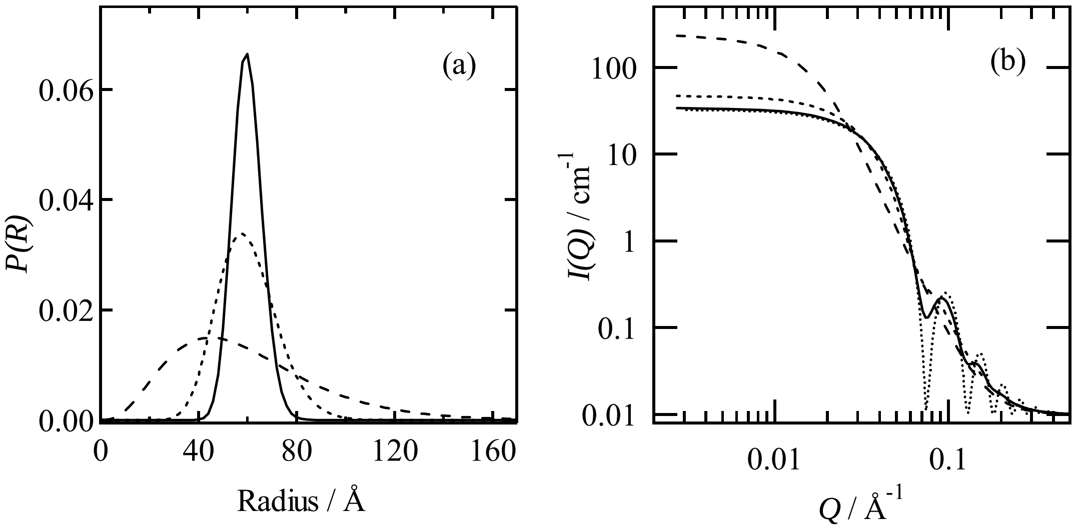

Figure 3.7: a) the Schulz distribution for p = 0.1 (——), p = 0.2 (·····) and p = 0.5 (– – ·), and b) the corresponding scattering functions for polydisperse spheres and monodisperse spheres (·········), with R = 60 Å and $\Delta\rho$ = 6.0 x 10^{-6} Å^{-2}. The effect of polydispersity is to "smear" the data.

is given by:[87,91]

$$P(R) = \left(\frac{z+1}{\overline{R}}\right)^{z+1} \frac{R^z}{\Gamma(z+1)} \exp\left(-\frac{R(z+1)}{\overline{R}}\right) \qquad 3.8$$

where $\overline{R}$ is the average radius, $\Gamma(z + 1)$ is the gamma function and $z + 1 = 1/p^2$. $p = \sigma/\overline{R}$, where σ^2 is the variance from standard statistics. p may take any value between 0 and 1, where 0 is for monodisperse particles. Examples of the Schulz distribution are shown in Figure 3.7a for p = 0.1, 0.2 and 0.5.

Figure 3.7b compares the scattering from polydisperse spheres with the Schulz distribution to scattering from monodisperse. The polydispersity effectively "smears" the scattering function of monodisperse spheres. It should also be noted that the polydisperse scattering function is similar to a short rod-like micelle (also shown) and what would be expected for elliptical micelles with random orientation in solution (not shown but similar to a short rod-like micelle).

3.2.3 Experimental Equipment and Data Reduction

3.2.3.1 Experiment

The SANS data in this thesis was collected at the NIST Centre for Neutron Research (NCNR) in Gaithersburg, Maryland, USA using instrument NG3. The main features of the instrument are shown in Figure 3.8.

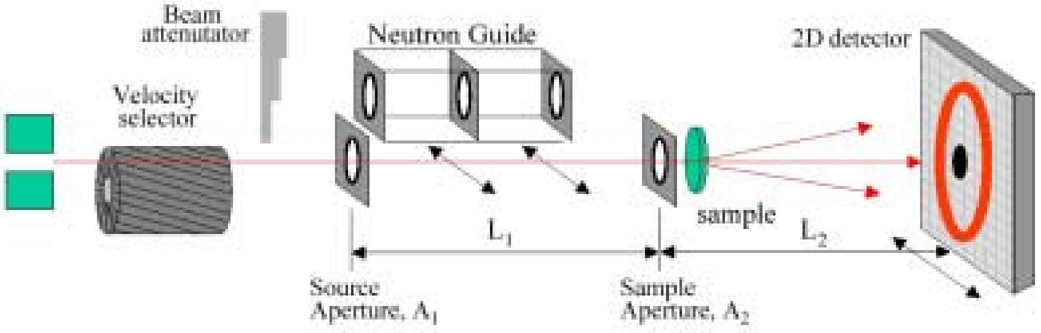

Figure 3.8: Schematic diagram of SANS instrument NG3.[92]

Neutrons were produced by a 20 MW nuclear reactor and passed through a moderator to give them wavelengths in the range required for SANS. They were then passed through a velocity selector that selected neutrons with an average wavelength of 6.0 Å. The neutron wavelengths had a Gaussian profile with a 15 % spread (FWHM). The polydispersity of the neutrons produced a smearing effect on the scattering data as is the case for polydisperse spherical micelles. This can be accounted for during data fitting by replacing $P(R)$ in Equation 3.7 with a gaussian distribution.

The neutrons then pass through the sample. The sample thickness is chosen so as to maximise the scattering but minimise multiple scattering events, which make the previously derived models useless. Optimal sample thickness gives a transmission of approximately 90 % (i.e. 10 % of neutrons are scattered while 90 % pass straight through the sample).[83] We used cylindrical quartz cells with a 1.0 mm path length. This provided a transmission of 89 – 91 %. The cells had a diameter of 1.0 cm with a surface area of $\pi/4$ cm^2 in contact with the neutron beam.

The neutrons were scattered from the sample onto a two dimensional (2D) detector at a distance *d* from the sample. The detector has a grid of 128 x 128 elements to detect neutrons. It is 650 x 650 mm wide giving it a resolution of 5.0 x 5.0 mm^2. The scattering was required as a function of Q so the 2D image was reduced to a 1D function of intensity versus scattering angle and then the scattering angle was converted to Q using the equation $Q = (4\pi/\lambda)\sin(\theta/2)$. The 2D image on the detector was reduced to a 1D function of angle by radially averaging scattering in rings around the direct beam. The averaging was for rings between r and r + dr, where r is the distance from the direct beam and dr is the thickness of an averaged ring. The value of dr is dependent on the resolution of the detector and was 0.5 mm as stated before.

The Q range was determined by the largest scattering angle and the resolution of the detector. The scattering angle is determined by the sample to detector distance and the maximum distance along the detector (from the beam stop to the edge). To maximise this, the detector was offset by 0.2 m and two scattering distances of 1.4 m and 13.1 m used. This provided two overlapping Q ranges of 0.0038 Å^{-1} to 0.0415 Å^{-1} at 13.1 m and 0.0265 Å^{-1} to 0.3705 Å^{-1} at 1.4 m. This gives a combined Q range of 0.0038 to 0.3705 Å^{-1}.

3.2.3.2 Data Collection and Reduction

The raw SANS data must be corrected for many factors and then scaled to absolute intensity. Corrections need to be made for detector efficiency, size of the detector elements, intensity of the neutron beam, thickness of the cell, scattering from air and the cell, area of the beam and attenuation of scattering due to the solution. This process is a simple yet tedious mathematical reduction and is presented below for completeness rather than clarity.

The raw scattering from a sample at a given detector distance is:[83]

$$I_{\mathrm{raw}}(Q) = C_{\mathrm{o}} \times T_{\mathrm{s+c}} d \left[\left(\frac{\partial \Sigma}{\partial \Omega} \right)_{\mathrm{sample}} + \left(\frac{\partial \Sigma}{\partial \Omega} \right)_{\mathrm{cell}} \right] + I_{\mathrm{bkg}} \qquad 3.9$$

where C_{o} is an instrumental constant discussed later, $T_{\mathrm{s+c}}$ is the transmission of the sample and the cell, d is the thickness of the sample determined by the cell manufacturer, $(\partial\Sigma/\partial\Omega)_{\mathrm{sample}}$ and $(\partial\Sigma/\partial\Omega)_{\mathrm{cell}}$ are the scattering cross sections for the sample and the cell respectively. I_{bkg} is the detector background caused by electrical noise and other detector imperfections. It is measured by blocking the beam and subtracted from all raw data.

The value required from Equation 3.9 is $(\partial\Sigma/\partial\Omega)_{\mathrm{sample}}$. The first correction is the subtraction of the cell scattering. This is obtained by collecting the raw scattering from an empty cell:

$$I_{\mathrm{cell}}(Q) = C_{\mathrm{o}} T_{\mathrm{c}} d \left(\frac{\partial\Sigma}{\partial\Omega} \right)_{\mathrm{cell}} + I_{\mathrm{bkg}} \qquad 3.10$$

where T_{c} is the transmission of the beam through the empty. Subtracting Equation 3.10 from 3.9 and rearranging the constants gives:

$$\left(\frac{\partial\Sigma}{\partial\Omega} \right)_{\mathrm{sample}} = \frac{I_{\mathrm{raw}} - I_{\mathrm{bkg}}}{C_{\mathrm{o}} d T_{\mathrm{s+c}}} + \frac{I_{\mathrm{cell}} - I_{\mathrm{bkg}}}{C_{\mathrm{o}} d T_{\mathrm{c}}} \qquad 3.11$$

Next the instrument constant C_{o} is evaluated. C_{o} is the number of neutrons striking the sample per second multiplied by the solid angle of the detector element multiplied by the efficiency of the detector. C_{o} is measured by recording the intensity of the direct beam:

$$\begin{aligned} I_{\mathrm{dir}}(Q) &= \Phi_{\mathrm{o}} A \varepsilon \Delta\Omega \\ &= C_{\mathrm{o}} T_{\mathrm{att}} \end{aligned} \qquad 3.12$$

where Φ_{o} is the neutron flux (neutrons.m^{-2}.s^{-1}), A is the cross-sectional area of the beam striking the sample (m^{-2}), ε is the detector efficiency and $\Delta\Omega$ is the solid angle of a detector element. The intensity of the direct beam is much larger than the scattered intensity and it would otherwise saturate the detector, this is prevented by attenuating the neutron beam and gives rise to the T_{att} term in Equation 3.12. Substituting Equation 3.12 into Equation 3.11 gives:

$$\left(\frac{\partial\Sigma}{\partial\Omega} \right)_{\mathrm{sample}} = \frac{1}{d} \frac{T_{\mathrm{att}}}{I_{\mathrm{dir}}} \left(\frac{I_{\mathrm{raw}} - I_{\mathrm{bkg}}}{T_{\mathrm{s+c}}} + \frac{I_{\mathrm{cell}} - I_{\mathrm{bkg}}}{T_{\mathrm{c}}} \right) \qquad 3.13$$

The correction for C_{o} that leads to Equation 3.13 has a small error in it due to the detector efficiency (e) being slightly different for each detector element. This is corrected by normalisation of Equation 3.13 by a detector "sensitivity" file that is produced by NCNR for the SANS instrument each reactor cycle.

The only terms remaining are the transmissions (T_{att}, $T_{\mathrm{s+c}}$ and T_{c}). T_{att} is a property of the material used for attenuation and is measured by NCNR for the SANS instrument prior to our use. T_{c} is measured at the beginning of the experiment for each detector distance by measuring the intensity of neutrons passing straight through an empty cell and dividing this by the intensity of the direct beam. This may require correction for any attenuation factors. T_{s+c} was collected for each new sample in the same manner.

3.3 Measurement of Phase Behaviour

3.3.1 Microscopic Identification of Mesophases

3.3.1.1 Isotropic and Anisotropic Mesophases

The first step in being able to plot the binary phase diagram for a surfactant system is the identification of different mesophases. They are most easily identified in the laboratory by their optical properties, which are dependent on the micellar structure of the mesophase. Broadly speaking mesophases are either isotropic or anisotropic. Isotropic mesophases are structurally the same in three orthogonal directions. For example, the body centred cubic phase in Figure 3.9a is structurally the same along all three axes. In contrast, an anisotropic phase is structurally different in at least one direction. For example, the lamellar phase in Figure 3.9b is structurally different along the *z*-axis compared to the *x* or *y*-axes. This can be seen more clearly by looking down the *y*-axis and rotating the image so that the bilayers rotate from a vertical alignment to a horizontal alignment. The *x*-axis also reveals anisotropy under these conditions, however, the z-axis looks the same regardless of the angle it is viewed from.

3.3.1.2 Crossed Polarisers

To understand the optical different between isotropic and anisotropic mesophases it is helpful to consider the wave nature of light as shown in Figure 3.10a. For simplicity this wave is represented as an arrow pointing in the direction of oscillation. For a standard light source (such as the sun or a filament bulb) light oscillates in all directions perpendicular to the direction of motion. Light is then “polarised” by being made to oscillate in one direction only. In the laboratory this is accomplished by passing unpolarised light through a film that transmits one polarisation much more than the others. For mesophase identification a second polarising film, called an analyser, is placed with its polarisation direction at right angles to the first so that no light passes through as shown in Figure 3.10b. This arrangement of two polarising films is known as ‘crossed polarisers’.

Error! Objects cannot be created from editing field codes.

Figure 3.9: a) The unit cell of a cubic phase with a body centred cubic structure. The phase is structurally the same along all three orthogonal axes and thus isotropic. b) The lamellar phase is structurally different along the *x* and *y*-axes as seen by rotation of about these axes.

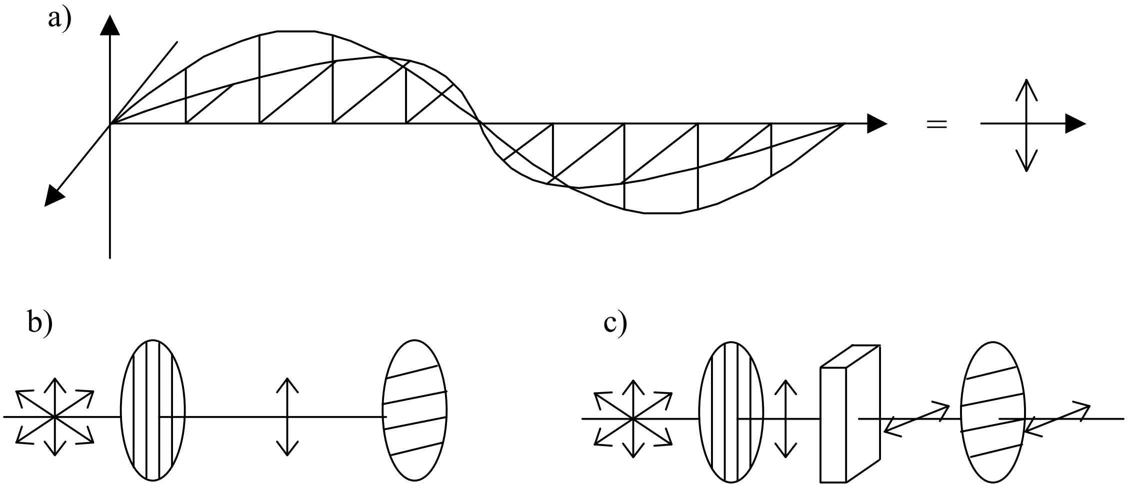

Figure 3.10: a) The wave nature of light is depicted as an electro-magnetic wave where the electric field oscillates perpendicular to the direction that the light is travelling. The magnetic field also oscillates perpendicular to the direction of motion as well as being perpendicular to the electric field vector. For simplicity only the electric field vector is considered and represented as a double headed arrow in the direction of oscillation. b) From a standard light source such as the sun, a filament bulb or a fluorescent tube the light oscillates in all directions. This light can be 'polarised' with a polarising film. A second polarising film rotated 90° will prevent any light from passing through. c) A birefringent sample rotates the plane of polarisation so that at least some of the light passes through the analyser.

3.3.1.3 Optical Properties of Mesophases

When an isotropic sample is placed between crossed polarisers the polarised light will pass through it and be blocked by the analyser. Thus, *an isotropic mesophase appears dark between crossed polarisers*. However, when an anisotropic sample is placed between crossed polarisers it rotates the plane of polarisation so that some of the light will pass through the analyser, as shown in Figure 3.10c. Thus, *an anisotropic mesophase appears bright between crossed polarisers*. The rotation of polarised light is known as optical birefringence.

The cause of birefringence in an anisotropic sample is complex and depends on many factors such as sample thickness and orientation. The important point though, is that isotropic mesophases (eg I_1 and V_1) will appear dark when viewed between crossed polarisers, while anisotropic mesophases (eg H_1 and L_α), are birefringent and will appear bright when viewed between crossed polarisers.

Anisotropic mesophases cannot be distinguished from each other by their optical birefringence alone and identification is made by observing their "texture" using an optical microscope with crossed polarisers fitted to it. The microscopic texture is determined by the different defects that each mesophase forms and is correlated empirically by comparison to samples previously identified by other methods. Several examples of optical textures have been collected by Rosevear[93] and are reproduced by Laughlin[69] with additional images. A few examples of microscopic textures of the H_1 phase and the L_α phase recorded on our microscope are given in Appendix A3.

Cubic phases are isotropic and thus transparent between crossed polarisers. However, they can be identified by correlating their lack of birefringence and their flow properties. Cubic phases do not flow when small forces are applied to them and they can be regarded as behaving like a solid under such conditions. Under the microscope this manifests itself as deformed air bubbles that are trapped in the cubic phase. Since the cubic phase is so viscous the bubbles are unable to take on their typical spherical shape. Identification of a cubic phase is thus straight forward. However, to differentiate between a micellar cubic phase (I_1) and a bicontinuous cubic phase (V_1) is more difficult and usually requires other phase information. For example, I_1 forms on the water rich side of H_1, while V_1 always forms on the surfactant rich side of H_1. The H_1 phase is a very common surfactant mesophase and it is usually not difficult to distinguish between I_1 and V_1 provided that the order of phases is know.

3.3.1.4 Penetration Experiments

The determination of the number and order of phases formed by a surfactant at a specific temperature was by penetration experiments.[94] A small sample of surfactant is placed on a microscope slide and covered with a cover slip. Water is placed at the edge of the cover slip and drawn under it by the capillary force. The water contacts the surfactant which immediately begins to dissolve. A concentration gradient forms from the water at the edge of the cover slip to the surfactant in the middle. Since the concentration spans the range from pure water to pure surfactant *all* possible phases for the surfactant must form. This makes it almost impossible for a mesophase to not form and be identified. However, the relatively large perimeter of the cover slip means evaporation is often significant and low viscosity mesophases can produce complex mixing effects that can easily change the order of phases.

3.3.1.5 DIT Method

A modified method of the penetration experiment that overcomes the evaporation problem is the Diffusive Interfacial Tension (DIT) method developed by Laughlin.[94] Basically, the microscope slide and cover slip are replaced with a long, flat, thin capillary with an internal thickness of approximately 0.02 to 0.2 mm. The surfactant is melted and drawn into one end of the capillary whilst water is forced into the other end (see below for full procedure). The water is then forced to contact the surfactant and all mesophases form, as with the penetration method. Over time the mesophases broaden significantly. They can then be identified using optical microscopy as discussed previously.

The advantage of the DIT method is the phases effectively form in one dimension and the possibility of complex mixing effects is largely reduced. It is also easier to prevent evaporation, and thus leave the sample for longer periods by sealing the ends.

3.3.1.6 Experimental Equipment

Phase identification was conducted on a Leica DMLB optical microscope with a 100W lamp. It was fitted with crossed polarisers and a slightly offset λ-plate to highlight colours from birefringent phases. An aperture below the condenser was used to increase sample contrast when necessary. Images were recorded using a Leica DC300 digital camera.

Sample temperature was controlled using a Linkam warm stage and controller. DIT studies were carried out in drawn glass capillary tubes with internal dimensions of 50 x 4.0 x 0.2 mm or a short path length cell with internal dimensions of 45 x 10 x 0.1 mm supplied by Starna Pty. Ltd. The short path length cell was made from quartz and came in two pieces for easy loading and cleaning.

3.3.2 Phase Boundaries

Once the order of phases is known the determination of composition at phase boundaries can be performed by a number of methods that fall into the two general categories of either constant temperature (isothermal) or constant concentration (isoplethal). Isothermal studies are typically conducted by making a surfactant sample and allowing it to equilibrate at the temperature of interest before identifying the phase. Phase boundaries are located by tediously diluting the solution until the next phase is found. Isoplethal studies, however, are carried out by making a series of samples at various surfactant concentrations. Phase boundaries are identified by heating the samples and recording the temperatures of phase changes.

Traditional phase study methods on surfactants have the disadvantages of being slow due to the slow equilibration times of surfactant mesophases. However, a much faster method based on the DIT experiment has been developed by Laughlin *et al.*[95] called DIT-NIR (DIT near IR) The basic principle is that the mesophases are allowed to form in a DIT cell and then the surfactant composition at the phase boundary is measured using an infrared (IR) spectrometer.

3.3.2.1 DIT-NIR

The small volumes in the DIT cell are measured using a Fourier Transform Infrared (FTIR) with an attached microscope. In practice, the concentration of water is measured and then converted to surfactant concentration using a calibration (see below).

From basic solution spectroscopy it is known that absorption is a function of the sample thickness and the sample concentration. To make the sample concentration the only parameter being measured the sample thickness is kept constant. Thus the DIT cell is made from quartz with a very uniform path length. The advantage of a quartz cell is that it can be made with a very short yet consistent path length. The disadvantage is that it is opaque to large section of the IR spectrum, specifically the main water peaks. This is overcome by using a combination water band with a very broad peak at about 5150 cm^{-1}. The peak is a combination of the H_2O antisymmetric vibration near 3600 cm^{-1} and the H_2O scissors deformation near 1640 cm^{-1},[96] and few surfactants absorb in this region, even if they posses an OH group because they lack the same bending motion found in water. In practice the concentration is measured by integrating over the range 5400 to 4600 cm^{-1}.

3.3.2.2 Calibration

A calibration curve is used to convert the integrated absorption spectra into water concentration and then into surfactant concentration with units of wt%. The water calibration curve was made by recording absorption versus water concentration in wt%. The calibration standard used by Laughlin was octyldimethylphosphine oxide because it is soluble over the entire concentration range, it has no mesophases above room temperature and it is easy to purify. We used hexadecyltributylammonium bromide ($C_{16}H_{33}N(C_4H_9)_3Br$) for the same reasons and because we had it available at the time.[97] Other standards were also tested but found to be inadequate for various reasons, for example, acetone was too volatile to accurately weigh out its concentration, poly(ethylene glycol) was too viscous to load into the cell and glycerol had a broad peak at about 4780 cm^{-1} that overlapped with the water peak making integration impossible.

The calibration spectra and graph are shown in Figure 3.11a and b for four different water concentrations. The calibration is linear with concentration. The line of best fit from a linear regression is also shown on this graph. The surfactant concentration (C_{surf}) for a binary mixture is simply 100 wt% minus the water concentration (C_{water}). This gives:

$$C_{\mathrm{surf}} = 100\left(1 - \frac{\mathrm{Area} - \mathrm{Area}_{\mathrm{o}}}{\mathrm{Area}_{\mathrm{max}} - \mathrm{Area}_{\mathrm{o}}}\right)$$

where $\mathrm{Area}_{\mathrm{max}}$ is the peak area at 100 wt% water and $\mathrm{Area}_{\mathrm{o}}$ is the peak area at 0 wt% water. This value is typically non-zero due to a residual from the integration process.

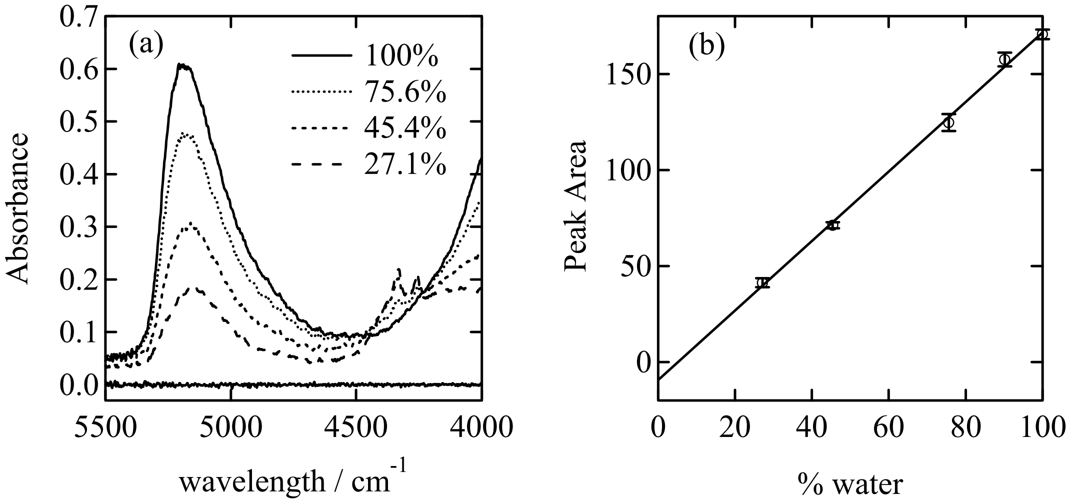

Figure 3.11: a) Calibration spectra for water at 27.1 wt% (- -), 45.4 wt% (···), 75.6 wt% (·····) and 100% (—) and b) peak area vs water concentration (wt%) from integrating spectra in (a) from 4600 to 5400 cm^{-1}.

3.3.2.3 Experimental Procedure

One end of the DIT cell is loaded with surfactant and the other end with water. The surfactant is loaded by melting it and using capillary action to draw it about one third to two thirds into the DIT cell. The surfactant end is then sealed with Epon 1004 from Shell (which is a low impurity resin that melts at ~100°C) by melting the resin and smearing it on the end of the cell. The water is loaded into the other end of the capillary by placing the capillary in a vacuum desiccator with a drop of water next to the opening of the capillary. The chamber is then evacuated so that a vacuum exists in the capillary and the water drop is brought into contact with the capillary opening so that it covers the entire opening. Air is then slowly reintroduced into the chamber and the air pressure forces the water into the capillary. There is a small gap (about 2mm) between the surfactant and the water. The water is made to contact the surfactant either by mechanical agitation or by placing it in a centrifuge. This end is then sealed like the other, to prevent evaporation.

The mesophases are allowed to broaden over time (~10 hours is sufficient). The phases are identified with an optical microscope fitted with crossed polarisers and the position of the phase boundaries recorded as a function of distance along the DIT cell. The cell is then placed in the FTIR-microscope and the water concentration measured at the phase boundary. In practice, two-phase coexistence regions do not occur in

DIT cells and there is a concentration discontinuity at the phase boundary. To measure the concentration more accurately it is necessary to measure the concentration as a function of distance from the interface and then extrapolate back to the edge of the mesophase. The concentration of water is then converted to surfactant concentration.

3.3.2.4 Experimental Equipment

Spectra were collected with a Brukner FTIR-microscope fitted with a microscope translation stage that was adjustable to approximately 0.1 mm. The DIT cell was a 40 x 10 x 0.02 mm quartz cell purchased from Starna.

The cell was cleaned by first removing any excess resin (either physically or by soaking in fresh dichloromethane). It was then cleaned in boiling concentrated nitric acid for greater than three hours (often much longer), which oxidises anything in the cell. The cell was then rinsed in copious amounts of MilliQ water and dried in an oven. It is essential that the cell is clean before loading with surfactant to ensure a clean water/surfactant interface. If the cell is dirty neither the water nor the surfactant will wet the glass during sample preparation.

3.3.2.5 Comparison to a Known Phase Diagram

The calibration and temperature control of our experimental set up was tested on $C_{12}E_8$ as a function of temperature. $C_{12}E_8$ was chosen because it can be purchased in a highly pure form (>98 %) from Fluka Chemicals and its phase behaviour is well known.[71] Before conducting the DIT-NIR study a conventional penetration experiment was conducted to ensure that all mesophases form. These phases were also studied as a function of temperature to ensure that the mesophases melt at the correct temperatures. This is a fast and efficient means to test the purity of a sample, since the phase behaviour changes noticeably with very small quantities of impurities.

The initial penetration study revealed a melting point for the hexagonal phase that was approximately 30 °C below the literature value. From chromatography (see Section 3.6) it was found that the impurities are due to break down of the polyoxyethylene head group. A new sample was ordered and similarly tested. It was found to behave as it should and was used in the phase studies.

The phase diagram of $C_{12}E_8$ from Mitchell *et al.*[71] is reproduced in Figure 3.12 with the phase boundaries from DIT-NIR shown as open circles. There is reasonably good agreement between the two except above ~55°C, where temperature equilibration becomes difficult.

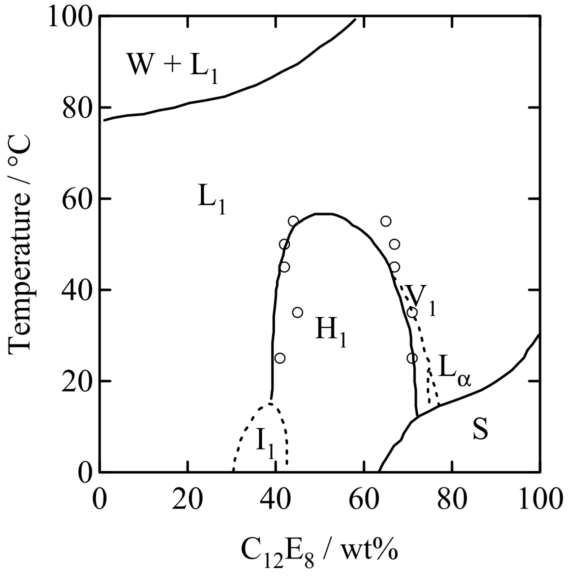

Figure 3.12: Phase diagram of $C_{12}E_8$ from Mitchell *et al.*.[71] Open circles are the phase boundaries as determined from DIT-NIR. Reasonable agreement is achieved at low temperatures, although agreement becomes poor above ~55 °C due to poor temperature equilibration.

3.4 Cloud Temperature Measurements

Cloud temperatures were measured by heating 1 wt% surfactant solutions in a temperature bath and observing when the solutions first go cloudy. The onset of clouding was determined visually by reference to a pure water sample. In some cases the surfactant became very viscous as the solution approached the cloud point, increasing the time of separation and making identification of the cloud point extremely difficult. In these cases the cloud point was determined by measuring the turbidity as a function of temperature with a Carey UV-Vis spectrometer fitted with a thermostated cell holder. This method is slower but allows extrapolation to the cloud temperature.

It should be noted that the cloud temperature at 1 wt% is an approximation to the critical temperature, which depends on the concentration. This approximation was made necessary because of slow separation and possible surfactant decomposition at elevated temperatures.

3.5 Viscosity Measurements

The viscosity of a fluid can be thought of as a measure of its resistance to flow. A fluid that does not flow easily is said to be highly viscous (eg honey) while a fluid that flows easily is said to have low viscosity (eg water). The viscosity can be defined more precisely by considering a liquid confined between two parallel plates. The bottom plate is held stationary while a shear force is applied to the top plate (i.e. a force per area parallel to the plate). Any plane in the liquid will have a velocity gradient proportional to the applied force. The velocity gradient is called the shear rate and the proportionality constant is the viscosity (η). Mathematically this is:[78]

$$\frac{F}{A} = \eta \frac{dv}{dx}$$

where F/A is the shear force per area applied to the top plate, v is the velocity of solution at a distance x from the shearing plate. If the viscosity of a liquid is constant for all shear rates it is called a Newtonian liquid. Although this is rarely the case in colloidal systems it is often invoked in theories as ideal solution behaviour.

Viscosity measurements were made using a capillary viscometer submersed in a temperature controlled water bath with the temperature stable to ± 0.5 °C. The capillary viscometer was operated as shown in Appendix A4. The basic principle of operation is to measure the flow time of a known volume of solution through a thin glass capillary, which for a Newtonian liquid is proportional to the viscosity. For this work we were only interested in the viscosity of a surfactant solution divided by the viscosity of water, which is called the relative viscosity. This is simply the ratio of the flow times for the surfactant solution and water.

It should be noted that some solutions in this thesis are non-Newtonian liquids, making the relationship between viscosity and flow time much more complicated. However, this is not a major concern since we are only interested in general trends and not absolute values.

3.6 High Performance Liquid Chromatography (HPLC)

A flooding experiment on a supposedly pure $C_{12}E_8$ sample in our lab found the melting point of the hexagonal phase (H_1) was only 31–33 °C, which is much lower than the literature value of 59 °C reported by Mitchell *et al.*.[71] This discrepancy was attributed to impurities in the sample. In particular, it has been shown that poly(ethylene oxide) breaks down over long periods of time by a variety of mechanisms that result in depolymerisation or fission of the polymer chain.[98] We tested this by ordering a new sample of $C_{12}E_8$ from Fluka Chemicals and comparing its composition to the original surfactant in question. The purity of the new sample was tested by measuring the melting point of its hexagonal phase and comparing this to the published value.

Comparison of the two surfactants was made using a chromatographic technique to separate the individual surfactants based on the length of the polyoxyethylene head group. High Performance Liquid Chromatography (HPLC) was chosen for this task. Other chromatographic techniques such as Gas chromatography (GC) were also considered, however, available equipment was unsatisfactory for separation of surfactant by head groups.

The separation technique was a modification of the procedure of Desbène *et al.*.[99] The experiment is shown in block diagram form in Figure 3.13. The Eluant was a 20:80 v/v mixture of water in acetonitrile. The more common methanol/water and acetone/water eluants where not used because these only allow separation of the hydrophobic tail and are thus useless for separation of surfactants with different head groups. The eluant was pumped at 0.7 mL/min. A 5 μL injection loop was used to inject 1 wt% samples into the column. Separation was on a C_{18} reverse phase column from Waters (3.9 x 150 mm C_{18} 5 μm column, Part number WAT046980). A C_8 column would have been preferable for finer separation, but is not necessary for establishing the purity of surfactants, as was undertaken here. The elution times were collected using a refractive index detector, also from Waters.

The results of the separation are shown in Figure 3.14. The separation shows that there is a small amount of impurity in the new sample whilst the older sample has significant impurities about the main peak.

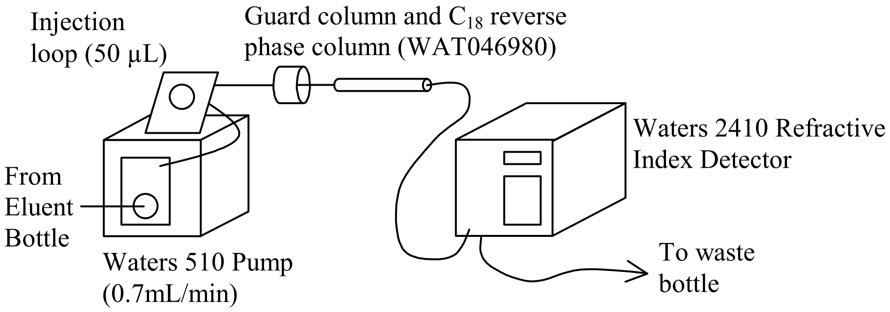

Figure 3.13: Block diagram of the HPLC setup for the determination of decomposition of nonionic surfactant.

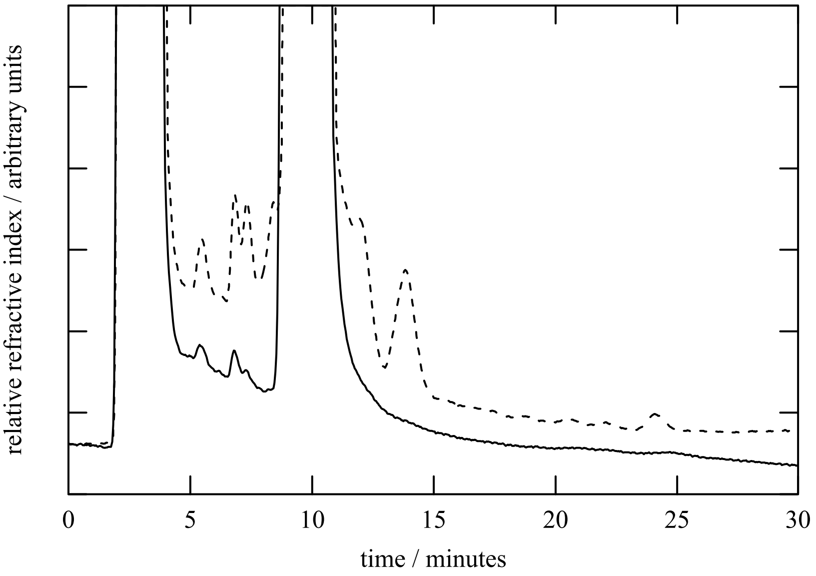

Figure 3.14: Separation of the new, “pure” sample of $C_{12}E_8$ (solid line) and the old, “impure” sample (dashed line). The first large peak (off scale) is the solvent peak (water) and the second large peak is $C_{12}E_8$. All additional peaks are impurities. Note that even in the new $C_{12}E_8$ there is still a small amount of impurity.

Chapter 4: Critical Micelle Concentrations (CMCs)

4.1 Introduction

This chapter investigates the concentration that micelles first form (the CMC). Specifically, this chapter is concerned with the values of the CMCs, how they behave when mixed with conventional surfactants and how they compare to conventional nonionic surfactant behaviour.

4.2 Results

4.2.1 CMCs of Nonionic Gemini Surfactants

An initial attempt was made to measure the CMC of $\mathrm{Gem}_{20}\mathrm{E}_{15}$ by surface tension, using the Wilhelmy plate. The measurements revealed extremely slow equilibration times. For concentrations less than 10^{-6} M the surface never came to equilibrium, even after several days. The slow equilibration times made it impossible to collect data in a reasonable time period without solution evaporation and contamination of the plate.

The slow equilibration times are probably caused by the large size of the gemini surfactants (i.e. MW > 2000) and their low concentrations (i.e. conc $\leq 10^{-5}$ M) combining to produce very slow diffusion of surfactant molecules to the surface. Another factor is the polydispersity of the head groups, which is also known to cause difficulties in surface tension measurements.[70] CMC determination by this method was thus abandoned and the CMCs were determined by the pyrene fluorescence method instead.

Figure 4.1 shows the pyrene $I_{1/3}$ ratio versus the surfactant concentration for $Gem_{20}E_{10}$, $Gem_{20}E_{15}$, $Gem_{20}E_{20}$ and $Gem_{20}E_{30}$ at room temperature. The $I_{1/3}$ values are offset in multiples of 0.2 for clarity and the concentration axis is on a logarithmic scale due to the large range covered. CMCs were found by extrapolation of $I_{1/3}$ above the CMC back to where it becomes constant at ~1.8. This is the first deviation from a constant $I_{1/3}$ and the first occurrence of micelles. The CMCs are given in Table 4.1 with error estimates from the extrapolation.

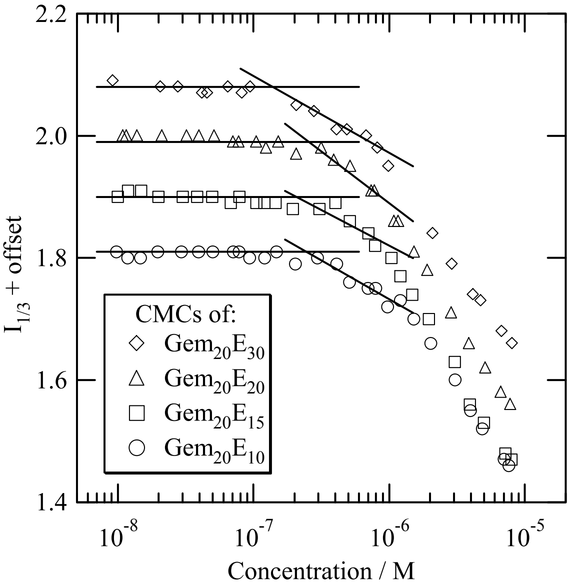

Figure 4.1: $I_{1/3}$ vs surfactant concentration curves for $Gem_{20}E_{10, 15, 20 \& 30}$ at 25°C.

The CMCs are all very low compared to conventional 12 carbon, nonionic surfactants, which have typical CMCs of 10^{-4} to 10^{-5} M. The gemini surfactants also have CMCs much lower than the lowest recorded conventional nonionic surfactant, $C_{16}E_6$, which has a CMC of 10^{-6} M.[70] Conventional surfactants with lower CMCs have not been reported, most probably due to poor solubility.

The CMC was not observed to change within experimental error as the degree of ethoxylation was increased from 10 to 30, there may even be a slight decrease, which has been observed in conventional nonionic surfactants,[70] although only rarely.

	10	**15**	**20**	**30**
CMC ($\times 10^{-7}$ M)	2.5 ± 1.0	2.0 ± 1.0	2.8 ± 1.0	1.5 ± 1.0

Table 4.1: CMCs for Gem$_{20}$E$_m$ surfactants with changing m. The CMCs are all ~2 x 10^{-7} M with no noticeable change with ethoxylation number (within experimental error).

Three points need to be made regarding measurement and extrapolation of the CMCs. Firstly, the drop in $I_{1/3}$ occurs over a concentration range of two to three orders of magnitude. This is a very slow change compared to measurements made on conventional nonionic surfactants with CMCs ≥ 10^{-4} M.[79,82] The reason for this can be understood by considering how the pyrene fluorescence method works. The drop in $I_{1/3}$ occurs at the CMC because the pyrene is solubilised in the newly formed micelles. However, in these experiments the pyrene concentration is ~3 x 10^{-7} M, which is barely the concentration of surfactant and certainly much less that the concentration of micelles. As a consequence, there are too few micelles to solubilise the pyrene even after the surfactant concentration is increased by a factor of 10. Also, because the CMCs are so close to the saturation concentration of pyrene a partitioning of the pyrene between water and micelles occurs. These two factors are not seen with much higher CMCs at 10^{-4} M because only a small increase in the surfactant concentration produces enough micelles to solubilise almost all the pyrene.

Secondly, some researchers have argued that the CMC should be taken at the concentration that $I_{1/3}$ falls to half its original value (~1.8) with respect to its final value (~1.2). This assignment is typically used so that CMCs from this method coincide with CMCs measured from other techniques such as surface tension or conductivity. However, there is no theoretical justification for this assignment and considering the points made in the previous paragraph it is clear that micelles begin to form as $I_{1/3}$ begins to decrease, and that the CMC should be assigned as the first drop in $I_{1/3}$.

Thirdly, significant adsorption of surfactant to the glassware is expected at concentrations of 10^{-8} M and probably even at 10^{-7} M. As surfactant is adsorbed it will be depleted from solution and reduce the surfactant concentration, effectively making the CMCs appear larger. If this effect occurs it may be large enough to increase the CMC from 10^{-10} M or 10^{-8} M to the values observed. The values need to be experimentally verified – this will be done later.

4.2.2 CMCs of Gemini Surfactants Mixed with Conventional Surfactants

The CMC of $Gem_{20}E_{30}$ mixed with a conventional $C_{18}E_{30}$ nonionic surfactant was measured as a function of mole fraction. Figure 4.2 shows $I_{1/3}$ versus concentration curves, offset in multiples of 0.1 for clarity. The CMCs are shown in Figure 4.3 as a function of mole fraction of $C_{18}E_{30}$. The open circles are the experimental values with the estimated error from the CMC extrapolation. The left most data point is the CMC of unmixed $Gem_{20}E_{30}$ at 1.5 x 10^{-7} M. The right most data point is the CMC of unmixed $C_{18}E_{30}$ at 4.1 x 10^{-6} M. As the mole fraction of the gemini surfactant is increased (i.e. moving from right to left across the graph) a rapid drop in the CMC occurs. This is highlighted by considering the CMCs at mole fraction of 1.0 and 0.98 on the graph. This is only 2 mole % addition of gemini surfactant but causes a factor of two decrease in the CMC. Further additions produce a slightly smaller decrease in the CMC until it approaches the limiting value for the unmixed gemini surfactant. The CMC of the mixed surfactant never went below this value.

The curve fit to the data in Figure 4.3 is the ideal mixing Equation (Equation 2.18), where x_1 is the mole fraction of $C_{18}E_{30}$, and CMC_1 and CMC_2 are the CMCs of $C_{18}E_{30}$ and $Gem_{20}E_{30}$ respectively. The applicability of ideal mixing is clearly seen from the CMCs greater than 10^{-6} M (i.e. $x_1 \geq 0.85$) and are thus not affected by the possible adsorption problems for concentrations less than 10^{-7} M that were mentioned previously.

In fact the ideal mixing equation can provide experimental verification that the CMCs less than 10^{-6} M are correct, by comparing the ideal mixing behaviour that would occur if the gemini surfactant CMC was much lower. These are shown in Figure 4.3 for $CMC_2 = 10^{-8}$ M and 10^{-10} M. The curve for $CMC_2 = 10^{-8}$ M (dashed line) drops much more rapidly than the data points at the undisputed concentrations (i.e. $x_1 \geq 0.85$). The curve for $CMC_2 = 10^{-10}$ M (dotted line) is even more convincing as it simply follows the axis down to CMC_2 and almost levels off. This difference between the ideal mixing curve fit to the experimental values and the ideal mixing curve for much lower gemini surfactant CMCs demonstrates that adsorption is not a significant problem.

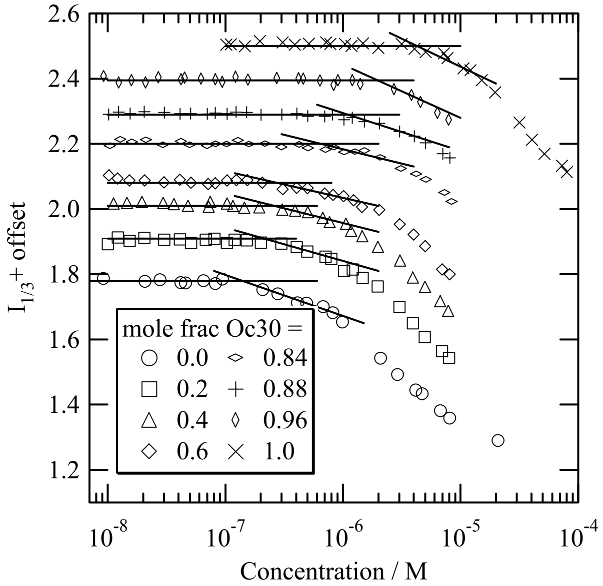

Figure 4.2: $I_{1/3}$ vs concentration curves for $Gem_{20}E_{30}$ mixed with $C_{18}E_{30}$ at room temperature. Values are offset for clarity.

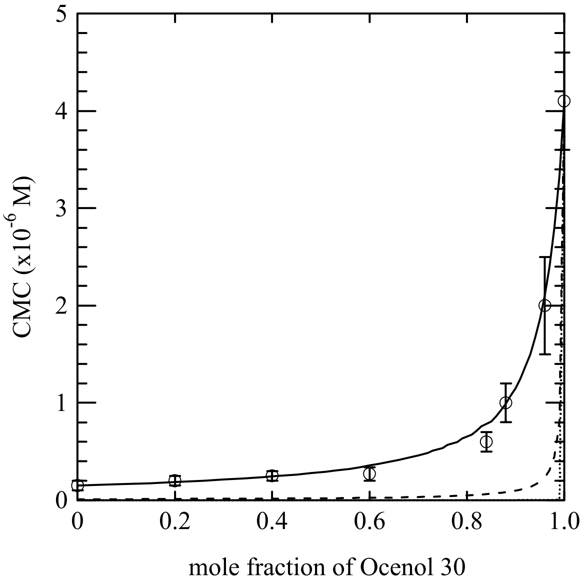

Figure 4.3: CMCs for $Gem_{20}E_{30}$ mixed with $C_{18}E_{30}$ versus mole fraction of $C_{18}E_{30}$. The solid line is the ideal mixing equation (Equation 2.18) fit to the data. Also shown are the ideal mixing curve (Equation 2.18) if the gemini surfactant CMC was 10^{-8} M (dashed line) and 10^{-10} M (dotted line).

The CMC of $Gem_{20}E_{30}$ mixed with a conventional ionic surfactant was also measured. The ionic surfactant was WC60 provided by Huntsman corporation. It is an ethoxylated nonylphenyl with a sulphate head group and ammonium counter-ion. The $I_{1/3}$ versus concentration curves are shown in Figure 4.4, and its mixing behaviour is shown in Figure 4.5 on a log scale. As with the conventional nonionic surfactant, $Gem_{20}E_{30}$ obeys the ideal mixing equation when mixed with ionic surfactants. The drop in the CMC is much more pronounced than for the nonionic surfactant. This is due to the large difference between the two unmixed CMCs. This further highlights the usefulness of mixing low CMC surfactants, such as gemini surfactants, with conventional surfactants to lower their CMCs.

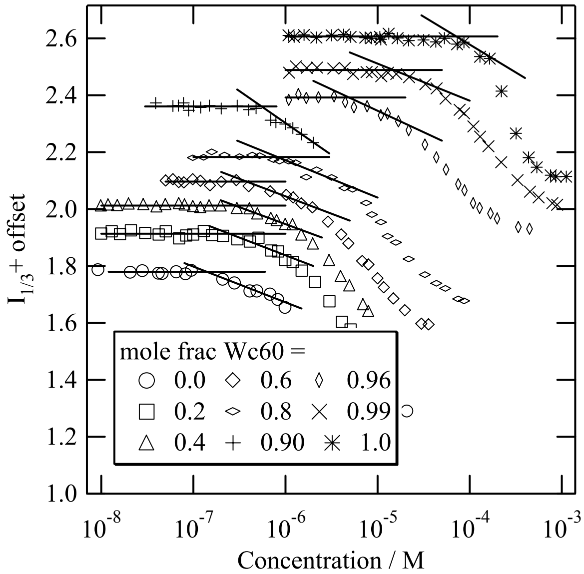

Figure 4.4: $I_{1/3}$ vs concentration curves for $Gem_{20}E_{30}$ mixed with Alkanate WC60.

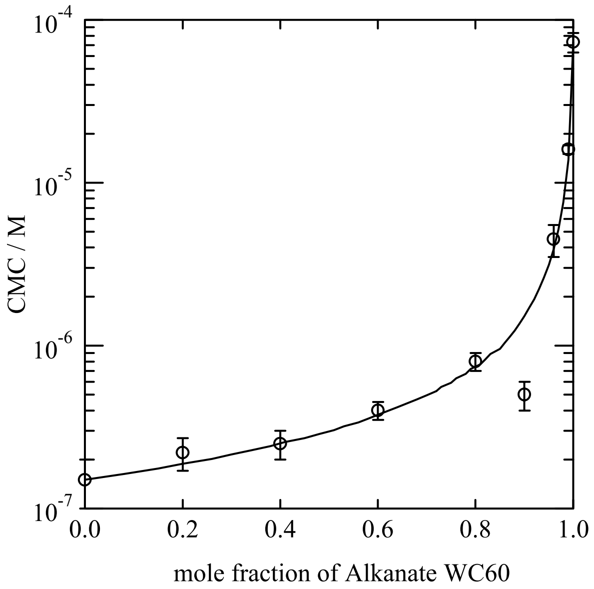

Figure 4.5: CMCs for Gem$_{20}$E$_{30}$ mixed with Alkanate WC60, as a function of mole fraction of Alkanate WC60. The solid line is the ideal mixing curve plotted using Equation 2.18

4.3 Discussion

One of the main aims of this work was the comparison of the physical chemical properties of gemini surfactants to conventional surfactants. For there to be a benefit using gemini surfactants its CMC must be less than *half* the CMC of the corresponding conventional surfactant.[8] Thus for the comparison of gemini to conventional surfactants, the CMCs will be expressed in moles of tail per litre as opposed to moles of surfactant molecules. This simply means multiplying the CMCs of the gemini surfactants in Table 4.1 by two.

Comparison of conventional surfactant CMCs to gemini surfactant CMCs requires them to posses the same number of carbon atoms per tail (n_c) and the same average number of ethylene oxide units per head group (n_{EO}). However, reliable CMCs for conventional nonionic surfactants with n_c greater than 16 have not been published. Comparison must therefore be made by extrapolation of CMCs from conventional surfactants with shorter tail lengths. The most widely studied series of conventional nonionic surfactants are linear alcohols with six ethylene oxide groups in the head group (i.e. C_nE_6) and these will be used as the reference data.

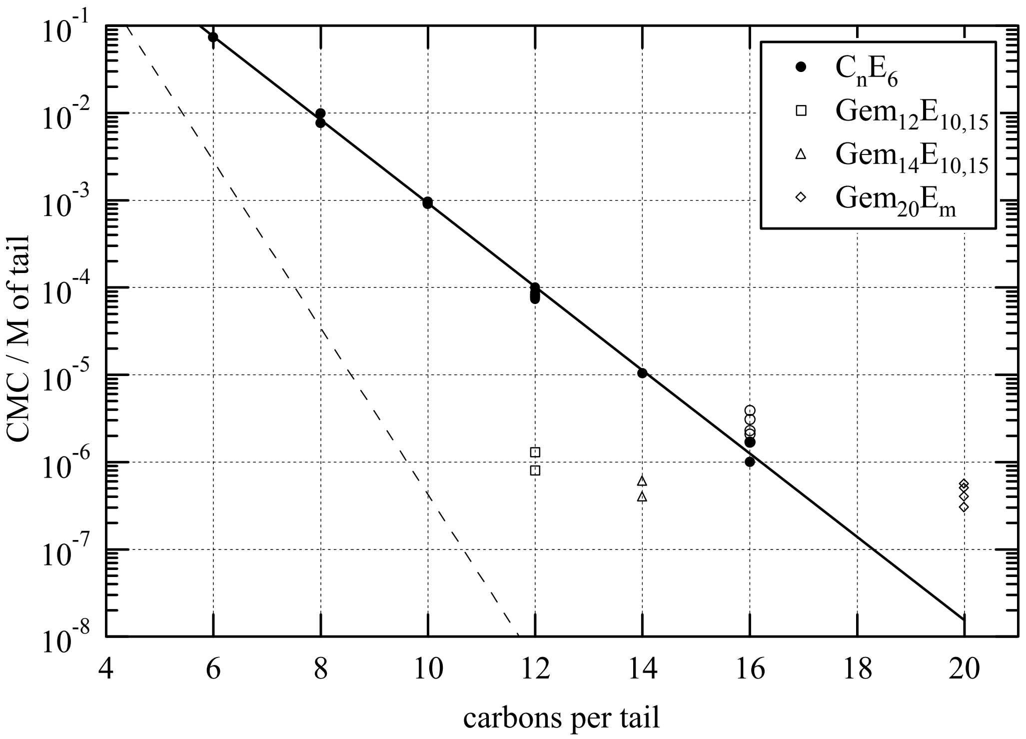

Figure 4.6: CMC versus carbon atoms per tail. Showing C_nE_6 (solid circles),[70] $C_{16}E_m$ (open circles),[70] $Gem_{20}E_m$ (open diamonds), $Gem_{14}E_m$ (open triangles) and $Gem_{12}E_m$ (open squares). The solid line is the best fit to the C_nE_6 data and the dashed line is the theoretical CMCs for gemini surfactants from Equation 2.17)

Figure 4.6 shows CMC vs n_c on a log plot for the gemini surfactants (Table 4.1). The solid circles are the conventional nonionic surfactant CMCs with a line of best fit demonstrating the log*CMC* vs n_c behaviour. Note that log*CMC* vs n_c is linear and *not* CMC vs n_c. This log dependence means a large decrease in the CMC can be achieved by a small increase in n_c.

Use of the C_nE_6 surfactant CMCs for comparison requires a correction for the different ethoxylation numbers of the gemini surfactants. Figure 4.7 shows CMC vs n_{EO} for C_{16} surfactants.[70] These points are also shown in Figure 4.6 as open circles for comparison. The CMC changes by less than a factor of four over the entire range from E_6 to E_{21}. This change is relatively small compared to the decrease from the addition of two carbon atoms to an alkyl tail. Because the CMCs of the gemini surfactants were not observed to change with increasing n_{EO} and because the change is small in conventional surfactants only a small correction is required for comparison. This correction will not be applied directly to the graph but made in the text as comparison is made.

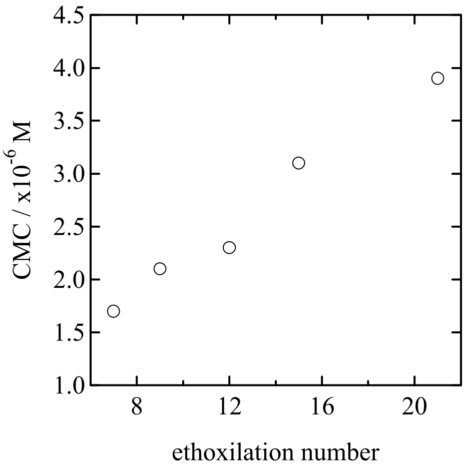

Figure 4.7: CMC versus ethylene oxide units per tail for a conventional C_{16} surfactant showing a modest increase with ethoxylation number.[70]

Also shown in Figure 4.6 are the CMCs of the $Gem_{12}E_m$ and $Gem_{14}E_m$ series. *m* is equal to 10 and 15 (the larger CMC is 15 in both cases). The synthesis and CMC measurements for the $Gem_{12}E_m$ and the $Gem_{14}E_m$ series were conducted by Dr Tim Davey using the same methods as for $Gem_{20}E_m$.[*]

Figure 4.6 shows the CMCs of the $Gem_{20}E_m$ series are all larger than the extrapolated conventional C_{20} nonionic surfactant. Even with a factor of four correction for the larger value of n_{EO} they are still only the same as the extrapolated value of a conventional C_{18} surfactant. The CMCs of the $Gem_{12}E_m$ and $Gem_{14}E_m$ series are all less than the conventional C_{12} and C_{14} nonionic surfactants even without correcting for n_{EO}, which would make the gemini surfactant CMCs even lower still.

The greatest gain is for the $Gem_{12}E_m$ series which are two orders of magnitude smaller than the conventional C_{12} surfactant. The gemini CMCs are about the same as for $C_{16}E_6$ making it equivalent to the lowest conventional surfactant. In terms of reduction in CMC with respect to conventional surfactants it certainly produces the greatest gain. However, the outright lowest CMC requires the hydrophobic tail to be as long as solubility limits will allow as demonstrated by the very low CMCs produced by the $Gem_{20}E_m$ series of surfactants.

---

[*] Formerly of University of Sydney, where he conducted this work

The theoretical CMCs for gemini surfactants (Equation 2.17) is shown in Figure 4.6 as a dashed line for comparison to the gemini surfactant CMCs. The gemini surfactant CMCs all lie well above the line demonstrating that the assumption $\Delta G^{o}_{\mathrm{gem}} = 2\Delta G^{o}_{\mathrm{conv}}$ is wrong. Intuitively this means that the gemini surfactants do not "want" to form micelles as readily as conventional nonionic surfactants. There is some barrier or restriction that makes it energetically more favourable for the gemini surfactants to remain in solution in preference to forming micelles.

A more subtle, but related observation is that the CMCs not only deviate from theory but also deviate from the log*CMC* vs n_c trend observed for conventional nonionic surfactants. In fact, the data suggest that the gemini surfactant CMCs "level off" at some limiting value, although there is not enough data to support this observation conclusively. It can be seen though that the CMCs deviate more from the theoretical prediction as n_c is increased, meeting the conventional CMC data at about $n_c = 18$.

These observations of CMCs deviating from linearity on the log*CMC* plot are not entirely new, even for conventional surfactants. For example, alkyltrimethylammonium bromide surfactants (i.e. $C_nH_{n+1}N(CH_3)_3Br$) has a slight deviation from log*CMC* vs n_c at ~ C_{18}.[5] An even more pronounced effect has been observed for the gemini surfactant analogues of the alkyltrimethylammonium bromide surfactants. Zana *et al.*[20] studying gemini surfactants with a six methylene spacer at 25 ºC and $n_c = 8$, 12 and 16 found no deviation from linearity. However, Menger *et al.*[22] studying gemini surfactants at 50 ºC with $n_c = 12$, 14, 16 and 18 and with a four methylene spacer found a deviation at $n_c = 18$, where the CMC for $n_c = 18$ is approximately the same as for $n_c = 16$.

In previous work, Menger *et al.*[2] studying a range of cationic gemini surfactants with $n_c = 8$ to 20 and a range of hydrophobic spacers found the CMC for $n_c = 18$ was *larger* than the CMC for $n_c = 16$. He treats these results with caution due to problems with slow equilibration, however the trend appears real. Song and Rosen[30] studying surfactants with the same spacer in 0.01 or 0.1 M NaCl, found deviation at $n_c = 14$ in both solutions. No increase in the CMC was observed with n_c though. Rosen and Lui[21] studying a gemini surfactant at 25 ºC with a spacer of $CH_2CH(OH)CH(OH)CH_2$

in both water and 0.1M NaBr found deviation at $n_c = 16$ (for the water solution) and at $n_c = 14$ (for the NaBr solution).

In short, a considerable number of gemini surfactants deviate from the normally observed relationship of ln*CMC* vs n_c. There is little correlation between the value of n_c at deviation and the type of spacer (be it rigid or flexible, hydrophobic or hydrophilic). Thus the source of deviation appears to be intrinsic to the behaviour of gemini surfactants and not due to the chemical nature of the spacer. To explore this further it is necessary to break down ΔG^{o}_{mic} and consider each component of micelle formation separately. Many have suggested the following:[6,54]

$$\Delta G^{o}_{mic} = \Delta g_{hp} + \Delta g_{hg} + \Delta g_{it} \qquad 4.1$$

where Δg_{hp} is the hydrophobic term, Δg_{hg} is the head group repulsion term and Δg_{it} is the interfacial tension term, each of which will be discussed below.

The hydrophobic term Δg_{hp} is the free energy gained by taking a surfactant tail out of solution and placing it in the hydrocarbon core of a micelle. This is the driving force for micelle formation and is by far the largest contributor to ΔG^{o}_{mic}. An estimate of Δg_{hp} has been made by McAuliffe[100] based on the energy required to transfer n-alkanes from aqueous solution to hexane. For linear hydrocarbons the magnitude of Δg_{hp} increases linearly with n_c. If Δg_{hp} for n-alkanes is plotted against n_c then the slope is the energy required to transfer a methylene group (CH_2) from solution to a purely hydrocarbon environment and the intercept is the additional energy to transfer the two terminal CH_3 groups:[6,100]

$$\Delta g_{hp} = -(3.70 \pm 0.05) n_{CH_2} - (8.8 \pm 0.2) n_{CH_3} \qquad 4.2$$

where all units are in kJ.mol^{-1}. The actual value of Δg_{hp} for surfactant systems will be smaller for several reasons. The two most important are, firstly the hydrocarbon tail is transferred to a confined environment where one end of the tail is anchored to the surface of the micelle. Secondly the CH_2 closest to the micelle surface, and possibly the next CH_2 also, is not sufficiently removed from solution to contribute to Δg_{hp}. Figure 4.8 shows ΔG^{o}_{mic} and Δg_{hp} versus n_c for the conventional C_nE_6 nonionic surfactant series. Clearly Δg_{hp} is the largest contributor to ΔG^{o}_{mic}. The slope for the

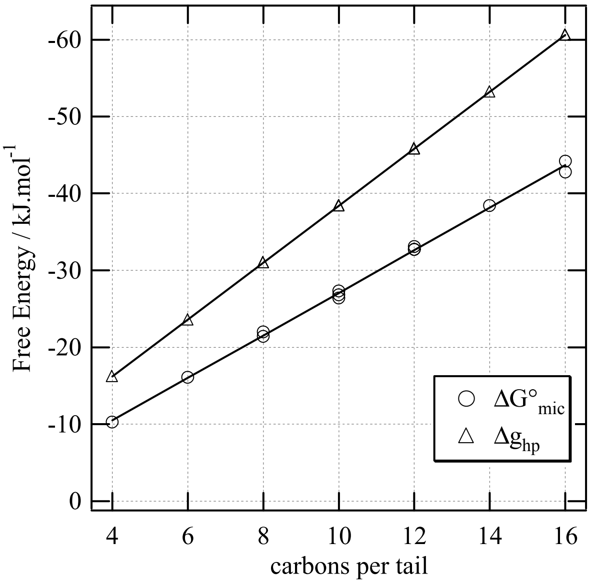

Figure 4.8: Free energy versus carbon atoms per tail for conventional nonionic C_nE_6 series.[70]

nonionic surfactants is 2.8 kJ.mol^{-1} compared with 3.7 kJ.mol^{-1} for n-alkanes. The difference is due to the Δg_{hg} and Δg_{it} terms discussed below.

The head group repulsion term Δg_{hg} is due to the repulsion between surfactant head groups in a micelle. This repulsion opposes the close approach of two surfactant molecules and thus opposes micelle formation. The larger its value the greater the opposition to micelle formation. For ionic surfactants Δg_{hg} is large due to the strong electrostatic interactions between charged head groups. For nonionic surfactants Δg_{hg} is small since it is due to a weak steric interaction between the poly(ethylene oxide) head groups. This difference in Δg_{hg} between ionic and nonionic surfactants is evidenced by the much smaller CMCs of nonionic surfactants compared with ionic surfactants.

The size of Δg_{hg} is dependent on the effective area that each surfactant molecule occupies at the micelle/solution interface (i.e. a_o). There is no exact theoretical value for Δg_{hg} although Israelachvili *et al.*[54] have suggested an inverse area dependence for ionic micelles, which should also be valid for nonionic surfactants.[71] For the conventional C_nE_6 series of surfactants a_o should be roughly constant (since n_{EO} is constant) and thus the value of Δg_{hg} is also expected to be roughly constant.

Finally the interfacial tension term Δg_{it} is an energy cost due to the core of a micelle being in contact with the solution around the micelle. This arises because the *physical* size of a surfactant head group at the micelle/solution interface (a) is smaller than a_o. This additional area ($a_o - a$) is mainly hydrocarbon in direct contact with the solution. The magnitude of Δg_{it} has been estimated by many researchers by multiplying an interfacial tension term by the area of hydrocarbon in contact with solution (i.e. $\gamma(a_o - a)$ the exact value of γ depends on where the area is measured from – Tanford[6] chose the van der Waals radius while Israelachvili *et al.*[54] chose the Gibbs dividing surface). For the C_nE_6 series of surfactants both a and a_o are fairly constant for the same reason given in the last paragraph. Thus the value of Δg_{it} will not change significantly with increasing n_c.

The value of the head group term and the interfacial tension term (i.e. $\Delta g_{\mathrm{hg}} + \Delta g_{\mathrm{it}}$) is the difference in the two lines plotted in Figure 4.8. They produce only a slight increase in magnitude with increasing n_c. Therefore it is clearly Δg_{hp} that produces the strong free energy dependence on n_c and hence the strong CMC dependence on n_c.

Returning to why the gemini surfactant CMCs are larger than expected and why they deviate from the ln*CMC* vs n_c relationship, the two terms Δg_{hg} and Δg_{it} can not be responsible because they are too small and not dependent on n_c. Further more they are dependent on the value of a_o but require it to change more than is physically possible for micelles. Since Δg_{hp} produces the ln*CMC* vs n_c dependence and since it is the driving force of micelle formation, only it can produce a large enough change in $\Delta G^{\mathrm{o}}_{\mathrm{mic}}$ to produce the lower than expected CMCs. Recalling that Δg_{hp} is the energy difference between a surfactant tail in a micelle core surrounded by hydrocarbon and a surfactant tail in solution surrounded by water molecules, one of these must be different in the gemini surfactant system.

Based on melting point data for n-alkanes Tanford has suggested that for surfactants with tails greater than C_{16} the core of the micelle is no longer liquid-like.[6] To transfer a hydrocarbon to this environment will thus produce a loss of freedom in movement and Δg_{hp} will be reduced from the value given by Equation 4.2. This may contribute to the higher than expected CMCs of the $\mathrm{Gem}_{20}\mathrm{E}_m$ series of surfactants but is insufficient for the $\mathrm{Gem}_{12}\mathrm{E}_m$ and the $\mathrm{Gem}_{14}\mathrm{E}_m$ series.

This leaves the energy of surfactant tails in solution. At this point it should be noted that the value of Δg_{hp} per CH_2 and CH_3 in Equation 4.2 for linear hydrocarbons is not observed for branched and cyclic hydrocarbons. In fact calculations based on experimental data suggest that Δg_{hp} is most probably related to the number of water molecules in contact with the hydrocarbon or the area of the cavity the molecule occupies in solution.[6,101,102] If the area of contact between the water molecules and the surfactant tail can be reduced then the value of Δg_{hp} will also be reduced. Some have even suggested this occurs for conventional surfactants.[103] It has been postulated that surfactants form dimers in solution such that two tails interact with each other reducing the area of contact with the solution.[103] This is only postulated for very hydrophobic surfactants, which is the case for gemini surfactants that have two tails tethered together. The possibility also exists that since the tails are tethered together they also interact with each other to produce the same decrease in the magnitude of Δg_{hp}. Menger has attempted to distinguish between these two theories by synthesising cationic gemini surfactants with a long rigid spacer so that the tails can not interact and then observing if they deviate from the $\ln CMC$ vs n_c relation.[2] This study suggested that the trend is caused by dimer formation below the CMC, although results were hampered due to equilibration problems when measuring the CMCs.

Zana[104] has studied dimer formation of cationic gemini surfactants (Figure 2.1) using electrical conductivity measurements. He found premicellar aggregation is present for C_{12} alkyl tails when the spacer is greater than 12 methylenes and present for C_{14} alkyl tails for eight methylene spacers. Based on these results the most probable reason for the nonionic gemini CMCs being higher than expected is dimer formation.

Chapter 5: Micelle Morphologies

5.1 Introduction

Having dealt in the last chapter with the concentration that micelles first form (the CMC) we now turn to the morphology of micelles in solution. Specifically, this chapter is concerned with the shapes the gemini surfactant micelles form (i.e. are they spherical, rod-like or disks?) and how they compare to conventional nonionic surfactant behaviour. The micelle morphology was studied as a function of the following:

1. The surfactant ethoxylation number and tail length,
2. The concentration of surfactant in solution and
3. The temperature.

Firstly, increasing the ethoxylation number increases the area per surfactant head group. The effect of this on micelle morphology was rationalised previously using the packing parameter,[54] $v/a_o l_c$. In particular, surfactants with low a_o values have large packing parameter values and thus prefer to form less curved structures, such as bilayers and rod-like micelles. Surfactants with larger a_o values have smaller packing parameter values and thus prefer to form micelles with high curvature, such as spherical or short rod-like micelles. Thus, as the size of the head group is increased with increasing ethoxylation number the micelle morphology is expected to follow the order of planar → rod-like → spherical.

Secondly, we are interested in how the micelle morphology is altered as the surfactant concentration is increased. As the concentration is increased a_o tends to become smaller and the transition of spheres → rods → bilayers is expected. As the concentration is increased further, a more noticeable effect is the reduced volume available for micelles, which leads to micelle interactions becoming significant at concentrations of a few weight percent.

Finally, interesting behaviour has been observed for conventional nonionic surfactants as the temperature is increased, especially in the region leading up to the cloud point.[105-107] Thus the gemini surfactants with accessible cloud points were studied as a function of temperature. To date the exact nature of micelle behaviour in this region has not been fully explained but it is widely believed that as the cloud temperature is approached the polyoxyethylene head groups begin to dehydrate,[71] which decreases the area they occupy (Figure 2.8). This leads to a sphere → rod transition and some have proposed a rod → branched rod transition at the cloud temperature.[108,109]

5.1.1 Methods of Study

5.1.1.1 Small Angle Neutron Scattering

The primary method for the determination of micelle morphology is Small Angle Neutron Scattering (SANS) as described in the experimental chapter. The experimental methodology is:

1. Raw scattering data is collected on a two dimensional detector, then radially averaged and calibrated to yield absolute scattering intensity versus scattering vector ($I(Q)$ vs Q),
2. The reduced data is analysed by a series of model-independent scattering theories to determine the approximate dimensions of the micelles,
3. The data is fit with analytical scattering models based on the expected micelle morphologies and interactions between them. The most common morphologies are spheres, ellipsoids (both prolate and oblate) and rods. For nonionic surfactants core-shell morphologies are used,[105-107] where the core is the hydrocarbon core of the micelle and the shell consists of hydrated ethylene oxide head groups.

5.1.1.2 Limitations of SANS

SANS (as beautiful a technique as it is) possesses some minor limitations. These are covered throughout the experimental chapter but the three main limitations that should be borne in mind throughout this chapter are:

1. The limit of resolution is of the order of micelle sizes. The smallest structure that can be resolved with SANS is approximately $2\pi/Q$.[83] We used a Q range of ~0.004 to 0.4 Å^{-1}, corresponding to a length scale of ~15 to 1500 Å. At the lower limit of detection micelle diameters are of the order of 30–50 Å, which is well inside the resolution of the SANS instrument. At the upper limit of detection micelles with elongated structure cannot be resolved if they extend more that 1500 Å.
2. Interacting particles complicate the SANS data and in many cases cannot be accounted for theoretically. Several analytical functions exist to account for interactions between spherical micelles[83] and these may also be applied to slightly ellipsoidal micelles, however, there are currently no analytical functions for fitting interactions between highly anisotropic micelles.
3. SANS data is averaged over all micelle orientations, which can lead to ambiguity in interpretation of data. One of the most noted cases is differentiation between polydisperse and elliptical micelles.[87] This ambiguity arrises because the size averaged scattering of polydisperse micelles is very similar to the orientationally averaged scattering of elliptical micelles.

These three limitations sometimes create ambiguity in the interpretation of data. In most of these cases it is of little consequence, such as if a micelle is slightly polydisperse or slightly elliptical. Occasionally though, two different models can fit the same data.[110] In these cases other experimental techniques are required to distinguish between the conflicting models. In this chapter viscosity data is used to distinguish between elongated micelles and short clustered micelles.

5.1.2 Surfactants Studied

The surfactants *available* for study are $Gem_{12}E_5$, E_{10} & E_{15}, $Gem_{14}E_5$, E_{10} & E_{15} and $Gem_{20}E_{10}$, E_{15}, E_{20} & E_{30} although the surfactants with the smallest ethoxylation

carbon atoms per tail	Ethoxylation number				
	5	10	15	20	30
12[*]	†	59	> 100	—	—
14[*]	†	46	> 100	—	—
20	—	†	81	> 100	> 100

Table 5.1: 1 wt% cloud temperatures (in °C) for Gem$_{12}$E$_{5-15}$, Gem$_{14}$E$_{5-15}$ and Gem$_{20}$E$_{10-30}$ in D$_2$O.

†Gem$_{12}$E$_5$, Gem$_{14}$E$_5$ and Gem$_{20}$E$_{10}$ are insoluble at room temperature, hence the cloud points could not be determined (see Chapter 6).

Carbon atoms per tail	Ethoxylation number			
	10	15	20	30
12	1 wt% 20 to 48 °C	1 wt% 25 °C	—	—
14	1 wt% 20 to 39 °C	1 wt% 25 °C	—	—
20	—	1, 2, 5 & 10 wt% 20 to 76 °C	1, 5 & 10 wt% 25 °C	1, 5 & 10 wt% 25 °C

Table 5.2: Concentrations and temperatures of samples used in SANS studies. All surfactants were initially studied at 1 wt% at 25°C. The three surfactants with accessible cloud temperatures (Gem$_{12}$E$_{10}$, Gem$_{14}$E$_{10}$ and Gem$_{20}$E$_{15}$, see Table 5.1) were studied from 20 °C up to their cloud temperature.

---

[*] SANS data for the Gem$_{12}$E$_m$ and Gem$_{14}$E$_m$ series was collected in collaboration with Dr Tim Davey of Dulux but analysis and interpretation was conducted separately.

number in each series were not studied due to their low solubility (see Table 5.1). The main focus was on the $Gem_{20}E_m$ surfactants, but the shorter tailed surfactants provide a good comparison for determining general trends with changing surfactant structure.

We consider first 1 wt% samples at 25 °C. At 1 wt% the samples are sufficiently dilute that micelle interactions are minimised and the scattering is due to independent scattering micelles. Next interactions between micelles were examined by studying $Gem_{20}E_{15}$, $Gem_{20}E_{20}$ and $Gem_{20}E_{30}$ at 2 wt% ($Gem_{20}E_{15}$ only), 5 wt% and 10 wt%. Finally, 1 wt% solutions of $Gem_{12}E_{10}$, $Gem_{14}E_{10}$ and $Gem_{20}E_{15}$ (which all have accessible cloud points) were studied as a function of temperature to determine structural changes as the cloud point is approached. A summary of surfactant compositions and temperatures studied is given in Table 5.2.

5.2 Results

5.2.1 Gemini Surfactants at 1 wt% and 25 °C

log*I(Q)* vs log*Q* for the gemini surfactants at 1wt% and 25°C are presented in Figure 5.1a-c. Before specific models are applied to fit the SANS data it is instructive to consider the scattering in light of ideal scattering behaviour. Ideal behaviour typically assumes one or more of the following:

1. the particles do not interact
2. the particles are monodisperse and
3. the particles have a single uniform scattering length density.

The first assumption allows the total scattering to be considered as simply the scattering from a single particle multiplied by the number of particles in solution. This is the same assumption used to derive the scattering models in Section 3.2.2, (Equation 3.2 – 3.3). The second and third assumptions allow the system to be described by a single particle geometry and greatly simplify calculations.

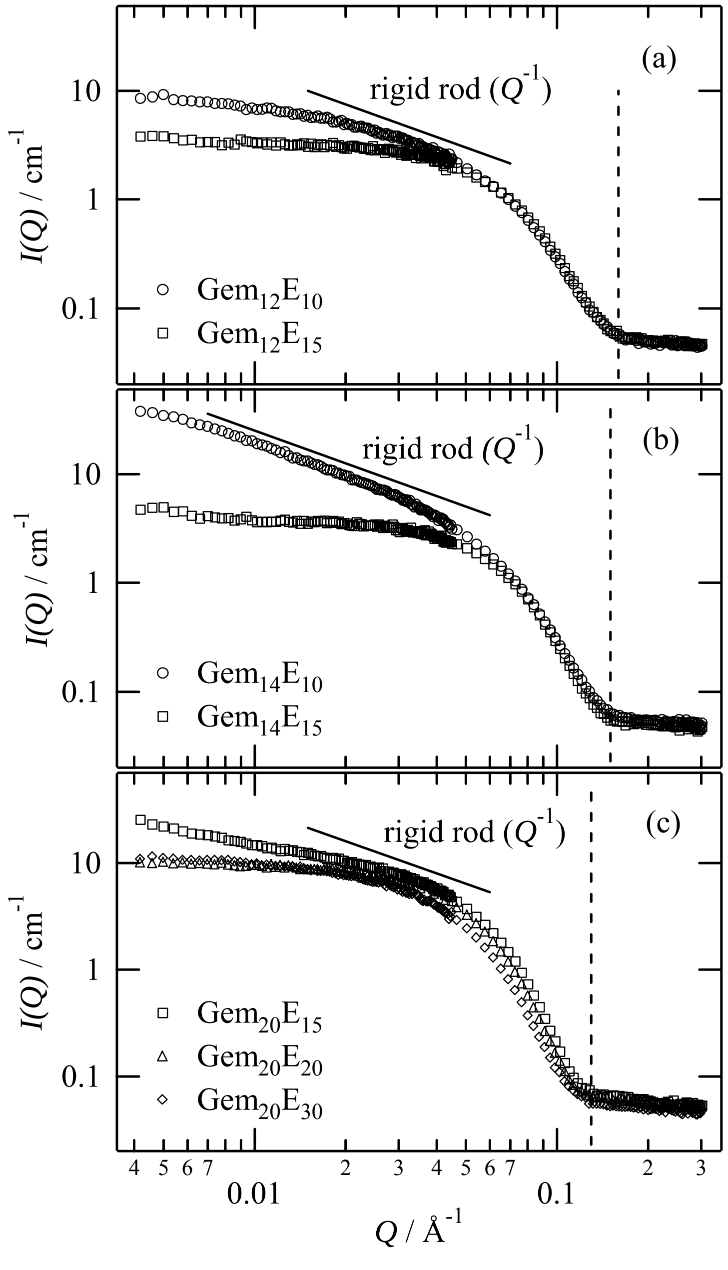

Figure 5.1: SANS data for 1 wt% solutions of a) $Gem_{12}E_m$, b) $Gem_{14}E_m$ and c) $Gem_{20}E_m$ at 25°C in D_2O. The dashed line is the scattering minimum, which corresponds to the smallest micellar dimension and the Q^{-1} is the scattering expected for long, rigid rod-like micelles.[111]

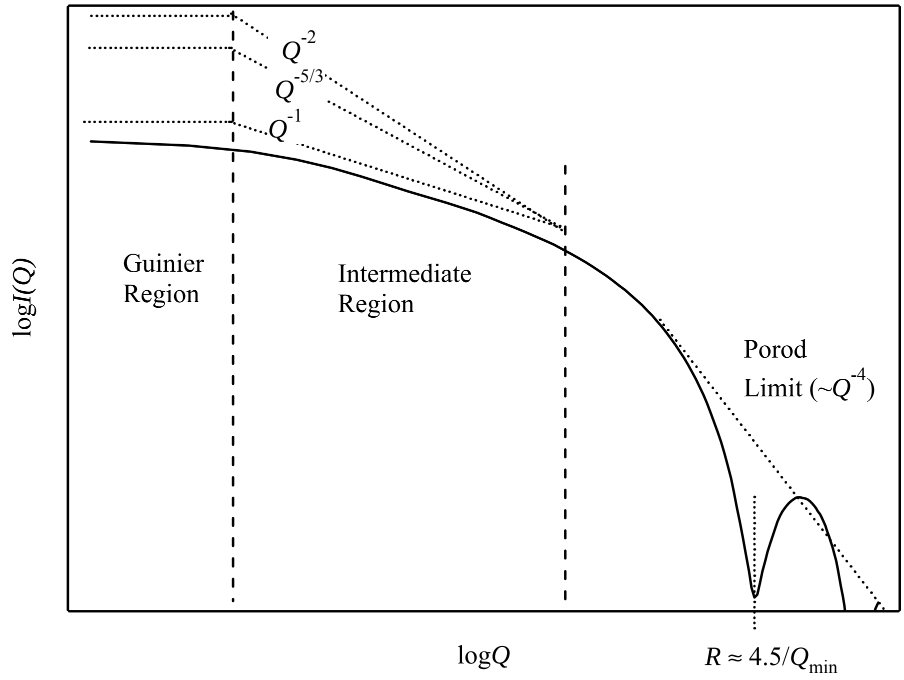

Figure 5.2: Schematic representation of the scattering regions for typical SANS data on a log-log plot. The data can be divided into several regions, from high to low Q there is: the Porod limit, which scatters as ~Q^{-4}, then the first "minimum" at $Q \approx 4.5/R$. Next is the intermediate region, which scatters as ~Q^{-1} for rigid rods, ~$Q^{-5/3}$ for an excluded volume coil, ~Q^{-2} for a gaussian coil and ~Q^{-2} for platelets.[111,112] Finally, the Guinier region extends to very low Q, which in the absence of micelle-micelle interactions levels off on a log-log scale.

The application of ideal scattering behaviour is not strictly valid for the nonionic gemini micelles because they are core-shell particles (i.e. the hydrocarbon core has a different scattering length density to the polyethylene oxide shell). Regardless of this, the following general scattering laws allow a qualitative description of the scattering curves.

The scattering curves may be divided into several regimes, shown schematically in Figure 5.2. Each of these regions will be considered in turn below.

The Scattering Minimum, marked with dashed lines in Figure 5.1a-c, is related to the smallest length scale of the micelles. For monodisperse spheres this corresponds to the first scattering minimum and is smeared in this data because the micelles are either slightly polydisperse or slightly elliptical (cf. Figure 3.7). For the ideal case of noninteracting, homogenous, monodisperse spheres the scattering function is:

$$I(Q) = \frac{N_P}{V_{tot}} \left[\frac{3V_{micelle}\Delta\rho(\sin QR - QR\cos QR)}{(QR)^3} \right]^2 \qquad 3.5$$

where N_P is the number of micelles, V_{tot} is the volume of the solution, V_{micelle} is the volume of a single micelle, $\Delta\rho$ is the difference between the scattering length density of the micelle and the solvent and R is the radius of the micelle. The scattering function has its first zero at $QR \approx 4.5$, i.e. $R \approx 4.5/Q_{\text{min}}$. Thus, this relationship gives the radius of spheres. If the micelles are not spherical this relationship provides an *estimate of the smallest micellar dimension.* For example, for rod-like micelles it turns out $R_{\text{rod}} \approx 3.9/Q_{\text{min}}$, where R_{rod} (the cross-sectional radius) is only 83% smaller than for a sphere.

$R \approx 4.5/Q_{\text{min}}$ values are given in Table 5.3 and are approximately 26 Å for the $\text{Gem}_{12}\text{E}_{\text{m}}$ series, 30 Å for the $\text{Gem}_{14}\text{E}_{\text{m}}$ series and 38 Å for the $\text{Gem}_{20}\text{E}_{\text{m}}$ series. That is, the micelle radius becomes larger as the hydrocarbon tail is increased in length. This trend is seen in Figure 5.1a-c as the scattering minimum moves towards lower Q as m increases, which in real space equates to a larger radius. This trend: that the micelle radius increases with alkyl tail length, is expected.

Further, for each surfactants series with the same tail length, the scattering minima almost overlap, indicating that the smallest micelle dimension changes little with increasing ethoxylation number. This shows that increasing the ethoxylation number has little effect on the size of the micelle radius. However, it will be seen later that it has a large effect on the shape of the micelle.

Because the micelles are core-shell, the above values are not exact. For core-shell micelles the minimum is due to a combination of scattering from the core and the shell. The relationship between $R \approx 4.5/Q_{\text{min}}$ and the actual micelle radius depends on the scattering length density of the shell (ρ_{shell}), the core (ρ_{core}) and the solvent (ρ_{solv}) as well as the thickness of the shell relative to the radius of the core. For nonionic surfactants the value of ρ_{shell} lies between ρ_{core} and ρ_{solv}, as discussed in Section 3.2.2. For pure polyethylene oxide, ρ_{shell} is 0.64 x 10^{-6} Å^{-2}, which is much closer to the value of ρ_{core} (-0.29 x 10^{-6} Å^{-2}) than ρ_{solv} (6.4 x 10^{-6} Å^{-2}). For this unlikely case of “dry” head groups, $R \approx 4.5/Q_{\text{min}}$ equals the micelle radius to within 0.5%. With hydration of

Surfactant	$R_{\text{sphere}} \approx \frac{4.5}{Q_{\min}}$ (Å)	R_G (Å)	$\langle l \rangle$ (Å)	$R_{\text{sphere}} = \sqrt{\frac{5}{3}}R_G$ (Å)	$R_{\text{sphere}} = \frac{2\langle l \rangle}{3}$ (Å)
Gem$_{12}$E$_{10}$	26	69 ± 5	61 ± 3	89 ± 7	41 ± 2
Gem$_{12}$E$_{15}$	26	27 ± 3	54 ± 3	35 ± 4	36 ± 2
Gem$_{14}$E$_{10}$	30	208 ± 20	74 ± 3	270 ± 26	49 ± 2
Gem$_{14}$E$_{15}$	30	26 ± 6	57 ± 3	34 ± 8	38 ± 2
Gem$_{20}$E$_{15}$	38	80 ± 50	73 ± 3	103 ± 65	49 ± 2
Gem$_{20}$E$_{20}$	38	38 ± 3	71 ± 3	49 ± 4	48 ± 2
Gem$_{20}$E$_{30}$	38	54 ± 5	75 ± 4	70 ± 7	51 ± 2

Table 5.3: Comparison of $R \approx 4.5/Q_{\min}$, the radius of gyration, and the mean chord length, $\langle l \rangle$. Columns 4 and 5 are the radius of a sphere with R_G and $\langle l \rangle$ values from columns 2 and 3. Comparison shows good agreement for Gem$_{12}$E$_{15}$, Gem$_{14}$E$_{15}$ and Gem$_{20}$E$_{20}$ indicating spherical micelles. Poor agreement is obtained for Gem$_{12}$E$_{10}$, Gem$_{14}$E$_{10}$ and Gem$_{20}$E$_{15}$ indicating elongated structure.

the head groups ρ_{shell} approaches ρ_{solv}, effectively making the shell "invisible" to neutrons. Thus, $R \approx 4.5/Q_{\min}$ approaches the radius of the core and becomes a poorer estimate of the true micelle radius.

The actual value of ρ_{shell} lies between these two extremes and $R \approx 4.5/Q_{\min}$ is between the radius of the core and the total micelle radius. If the head group is assumed to contain two D_2Os per ethylene oxide,[106] ρ_{shell} equals 3.4 x 10^{-6} Å^{-2} and the maximum difference between $R \approx 4.5/Q_{\min}$ and the actual micelle radius is ~20%. The difference depends strongly on the ratio of shell-thickness to core-radius, with the maximum difference when the two values are approximately the same (see Appendix A5).

Consider now the *low Q regime*, where $Q < 1/R$ (Figure 5.2) and R is the smallest dimension of the micelles. This region contains structural information on length scales greater than R. That is, it contains information about either elongation of micelles (spheres, rods or plates) or micelle-micelle interactions (both attractive or repulsive).

Assuming no interactions between micelles, the low Q region is further divided into the intermediate and the Guinier region. The intermediate region spans the approximate range of $1/L < Q < 1/R$ (Figure 5.2), where L is the largest linear dimension of a micelle. The Guinier region begins in the intermediate region and extends to zero Q.

The intermediate region provides a rapid means of distinguishing between spherical, rod-like and planar aggregates. Spheres have no extended structure because their largest dimension is their radius, thus they have no intermediate region and at low Q on a log-log plot their scattering approaches a constant. This behaviour is observed for $\mathrm{Gem_{12}E_{15}}$, $\mathrm{Gem_{14}E_{15}}$ and $\mathrm{Gem_{20}E_{20}}$ and $\mathrm{Gem_{20}E_{30}}$ (Figure 5.1) showing that these surfactants are spherical or near spherical. Further, the levelling off at very low Q suggests that there are little or no micelle interactions (except possibly for $\mathrm{Gem_{20}E_{30}}$).

The intermediate region for rod-like micelles is slightly more complicated because of the several forms that rod-like micelles can assume. For example, rigid rods scatter as Q^{-1}, excluded volume coils as $Q^{-5/3}$ and Gaussian coils as Q^{-2}.[111,112] On log-log plots these power laws appear linear with slopes corresponding to the exponent as shown schematically in Figure 5.2. Only Q^{-1} behaviour approximates the experimental scattering and is also shown in Figure 5.1a-c.

$\mathrm{Gem_{14}E_{10}}$ scatters as Q^{-1}, almost to the lower limit of Q strongly suggesting long, rigid, rod-like micelles.[111] $\mathrm{Gem_{12}E_{10}}$ almost scatters as Q^{-1} for a limited Q range possibly suggesting short, rod-like micelles. However, at lower Q the data does not level off as expected for short, rigid rods but continues to increase slowly. Finally, $\mathrm{Gem_{20}E_{15}}$ clearly shows increasing scattering with decreasing Q, but has a slope lower than Q^{-1}. The structure is obviously more complex than simple rigid, rod-like micelles but the scattering indicates extended structures.

From SANS it is possible to measure a single length parameter called the radius of gyration (R_G), defined as:[84]

$$R_G^2 = \frac{\int_0^{\infty} r^2 d\rho(r)}{\int_0^{\infty} d\rho(r)} \qquad 5.1$$

where r is the distance from the centre of mass (or the scattering equivalent) and ρ is the scattering length density at *r* relative to the solvent (the Δ has been dropped to simplify the notation). R_G, as defined by this equation, is valid irrespective of micelle geometry or scattering length density distribution. The physical interpretation of R_G will be considered later.

The radius of gyration is measured experimentally in the Guinier region by either the Guinier approximation (best for spheres and cylinders with a large radius) or the Zimm approximation (best for polymers and rigid rods).[112] The Guinier approximation is:[84]

$$I(Q) = N_P^2 \Delta\rho \exp\left(-\frac{Q^2 R_G^2}{3} \right) \qquad 5.2$$

and the Zimm approximation is:[113]

$$I(Q) = N_P^2 \Delta\rho \left(1 + \frac{Q^2 R_G^2}{3} \right)^{-1} \qquad 5.3$$

These approximations are only valid for $QR_G < 1$.[83,84]

The Guinier approximation was used to measure R_G for $Gem_{12}E_{15}$, $Gem_{14}E_{15}$, $Gem_{20}E_{20}$ and $Gem_{20}E_{30}$, since these are most likely spherical structures as determined from the lack of an intermediate region. R_G was obtained by taking the slope of ln*I(Q)* vs Q^2, which from Equation 5.2 is equal to $-R_G^2/3$. An example is given in Figure 5.3a for $Gem_{14}E_{15}$, the other plots are given in Appendix A8.

The Zimm approximation was used for $Gem_{12}E_{10}$, $Gem_{14}E_{10}$ and $Gem_{20}E_{15}$ because they show extended structure in the intermediate region. R_G was obtained by plotting 1/*I(Q)* vs Q^2 and dividing the slope by the intercept, which by rearranging Equation 5.3 is equal to $R_G^3/3$. An example is given in Figure 5.3b for $Gem_{14}E_{10}$, the other plots are also given in Appendix A8.

All R_G values are given in Table 5.3. For $Gem_{12}E_m$ R_G dramatically *decreases* from 69 Å to 27 Å as *m* is *increased* from 10 to 15. This same trend is observed for the slightly longer tailed $Gem_{14}E_m$ surfactants, where R_G *decreases* from 208 Å to 26 Å as *m* is again *increased* from 10 to 15. For $Gem_{20}E_m$ R_G decreases from 80 Å to 38 Å for E_{15} to E_{20}, but then increases to 54 Å for E_{30}. This is consistent with rods for E_{15}, spheres for E_{20} and larger spheres for E_{30}.

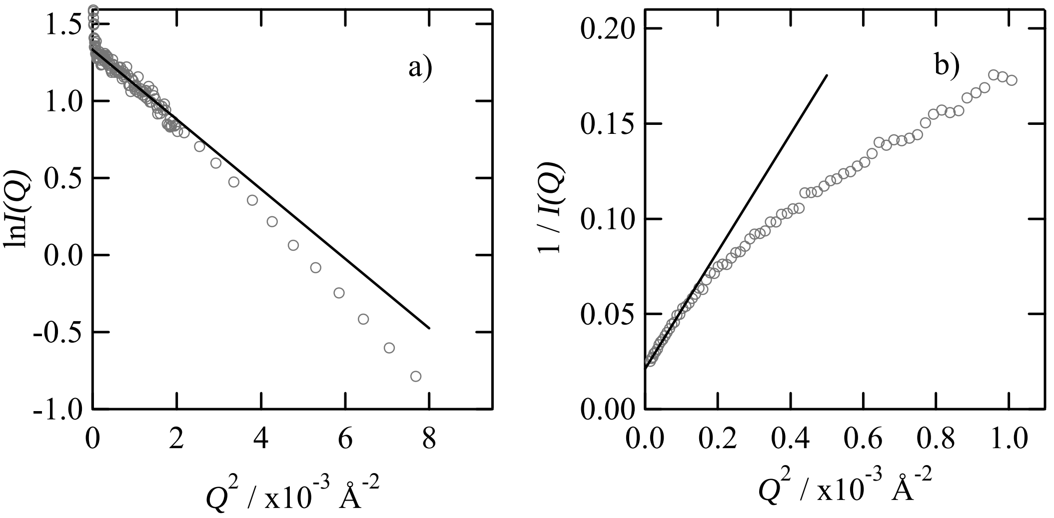

Figure 5.3: a) Guinier plot for Gem$_{14}$E$_{15}$, from Equation 5.2 the slope is equal to $-R_G^2/3$. b) Zimm plot for Gem$_{14}$E$_{10}$, from Equation 5.3 the slope/intercept is equal to $R_G^2/3$. The slope and intercept are measured at $QR_G < 1$. Plots for the other surfactants are given in Appendix A8.

R_G is very large for the E$_{10}$ surfactants due to their extended structure. The E$_{15}$ surfactants show no change for Gem$_{12}$E$_{15}$ and Gem$_{14}$E$_{15}$ but increase noticeably for Gem$_{20}$E$_{15}$ (despite the large error for Gem$_{20}$E$_{15}$, see Appendix A8).

Physical meaning can be given to R_G by applying specific geometric models. Using a single scattering length density, for consistency with earlier models, spheres give:[86]

$$R_G = \sqrt{3/5}\,R_{\text{sphere}} \qquad 5.4$$

where R_{sphere} is the radius of the sphere. Comparison of this to a core-shell micelle gives a maximum difference of only 7% for two D_2O/EO in the shell (see Appendix A6).

For rigid cylinders:[84]

$$R_G = \sqrt{\frac{L^2}{12} + \frac{R_{\text{rod}}^2}{2}} \qquad 5.5$$

where L is the length of the cylinder and R_{rod} is the cross-sectional radius. If $R_{\text{rod}} \approx L$ then R_{rod} dominates the R_G value. If L is much larger than R_{rod} ($L \geq {\sim}5R_{\text{rod}}$) it will dominate due to the square dependence in Equation 5.5, and $L \approx \sqrt{12}R_G$. Thus, R_G is approximately proportional to R_{rod} for small rods and approximately proportional to L for long rods.

Because R_G is sensitive to the length of micelles and R from Q_{min} is only sensitive to the cross sectional radius, comparison of these two values indicates the approximate elongation of the micelles. Table 5.3 presents $R \approx 4.5/Q_{min}$ in column 1, R_G in column 2 and R_{sphere} in column 4, calculated from R_G using Equation 5.4. For both the $Gem_{12}E_m$ surfactants, R ~26 Å, demonstrating that the smallest radius does not change with ethoxylation number yet R_{sphere} is ~89 Å for $Gem_{12}E_{10}$ and only ~35 Å for $Gem_{12}E_{15}$. This large discrepancy suggests $Gem_{12}E_{10}$ is significantly elongated compared with $Gem_{12}E_{15}$ and is probably *short*, rod-like micelles of some sort.

The same trend is seen for the two $Gem_{14}E_m$ surfactants. R is ~30 Å for both surfactants, while R_{sphere} is 270 Å for $Gem_{14}E_{10}$ and 34 Å for $Gem_{14}E_{15}$. R_{sphere} is much larger than R for $Gem_{14}E_{10}$, suggesting *long* elongated micelles. Assuming rod-like micelles, the approximation $L \approx R_G\sqrt{12}$ gives a length of ~700 Å.

Finally for $Gem_{20}E_m$ R is ~38 Å and $R_{spehere}$ is 80 ± 50 Å, 38 Å and 54 Å for $Gem_{20}E_{15}$, $Gem_{20}E_{20}$ and $Gem_{20}E_{30}$ respectively. R_{sphere} for $Gem_{20}E_{15}$ and $Gem_{20}E_{30}$ are poor due to difficulties in extrapolation, regardless, comparison suggests elongated micelles of some type for $Gem_{20}E_{15}$, spherical micelles for $Gem_{20}E_{20}$ and most probably spherical or slightly elongated micelles for $Gem_{20}E_{30}$.

Comparison of surfactants with the same head groups reveals for E_{10} surfactants that $Gem_{12}E_{10}$ is slightly elongated, while the longer tailed $Gem_{14}E_{10}$ is highly elongated. For the E_{15} surfactants $Gem_{12}E_{10}$ and $Gem_{14}E_{10}$ are spherical, while the longer tailed $Gem_{20}E_{15}$ is probably slightly elongated (although less than either of the E_{10} surfactants). The E_{20} and E_{30} surfactants are both spherical.

5.2.1.1 Chord Analysis

Another useful quantity calculated from scattering data is the mean chord length $\langle l \rangle$,[114] (usually denoted l_c but denoted here as $\langle l \rangle$ to distinguish it from the critical tail length). The mean chord length is another length scale like R_G, but unlike R_G it is insensitive to micelle interactions.[84] For this reason the mean chord length provides a useful comparison to other methods of interpretation, which may be dependent on interactions or particle geometry. The mean chord length is only strictly valid for micelles with a single scattering length density and thus its application to core-shell micelles is only an approximation.

The mean chord length is calculated from scattering data by:[114]

$$\langle l \rangle = \frac{\pi}{q^*}\int_0^\infty QI(Q)dQ$$

where q^* is the invariant defined by:

$$q^* = \int_0^\infty Q^2 I(Q)dQ$$

Integration requires data from the Guinier region at high Q to the Porod limit at low Q. Examples of the two functions for integration are shown in Figure 5.4 for $\mathrm{Gem}_{12}\mathrm{E}_{15}$.

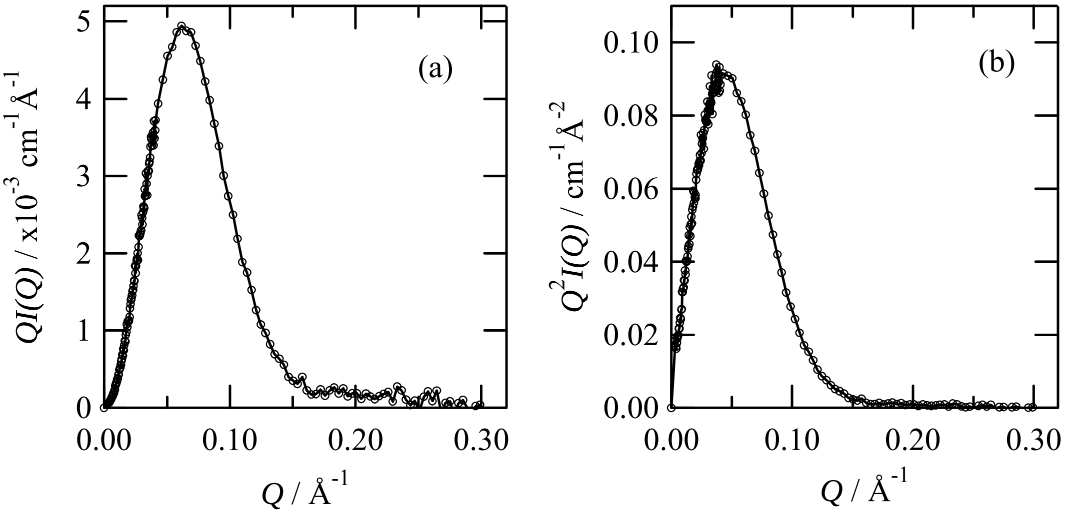

Figure 5.4: Example of the mean chord length ⟨*l*⟩ calculation for $\mathrm{Gem}_{12}\mathrm{E}_{15}$. ⟨*l*⟩ is calculated by integration of (a) *QI(Q)* vs *Q* and then multiplying by π over the integral of b) $Q^2I(Q)$ vs *Q*.[114]

Mean chord values are given in Table 5.3 and show a general *decreases* with *increasing* ethoxylation number. For the $\mathrm{Gem}_{12}\mathrm{E}_m$ series it decreases modestly from 61 Å to 54 Å and for the $\mathrm{Gem}_{14}\mathrm{E}_m$ series decreases more obviously from 74 Å to 57 Å. In contrast the $\mathrm{Gem}_{20}\mathrm{E}_m$ series reveals only slight differences going from 73 Å to 71 Å to 75 Å.

Comparing surfactants with the same ethoxylation number, ⟨*l*⟩ increases for the E_{10} surfactants from 61 Å for $\mathrm{Gem}_{12}\mathrm{E}_{10}$ to 74 Å for $\mathrm{Gem}_{14}\mathrm{E}_{10}$ (i.e. by 13 Å). This increase is much larger than the 2.5 Å increase in micelle radius expected from the addition of two carbons to the alkyl tail (Equation 2.1) and suggests elongated micelles that become more elongated with increased tail length.

The E_{15} surfactants show a much smaller increase of 54 to 57 to 73 Å going from $\mathrm{Gem}_{12}E_{15}$ to $\mathrm{Gem}_{14}E_{15}$ to $\mathrm{Gem}_{20}E_{15}$ and corresponds to increases of ~3 Å for C_{12} to C_{14} and ~16 Å for C_{14} to C_{20}. For spherical micelles these are expected to increase by ~2.5 Å and ~7.3 Å with the addition of two carbons and six carbons respectively (Equation 2.1). This suggests spherical micelles for the first two surfactants and slight elongation for $\mathrm{Gem}_{20}E_{15}$.

Mean chord lengths are given in Table 5.3 for comparison to R_G. Comparison is easier if $\langle l \rangle$ is converted to the radius of an equivalent sphere,[84]

$$R_{\mathrm{sphere}} = \frac{2}{3}\langle l \rangle$$

which is also given in Table 5.3.

For the $\mathrm{Gem}_{12}E_m$ surfactants, R_{sphere} calculated from R_G ($R_{\mathrm{sphere,Rg}}$) and $\langle l \rangle$ ($R_{\mathrm{sphere},\langle l \rangle}$) are in good agreement for $\mathrm{Gem}_{12}E_{15}$ suggesting yet again spherical micelles. For $\mathrm{Gem}_{12}E_{10}$ they are different by a factor of 2.2, which again suggests elongated micelles.

For the $\mathrm{Gem}_{14}E_m$ surfactants $R_{\mathrm{sphere,Rg}}$ and $R_{\mathrm{sphere},\langle l \rangle}$ are in agreement for $\mathrm{Gem}_{14}E_{15}$ suggesting spherical micelles. For $\mathrm{Gem}_{14}E_{10}$ they are different by a factor of 5.5 suggesting highly elongated micelles.

Finally, for the $\mathrm{Gem}_{20}E_m$ surfactants good agreement is obtained for $\mathrm{Gem}_{20}E_{20}$ suggesting spherical micelles, while poor agreement is obtained for $\mathrm{Gem}_{20}E_{15}$ and $\mathrm{Gem}_{20}E_{30}$ also suggesting elongated structures.

5.2.1.2 Model Fitting

Having considered ideal behaviour the data can now be fit with specific models. For simplicity, the models chosen are core-shell morphologies with pure hydrocarbon core and a hydrated polyethylene oxide shell with uniform scattering length densities.

It is more probable though, that the head groups are more hydrated further from the core and that the scattering length density increases continuously from the core to the edge of the micelle. Is it valid then to treat the micelles as core-shell? A linearly changing scattering length density profile for the shell is presented in Figure 5.5a compared with the closest core-shell approximation. Scattering from the linear profile was approximated by a ten-shell model, with the scattering profiles from both models presented in Figure 5.5b. The two curves compare very well with none of the main scattering features significantly altered. Thus, it is justified fitting with core-shell models.

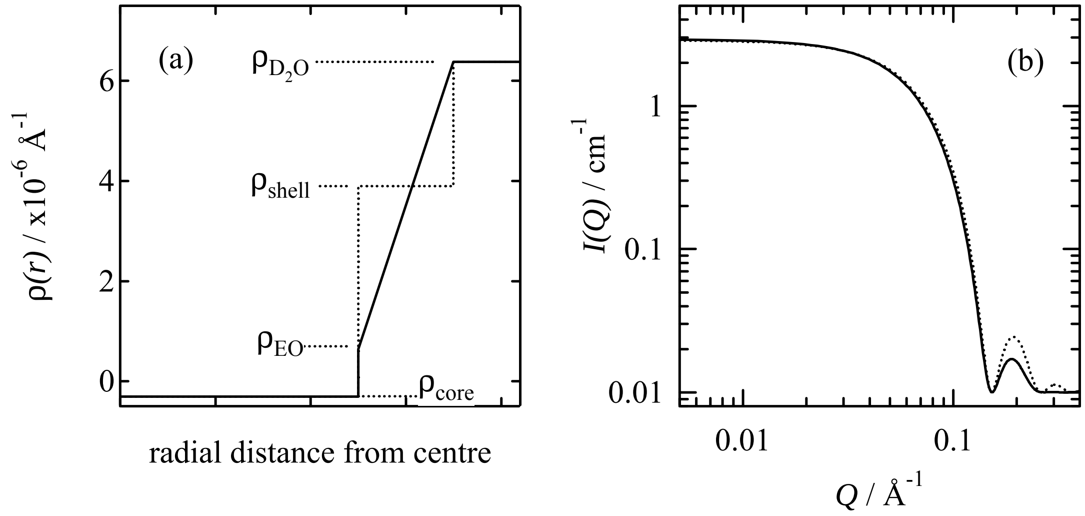

Figure 5.5: a) SLD profile for a core shell particle with a single contrast shell (dotted line) and a continuously varying contrast (solid line). b) the corresponding scattering from the two SLD profiles shows little difference between them.

Only two simple models where used to fit the data, these are core-shell spheres (Equation 3.5) and rigid core-shell rods (Equation 3.6), with neither polydispersity nor resolution smearing being required for reasonable fits. The fitting values for core-shell spheres are the core radius (R_{core}) and the shell thickness (t_{shell}). The fitting values for core-shell rods are the cross-sectional radius of the core (R_{core}), the thickness of the shell (t_{shell}) and the length of the core (L_{core}), where the total length is $L_{\text{core}} + t_{\text{shell}}$.

The other parameters required for fitting are N_P/V_{tot}, ρ_{core}, ρ_{shell}, ρ_{solv} and the background. ρ_{core} and ρ_{solv} were calculated in Section 3.2.2 for pure hydrocarbon and pure D_2O respectively. The background was calculated using the Porod law (see Appendix A7). ρ_{shell} was calculated as a combination of scattering from EO and D_2O (see Section 3.2.2):

$$\rho_{\text{shell}} = \frac{\sum b_{\text{EO}} + n_{\text{D}_2\text{O/EO}} \sum b_{\text{D}_2\text{O}}}{v_{\text{EO}} + n_{\text{D}_2\text{O/EO}} v_{\text{D}_2\text{O}}}$$

where b_{EO} and $b_{\text{D}_2\text{O}}$ are the scattering lengths of a EO unit and a D_2O respectively (see Table 3.2), v_{EO} and $v_{\text{D}_2\text{O}}$ are the volumes of a EO unit and a D_2O molecule respectively (see Table 3.2) and $n_{\text{D}_2\text{O/EO}}$ is the number of D_2Os per EO in the head group (but *not* necessarily the number of D_2Os *associated* with each EO). $n_{\text{D}_2\text{O/EO}}$ was calculated by subtracting the volume of ethylene oxide in the shell from the total shell volume and assuming the remaining volume is D_2O. The equations used are in Appendix A10.

$N_{\text{P}}/V_{\text{tot}}$ was calculated from:

$$\frac{N_{\text{P}}}{V_{\text{tot}}} = \frac{\phi_{\text{vol, HC}}}{V_{\text{core}}}$$

where $\phi_{\text{vol, HC}}$ is the volume fraction of all hydrocarbon cores, calculated directly from the surfactant concentration in wt% using the equations in Appendix A10, and $V_{\text{core}} = \frac{4}{3}\pi R_{\text{core}}^3$ is the volume of the micelle core.

The best fits to the data are shown in Figure 5.6 with the fitting values in Table 5.4. Good fits are obtained for $\text{Gem}_{12}\text{E}_{15}$ (spheres), $\text{Gem}_{14}\text{E}_{10}$ (rods), $\text{Gem}_{14}\text{E}_{15}$ (spheres) and $\text{Gem}_{20}\text{E}_{20}$ (rods). Poor fits are obtained at low Q for $\text{Gem}_{12}\text{E}_{10}$ (rods), $\text{Gem}_{20}\text{E}_{15}$ (spheres) and for $\text{Gem}_{20}\text{E}_{30}$ (spheres), although the high Q data fits very well. Deviation occurs in all cases as increased scattering at low Q, which suggests more complex models are necessary, such as spherical end caps on the micelles, flexibility in the rods, interactions or polydispersity. No attempts where made to generate such complex models due to theoretical limitations, and to avoid over interpretation of the data. The scattering of $\text{Gem}_{12}\text{E}_{10}$ and $\text{Gem}_{20}\text{E}_{15}$ will be returned to later when discussing their temperature dependence. Additional scattering experiments were not conducted to resolve the deviation of $\text{Gem}_{20}\text{E}_{30}$ from spherical micelles.

The shell thickness (Table 5.4) is ~20 ± 2 Å for the E_{10} and E_{15} surfactants. Almost no change is observed, regardless of micelle morphology or tail length. This value is small compared to the all trans lengths of ~40 and ~60 Å for E_{10} and E_{15} respectively, which is consistent with the polyethylene oxide head groups assuming a

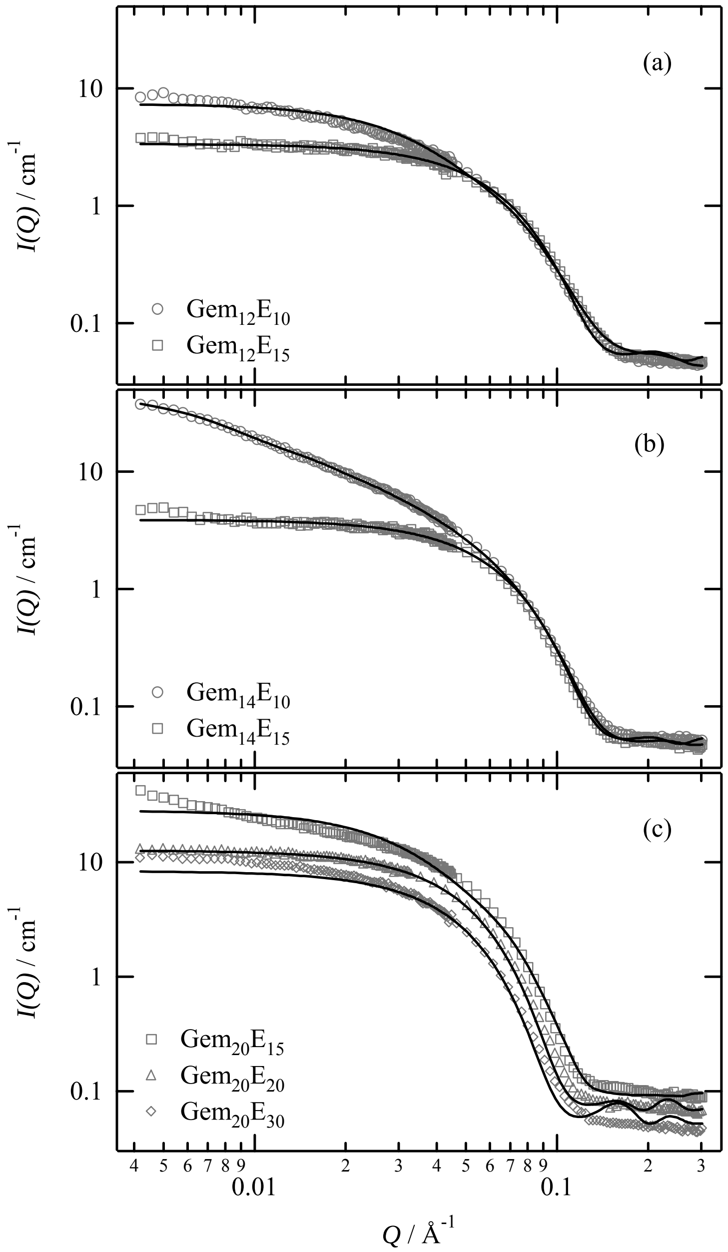

Figure 5.6: Best fits for a) Gem$_{12}$E$_m$, b) Gem$_{14}$E$_m$ and c) Gem$_{20}$E$_m$ at 1 wt% and 25°C. The curves for Gem$_{20}$E$_{15}$ and Gem$_{20}$E$_{20}$ are slightly offset for clarity (cf Figure 5.1). Circles are for E$_{10}$, squares for E$_{15}$, triangles for E$_{20}$ and diamonds for E$_{30}$ surfactants. Best fit values are given in Table 5.4. Good fits are obtained for Gem$_{12}$E$_{15}$ (CS spheres), Gem$_{14}$E$_{10}$ (CS rods), Gem$_{14}$E$_{15}$ (CS spheres) and Gem$_{20}$E$_{20}$ (CS spheres). Poor fits are obtained for Gem$_{12}$E$_{10}$ (CS rods), Gem$_{20}$E$_{15}$ (CS rods) and Gem$_{20}$E$_{30}$ (spheres).

Surfactant	Model	R_{core} (Å)	t_{shell} (Å)	R_{tot} (Å)	L_{core} (Å)	χ^2	ρ_{shell} (x10^{-6} Å^{-2})
Gem$_{12}$E$_{10}$	CS Rod	13	20	33	130	25.4763	4.6
Gem$_{12}$E$_{15}$	CS Sphere	17.8	21.2	39.0	—	1.00064	5.0
Gem$_{14}$E$_{10}$	CS Rod	14.8	18.2	33.0	652.4	5.03747	3.7
Gem$_{14}$E$_{15}$	CS Sphere	19.2	20.5	39.7	—	1.1008	4.9
Gem$_{20}$E$_{15}$	CS Rod	19	18	37	131	317.546	4.1
Gem$_{20}$E$_{20}$	CS Sphere	26.0	26.1	52.1	—	2.78477	5.2
Gem$_{20}$E$_{30}$	CS Sphere	22.8	29.9	52.7	—	135.166	5.6

Table 5.4: Best Fits for 1wt% gemini surfactants at 25°C, where all distances are in Å. Column 1 in the model used, either core-shell spheres (CS Sphere) or core-shell, rigid rods (CS Rod), R_{core} is the core radius, t_{shell} is the shell thickness, R_{tot} is the total radius (R_{core} + t_{shell}), L_{core} is the core length of a core-shell rod (the total length is L_{core} + 2t_{shell}), χ^2 is a goodness of fit parameter (smaller values are better fits) and ρ_{shell} is the scattering length density of the shell. R_{core} increases with tail length, although rod like micelles have smaller values (see text). Little change in the shell thickness is observed except for the Gem$_{20}$E$_m$ surfactants. The length increases greatly going from Gem$_{12}$E$_{15}$ to Gem$_{14}$E$_{15}$ (see text). Fits are shown in Figure 5.6.

more compact meander conformation (Figure 2.2). As the head group is increased to E$_{20}$ and E$_{30}$ small increases of 6 and 10 Å are observed respectively. Larger increases are not observed as the head groups are doubled (from E$_{10}$ to E$_{20}$ and from E$_{15}$ to E$_{30}$) because the polyethylene oxide head groups must occupy more volume as the radius is increased, since volume increases as R^3.

The core-shell sphere radii values (Table 5.4) of 17.8 Å for Gem$_{12}$E$_{15}$, 19.2 Å for Gem$_{14}$E$_{15}$ and ~23 – 26 Å for Gem$_{20}$E$_{20}$ and E$_{30}$ are very close to the l_c values of 16.7 Å, 19.2 Å and 26.8 Å from Equation 2.1.[6] The radius of Gem$_{12}$E$_{15}$ is 1.1 Å larger than l_c and is due to the fitting procedure including some of the shell in the core.

R_{core} for the core-shell rods is smaller than R_{core} for the core-shell spheres, with 13 Å vs 17.8 for Gem$_{12}$E$_m$, 14.8 vs 19.2 Å for Gem$_{14}$E$_m$ and 19 Å vs ~23 – 26 Å for Gem$_{20}$E$_m$. This has been observed for conventional surfactants also[115] and can be understood qualitatively by considering the free energy cost of having ends on rod-like micelles. Israelachvili *et al.*[54] have demonstrated that rod-like micelles form spherical end caps to reduce the free energy cost of hydrocarbon ends in contact with water, as represented in Figure 5.7. Using thermodynamics and geometric arguments they show that the ratio of the area of the rod (a_o) to the area of the end caps (a) lies between 2/3 and 1.[54] From this expression it can be shown that the cross-sectional radius of the rod (R_{rod}) must lie between $2l_c/3$ and l_c, as observed from the SANS results.

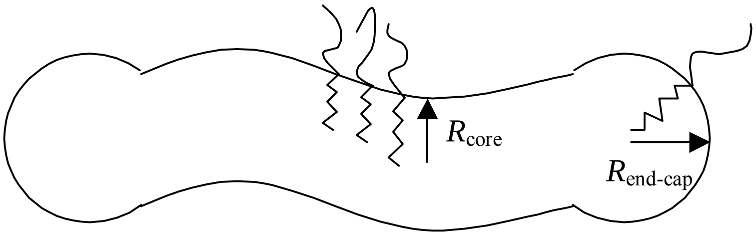

Figure 5.7: Schematic representation of spherical end-caps on a rod-like micelle. The radius of the end-caps ($R_{end\text{-}cap}$) is larger than the cross-sectional radius (R_{core}).[54]

The length of the rod-like micelles (Table 5.4) increases significantly with tail length from ~130 Å for $Gem_{12}E_{10}$ to 652.4 Å for $Gem_{14}E_{10}$. $Gem_{20}E_{15}$ behaves more like $Gem_{12}E_{10}$ with a length of ~130 Å. The large increase in length with the addition of two carbons to the tail is rationalised with the packing parameter by considering that the head groups are about the same size, yet the radius increases by ~2 Å, producing a significant increase in the volume. This increases the packing parameter sufficiently to drive the formation of longer micelles.

The ρ_{shell} values (Table 5.4) correspond to $n_{D_2O/EO}$ values of 5.0 and 7.0 for $Gem_{12}E_{10}$ and $Gem_{12}E_{15}$, 2.4 and 6.3 for $Gem_{14}E_{10}$ and $Gem_{14}E_{15}$, and 3.4, 8.0 and 14.2 for $Gem_{20}E_{15}$, $Gem_{20}E_{20}$ and $Gem_{20}E_{30}$. These are much larger than the 1.2 – 2.0 $n_{D_2O/EO}$ values measured for conventional surfactants.[105,106] This is not due to these being gemini surfactants but because the conventional surfactants studied have much smaller head groups (e.g. E_4 and E_5) compared with E_{10} to E_{30}. The larger head groups extend further into solution, producing a significantly higher percentage of solvent in the shell.

The rod-like micelles have smaller ρ_{shell} values than the spherical micelles. This corresponds to the spherical micelles containing more water in the core than the rod-like micelles and is consistent with the spherical micelles having larger, more hydrated head groups.

In summary, the 1wt% gemini surfactants at 25°C have spherical micelles for the larger head groups, and rod-like micelles for the smaller head groups. This is explained by the packing parameter, which predicts a sphere to rod transition as the area per head group is reduced. Further as the tail length is increased (from 12 to 14 carbons) the rods become longer. This is also explained by the packing parameter, which predicts a sphere to rod transition as the tail length is increased (provided the area per head group remains constant).

5.2.2 Concentrated Solutions of Gemini Surfactant Micelles

SANS data is shown in Figure 5.8a-c for concentrated samples of $\text{Gem}_{20}\text{E}_{15}$, $\text{Gem}_{20}\text{E}_{20}$ and $\text{Gem}_{20}\text{E}_{30}$ respectively. Samples were at 1wt%, 2wt% ($\text{Gem}_{20}\text{E}_{15}$ only), 5wt% and 10 wt%. As the concentration increases the scattering at low Q decreases indicating repulsions.[87] The repulsions become noticeable with increased concentration because the volume fraction of micelles becomes large enough to produce spatial correlations between them.[87]

The mean chord values are given in Table 5.5 and in general show a decrease in micelle size as the solution becomes more concentrated. The mean chord lengths for $\text{Gem}_{20}\text{E}_{15}$ initially increase ~5 Å, from 1 wt% to 2 wt%, before decreasing ~11 Å from 2 to 10 wt%. The initial increase indicates a growth in the micelles, although the decrease is peculiar. For $\text{Gem}_{20}\text{E}_{20}$ a decrease of 5 Å from 1 to 5 wt% then 9 Å from 5 to 10 wt% is observed. Similar behaviour is observed for $\text{Gem}_{20}\text{E}_{30}$, which decreases 9 Å from 1 to 5 wt% and then 7 Å from 5 to 10 wt%. These results are also peculiar.

From 1 wt% to 2 wt% the scattering of $\text{Gem}_{20}\text{E}_{15}$ shows a slight increase at low Q (Figure 5.8a). At 5 wt% a large decrease is seen and at 10 wt% a small peak forms. The peak corresponds to the particles becoming locally ordered with an average

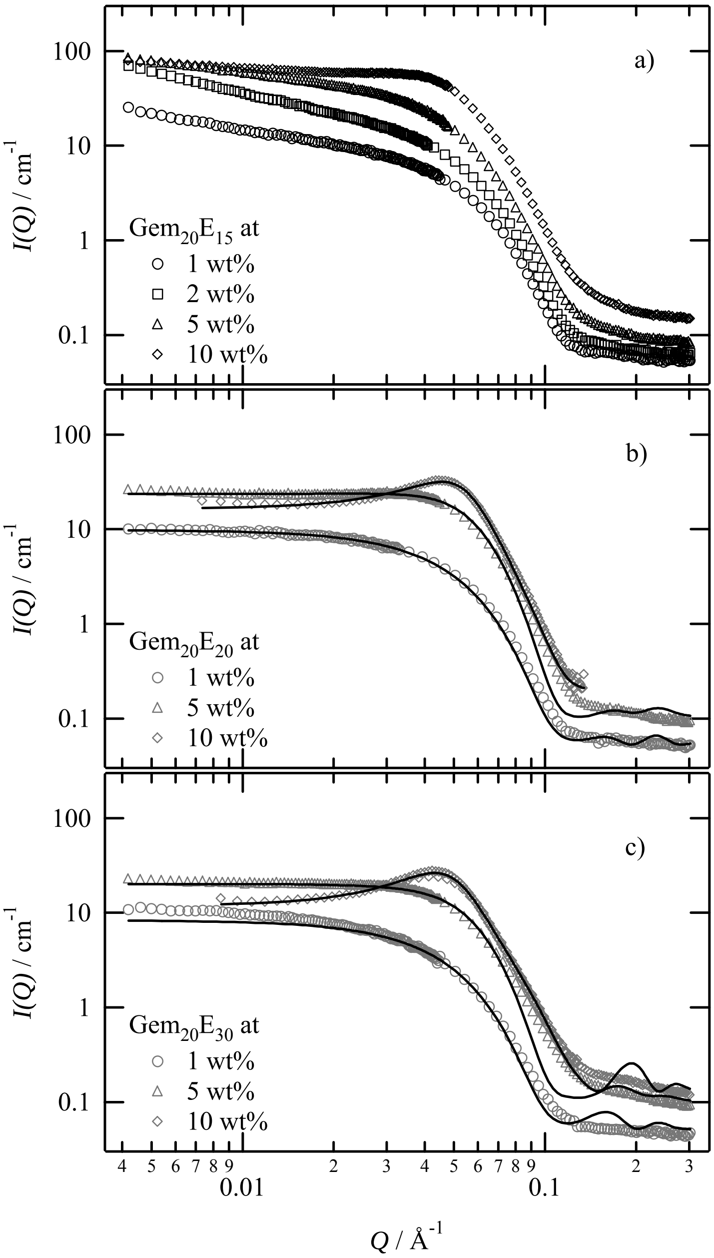

Figure 5.8: SANS data for a) Gem$_{20}$E$_{15}$, b) Gem$_{20}$E$_{20}$ and c) Gem$_{20}$E$_{30}$ at 1wt% (circles), 2wt% (squares, Gem$_{20}$E$_{15}$ only), 5 wt% (triangles) and 10wt% (diamonds). Scattering at low *Q* decreases with increased concentration due to repulsions between micelles. Hard sphere fits are shown for Gem$_{20}$E$_{20}$ and E$_{30}$ (see Table 5.6 for fitting values).

	1wt%	**2wt%**	**5wt%**	**10wt%**
$Gem_{20}E_{15}$	74 ± 3	79 ± 2	76 ± 2	67 ± 1
$Gem_{20}E_{20}$	71 ± 3	—	66 ± 1	57 ± 3
$Gem_{20}E_{30}$	75 ± 4	—	66 ± 2	59 ± 1

Table 5.5: Mean chord lengths for concentrated $Gem_{20}E_m$ surfactants. For $Gem_{20}E_{15}$ $\langle l \rangle$ initially increases by 5 Å, then decreases with concentration to 67 Å at 10 wt%. Both $Gem_{20}E_{20}$ and $Gem_{20}E_{30}$ show a drop of 5 to 9 Å between 1 and 5 wt% indicating a reduction in micelle size with concentration. A further decrease of ~8 Å is seen when the concentration is doubled to 10 wt%, indicating a further decrease in micelle size.

centre to centre distance (*D*) equal to: [83]

$$D = \frac{2\pi}{Q_{\text{peak}}}$$

where Q_{peak} is the Q value of the peak. Q_{peak} is ~0.04 Å^{-1}, which gives D ~157 Å. This is much larger than the cross-sectional diameter of 74 Å obtained from fitting the 1 wt% data.

For $Gem_{20}E_{20}$ a small peak is observed at 5 wt% and a much larger peak at 10 wt%. Q_{peak} is ~0.045 Å^{-1} giving D ~140 Å, which is much larger than the diameter of 95 Å obtained by converting the 1 wt% mean chord length to an equivalent spherical radius, and fails to explain its decrease. At 10 wt% the mean chord length gives a diameter of 76 Å, which is almost half *D*.

For $Gem_{20}E_{30}$ no peak is observed at 5 wt% but a large peak is observed at 10wt%. Q_{peak} is ~0.042 Å, which corresponds to D ~150 Å. This is a slightly larger distance between micelles than observed for $Gem_{20}E_{20}$, which can be explained by considering that there are fewer micelles in the $Gem_{20}E_{30}$ solution at the same wt% since there is more surfactant required for each micelle.

Interacting micelles can be fit by dividing the scattering into a form factor (*P(Q)*, which is the scattering of the individual particles derived previously) and a structure term (*S(Q)*, which is due to correlations between particles):[87]

$$I(Q) = P(Q)S(Q)$$

Surfactant	Volume Fraction	R_{core} (Å)	t_{shell} (Å)	p	ρ_{shell}	χ^2
Gem$_{20}$E$_{20}$						
1 wt%	—	26.0	26.1	—	5.2	—
5 wt%	0.11	25.4	23.2	0.09	3.9	53.86
10 wt%	0.21	31.3	24.0	0.07	5.1	33.37
Gem$_{20}$E$_{30}$						
1 wt%	—	22.8	29.9	—	5.6	—
5 wt%	0.084	21.1	26.5	0.12	3.7	20.41
10 wt%	0.21	32.0	28.1	0.00	5.5	40.65

Table 5.6: Best fit values for Gem$_{20}$E$_{20}$ and Gem$_{20}$E$_{30}$ at 5 wt% and 10 wt%. The 1 wt% fits from Table 5.4 are included for comparison. Volume fraction is the total volume fraction of interacting micelles, R_{core} is the core radius, t_{shell} is the shell thickness, *p* is the polydispersity (from the Schulz distribution given in Equation 3.8), ρ_{shell} is the SLD of the shell and χ^2 is a goodness of fit parameter (see Appendix A10).

This expression is only exact for monodisperse, spheres but is often used as an approximation for polydisperse spheres or *slightly* elongated particles.[87] It is not valid for highly elongated micelles.

The SANS data for the concentrated gemini surfactants was fit using a poly core-shell form factor[87] and a hard sphere structure factor (using the Percuss Yevic closure).[116] The fitting parameters are the core radius, the shell thickness, the polydispersity (see Equation 3.8) the shell SLD and the volume fraction of micelles. Best fits are shown in Figure 5.8 and given in Table 5.6.

Decent fits are obtained at low *Q* for all surfactants, and fit the interaction peak well for Gem$_{20}$E$_{20}$ and Gem$_{20}$E$_{30}$. The fits for the 5 wt% gemini surfactants are significantly poorer at higher *Q*, where they fall too sharply. This suggests the micelles are not strictly not hard spheres but interact with a soft repulsion, caused by interpenetration of the ethylene oxide head groups. This is seen in Figure 5.9, which compares the structure factor for the hard sphere repulsion (solid line) with the structure factor for a hard sphere plus exponential decay (using the Hayter/Penfold[117]

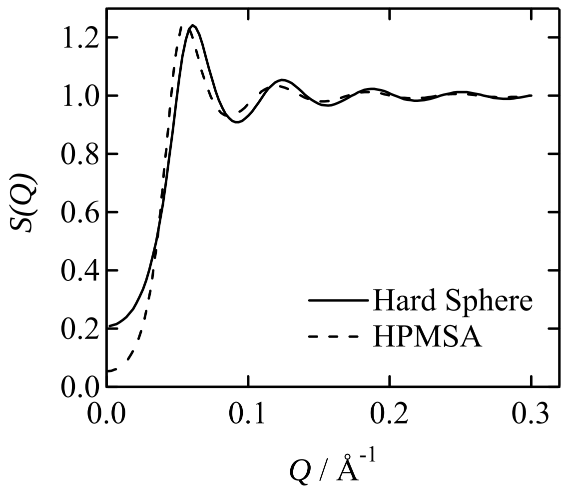

Figure 5.9: Comparison of the hard sphere structure factor (solid line) with the HPMSA structure factor[117] (dashed line), which is derived from an interaction potential consisting of a hard sphere plus an exponential repulsion.

Mean Spherical Approximation). The first peak gives rise to the interaction peak observed in the experimental data and decays away faster for the hard sphere repulsion, as is observed for the experimental data. The potential of the later model is probably incorrect for nonionic micelles and its additional complexity provides no additional information, thus it was not used to fit the data.

The R_{core} values (Table 5.6) decrease slightly from 1 wt% to 5 wt% and then increase for 10 wt% (by ~5 Å for $Gem_{20}E_{20}$ and ~11 Å for $Gem_{20}E_{30}$).

t_{shell} decreases by ~3 Å from 1 wt% to 5 wt% (for both surfactants), before increasing about 1 Å from 5 wt% to 10 wt%.

The polydispersity is fairly low (c.f. Figure 3.7) for all surfactants and produced only slightly better fits.

ρ_{shell} decreases from 1 wt% to 5 wt%, indicating a loss of water from the shell, and then returns to its original value, from 5 wt% to 10 wt%. This is consistent with the behaviour of t_{shell}, which decreases in size from 1 wt% to 5 wt% (excluding water in the process) and then increasing again from 5 wt% to 10 wt%.

The fit volume fractions are ~0.1 for the 5 wt% surfactants and ~0.2 wt% for the 10 wt% surfactants. Because the density of the surfactant is approximately the same as the solvent the volume fraction should be approximately the same as the weight fraction (i.e. 0.05 and 0.1). The discrepancy can be accounted for by the large volume of water in the shell, which increases the volume fraction of the micelles.

5.2.3 Gemini Surfactants at Elevated Temperatures

The SANS data for 1wt% $Gem_{12}E_{10}$, $Gem_{14}E_{10}$ and $Gem_{20}E_{15}$ are given in Figure 5.10a-c from 20°C up to the 1wt% cloud temperatures. For $Gem_{12}E_{10}$ Figure 5.10a shows a significant increase in the scattering in the intermediate region, suggesting an increase in the elongation of the micelles, whilst no change is observed at high Q region, suggesting the smallest dimensions do not change. At 20°C (diamonds) and 25°C (flat diamonds) only a slight increase in scattering is observed in the intermediate region, suggesting nearly spherical micelles or short rod-like micelles. At 32°C (triangles) the scattering increases and at 39°C (squares) the scattering approaches the Q^{-1} dependence expected for long, rigid rods.[111] A further increase to 48°C shows an increase in scattering above the Q^{-1} dependence, due most probably to micelle interactions.

Figure 5.10b shows that at 20°C and 25°C $Gem_{14}E_{10}$ already scatters as Q^{-1} due to the presence of rigid rod-like micelles,[111] as discussed in Section 5.2.1.2. Increasing the temperature towards the cloud point (T_c = 46°C) causes the scattering to increase at very low Q, while the scattering at high Q does not change. Further increases in temperature above the cloud temperature (see Appendix A12) show a large increase in scattering at low Q due to the formation of droplets as the solution begins to phase separate.

For $Gem_{20}E_{15}$ Figure 5.10c shows only a slight increase in the scattering at low Q as the temperature is increased by 28 degrees from 20°C to 48°C. Then over a 10 degree increase to 58°C the scattering jumps to a Q^{-1} dependence, changing only slightly with a further increase of 18 degrees to 76°C.

For each of these surfactants the SANS data indicates elongation at low temperatures before approaching a Q^{-1} dependence several degrees below the cloud temperature. That is, short rigid rod-like micelles[111] that grow larger as the cloud temperature is approached. As mentioned previously, however, SANS can not distinguish unambiguously between interacting spherical micelles and long rod-like micelles.[110] This ambiguity has been resolved by measuring the viscosity of $Gem_{20}E_{15}$ as a function of both concentration and temperature.

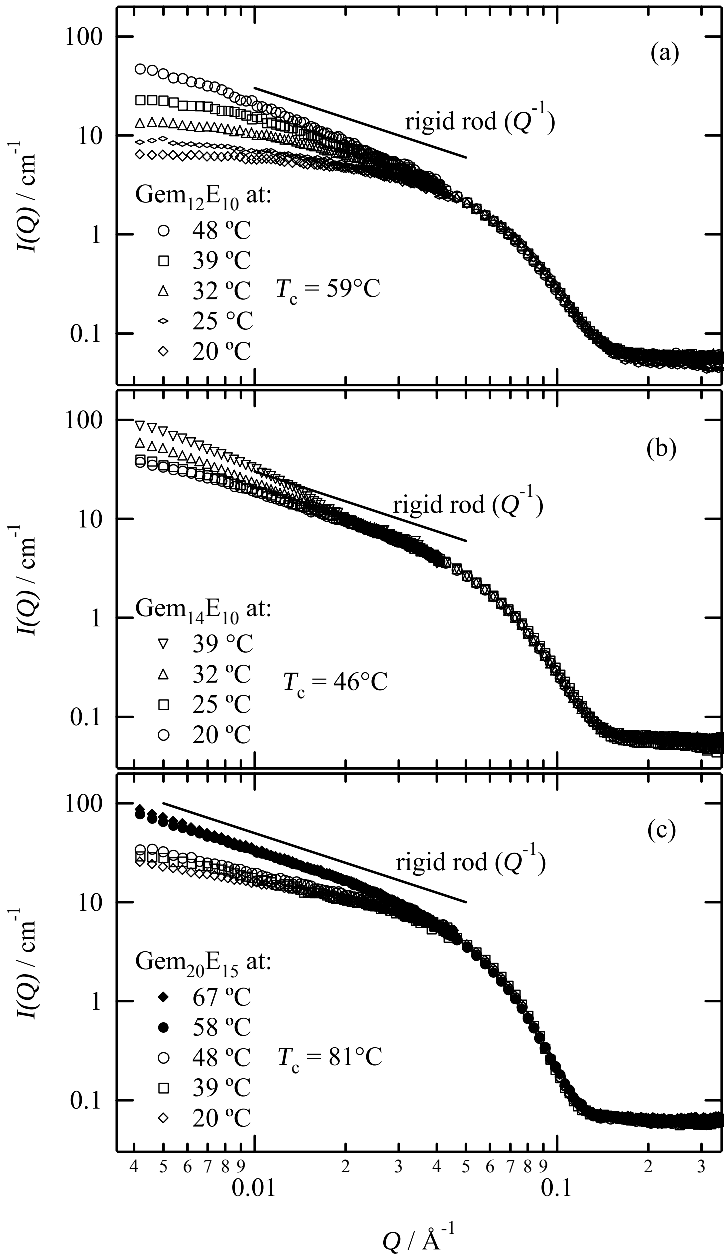

Figure 5.10: Scattering vs temperature for 1 wt% solutions of a) Gem$_{12}$E$_{10}$, b) Gem$_{14}$E$_{10}$ and c) Gem$_{20}$E$_{15}$ in D_2O. T_c is the cloud temperature for each surfactant in D_2O (see Table 5.1)

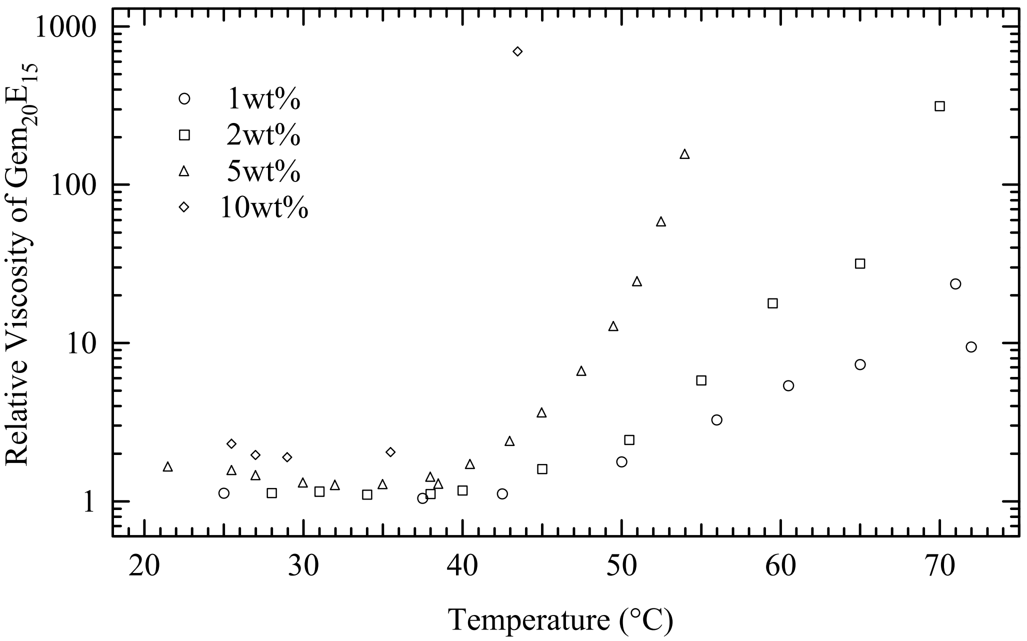

Figure 5.11: logη_r vs temperature for of Gem$_{20}$E$_{15}$ at 1wt% (circles), 2 wt% (squares), 5wt% (triangles) and 10wt% (diamonds). The viscosity decreases slightly up to ~40°C and then increases rapidly. Almost a factor of 10 increase is observed at 1wt% over 30 degrees (from 40°C to 70°C) and a factor of 100 increase for 5wt% over 20 degrees (from 40°C to 60°C). The 10wt% increases even more rapidly, becoming viscoelastic at ~50°C and gelling at ~60°C.

logη_r vs temperature is shown in Figure 5.11, where η_r is the relative viscosity (i.e. viscosity of surfactant divided by viscosity of the solvent). It shows only a slight change in η_r up to ~40°C and then a rapid increases. At 1 wt% η_r increases by a factor of 10 over 30 degrees and at 10 wt% was observed visually to became viscoelastic at ~50°C (not shown on graph), eventually gelling at ~60°C. The increase in viscosity at 40°C corresponds well with the large increase in scattering observed between 48°C and 58°C and supports the growth of rigid rod-like micelles.

Figure 5.12a shows logη_r vs concentration at 30°C, 40°C, 50°C and 60°C. The viscosity increases rapidly with concentration, becoming more noticeable as the temperature is increased. The 30°C and 40°C data are expanded in Figure 5.12b, for comparison with the Einstein viscosity law for non interacting spheres:[78,118]

$$\frac{\eta_{sphere}}{\eta_{solv}} \approx 1 + 2.5\phi$$

where ϕ is the volume fraction of spheres. This is plotted as a solid line, assuming the

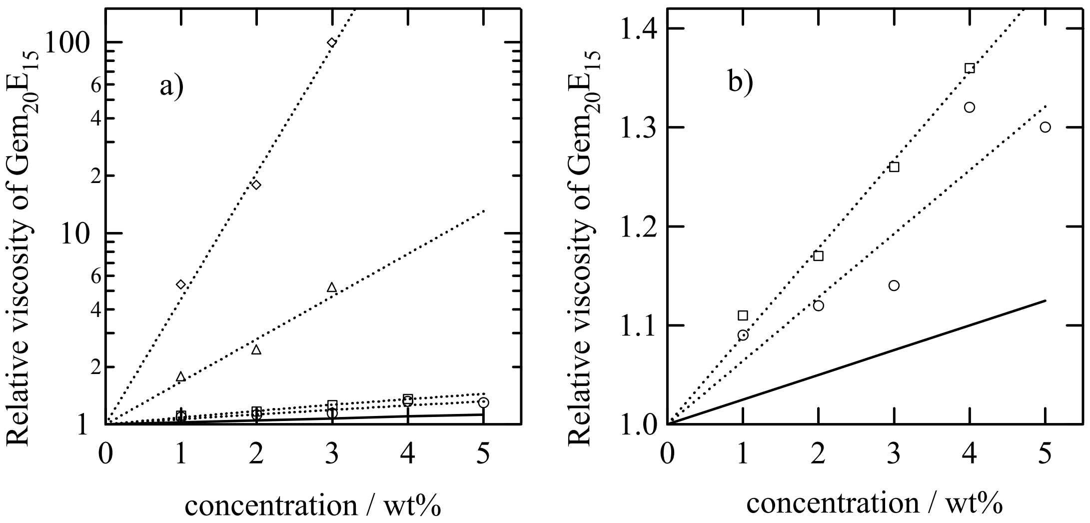

Figure 5.12: a) logη_r vs concentration and b) η_r vs concentration for Gem$_{20}$E$_{15}$ at 30°C (circles), 40°C (squares), 50°C (triangles) and 60°C (diamonds). Dotted lines are best fit curves and the solid line (seen best in Figure b) is the Einstein viscosity law for spheres.[78,118] The viscosities are clearly too large for spherical micelles, supporting the interpretation of the SANS data that Gem$_{20}$E$_{15}$ forms rod-like micelles.

volume fraction is approximately equal to the weight fraction. In Figure 5.12b the viscosities at 30°C and 40°C are approximately 2 to 3 times larger than that expected for spheres with the Einstein law. At 50°C and 60°C the viscosity is much larger and can only be seen as on the log axis in Figure 5.12a. Such large viscosities at such low concentrations can only be due to entanglements of rod-like micelles.

No viscosity increases was observed with increasing temperature for the shorter tailed Gem$_{12}$E$_{10}$ and only a slight increase for Gem$_{14}$E$_{10}$ was observed just prior to the cloud temperature,[119] despite both approaching a Q^{-1} scattering dependence. This large viscosity increase with increasing alkyl tail length has also been observed by Rehage and Hoffmann[120] for alkyltrimethylammonium salicylate surfactants containing rod-like micelles. For 1 mM solutions the viscosity increased by a factor of 10 when the tail was increased from C$_{12}$ to C$_{14}$, and then by a factor of 100 when increased from C$_{14}$ to C$_{16}$.

5.3 Discussion

The micelle morphologies for the 1 wt% gemini surfactants at 25°C are summarised in Table 5.7. The smallest head group surfactants (E$_{10}$) form rod-like micelles, which grow with tail length. The E$_{15}$ surfactants are spherical except for the largest tail ($Gem_{20}E_{15}$), which forms short rod-like micelles. The rod-like micelles become longer as the temperature is increased towards the cloud temperature. At increased concentration the $Gem_{20}E_m$ surfactants show excluded volume interactions, forming noticeable micelle correlations at 10 wt%.

		ethoxylation number			
		10	**15**	**20**	**30**
Carbon atoms per tail	**12**	short rod-like micelle	spherical micelles	—	—
	14	long rod-like micelles	spherical micelles	—	—
	20	—	short rod-like micelles	spherical micelles	spherical micelles

Table 5.7: Summary of gemini surfactant morphologies at 1 wt% and 25°C. The smaller head group E_{10} surfactants form rod-like micelles that grow as the tail length is increased. The E_{15} surfactants form spherical micelles becoming rod-like with increased tail length.

Comparison to conventional nonionic surfactants is difficult due to a large number of differing results in the literature. The size of conventional nonionic micelles was initially studied by measuring the molecular weight of micelles by light scattering and converting to aggregation numbers.[70] These studies found significant micellar growth as the temperature is increased.[70] For example, the aggregation number of $C_{12}E_6$ (with a cloud temperature of 45°C) increased from 140 at 15°C to 4000 at the cloud temperature.[121] The aggregation numbers are much too large for spherical micelles (~56[*]) and were attributed to the formation of "giant micelles".[121,122]

The shape of nonionic micelles was initially studied with increasing temperature by Zulauf *et al.*[105,123,124] and Triolo *et al.*[106,107] using SANS. Studying C_8E_4,[123] C_8E_5[105,123,124] and $C_{12}E_8$,[124] Zulauf *et al.* found increased scattering at low Q with increasing temperature, which they interpreted as attractions between spherical micelles. They proposed that the micelles form loose "clouds" due to a short range

---

[*] $N_{agg} = V_{mic}/v_{tail}$, where V_{mic} is calculated using l_c as the radius and v_{tail} from Tanford,[6] see Equations 2.1 and 2.2.

attraction that became stronger as the temperature approached the cloud point. Triolo *et al.* studying $C_{12}E_6$[107] and $C_{12}E_8$[106] found a similar scattering behaviour and attributed it to critical concentration fluctuations between spherical micelles. However, Lum Wan *et al.*[110] have shown (for $C_{12}E_6$ at least) that this data can *also* be interpreted as polydisperse, rigid rod-like micelles and that SANS, in isolation of other techniques, is not capable of distinguishing between the two models.

More recently Glatter *et al.*[115] have studied $C_8E_{3,4,5}$, $C_{10}E_4$ and $C_{12}E_{5,6}$ from 3°C up to the cloud temperatures, with a combination of SANS and viscosity. Using a more complex method[125,126] than previous studies, they interpreted their data as interacting, rod-like micelles. They found a sphere-to-rod transition with increasing temperature. Further, surfactants with small head groups, such as C_8E_4 (T_c ~37°C) and $C_{12}E_5$ (T_c ~30°C) form rod-like micelles even at low temperatures.

The general trends for the gemini surfactants compare well with this study by Glatter *et al.*.[115] In particular, surfactants with small head groups form rod-like micelles at low temperatures, while larger head groups produce spherical micelles. Further, as the cloud temperature is approached the micelles undergo a sphere-to-rod transition and micellar growth.

Chapter 6: Phase Behaviour of Nonionic Gemini Surfactants

6.1 Introduction

In the last chapter the morphology of micelles in isotropic solution was considered. In this chapter the behaviour of surfactants at higher concentrations is explored, specifically, the formation of mesophases.

The theoretical treatment of mesophase formation has been dealt with by Mitchell *et al.*[71] by considering interactions *within* micelles (intramicellar) and interactions *between* micelles (intermicellar). Intramicellar interactions determine the shape of micelles and has been treated in Section 2.2 using the packing parameter ($p = v/a_\mathrm{o}l_\mathrm{c}$). As stated previously, a_o decreases with increasing concentration leading to less curved aggregates.

Intermicellar interactions become important as the concentration is increased and ordered mesophases cannot form without them. For nonionic micelles these are predominately attractive van der Waals attractions and steric repulsions.[71] These give rise to three main transitions, described below.

First the *disorder/order transition*. As the volume fraction of a surfactant is increased the solution becomes crowded with micelles in a disordered state. The micelles interacting through repulsions interfere with each other until a concentration is reached beyond which it becomes energetically unfavourable to add more micelles to the system. At this concentration, it becomes energetically favourable for the micelles to form an ordered phase coexisting with the disordered micelle solution. Theoretical studies of spheres with only a hard core interaction crystallise at a volume fraction of ~0.5, even though random close packing occurs at ~0.74.[127] For hard rods the transition occurs at ~0.7.[71] This *disorder/order transition* also causes randomly dispersed micelles to form ordered phases. Thus spherical micelles will close pack to form a cubic phase, rod-like micelles will close pack to form a hexagonal phase and bilayers will align to form a lamellar phase.[71] The volume fraction of these transitions in micelle systems will be lower than for hard core interactions. This is because the polyethylene head groups extend into solution (see Chapter 5), increasing the effective volume fraction.

Second is the *micelle shape* transition. As the volume fraction is increased the micelles within an ordered phase will be forced closer together. Mitchell *et al.*[71] have argued that intermicellar repulsions will oppose intramicellar curvature and the area per head group is forced to decrease. This eventually leads to *micelle shape transitions*.[54] Thus, at high enough concentration a cubic phase will transform to a hexagonal phase as the spherical micelles undergo a sphere to rod transition.[71] Similarly, a hexagonal phase will transform to a lamellar phase as the micelles undergo a rod to bilayer transition.[71]

Third is *secondary aggregation*. If intermicellar attractions are strong enough to overcome repulsions then the micelles will aggregate together. This leads to the formation of two separate phases, one rich in aggregated micelles and the other lean in micelles,[71] where the composition of the two phases are determined by the balance of attractive and repulsive forces. This mechanism gives rise to the formation of dilute solution/lamellar phase coexistence, which will be discussed later. It was also used by Mitchell *et al.*[71] to explain the clouding behaviour of nonionic surfactants at elevated temperatures. More recent theories[108,109] suggest that the formation of a network of branched rod-like micelles at the cloud point may be responsible. This is supported by recent cryo-TEM studies of $C_{12}E_5$,[128] however, the mechanism is still open to debate.

6.2 Results

The partial phase diagrams for the $Gem_{20}E_m$ surfactants were constructed from room temperature to ~60°C using a combination of flooding experiments and DIT-NIR,[95] as described in Section 3.3.1.5. The DIT data is given in Appendix A11.

Solid lines on phase diagrams indicate boundaries determined with reasonable confidence, while dashed lines are extrapolated from solid lines or estimated from the known phase behaviour of conventional surfactants. Phase labels used in this chapter are L_1, L_2, etc for liquid isotropic phases. L_1 is used for the micellar solution and L_2 for concentrated surfactant. I_1 is used for micellar cubic phases with a close packing of either spherical or slightly elongated micelles. H_1 is used for regular hexagonal phases consisting of hexagonally packed rod-like micelles. V_1 is used for bicontinuous cubic phases, constructed of curved bilayers. L_α is used for lamellar phases consisting of regularly spaced bilayers. W is a dilute surfactant solution, which does not contain micelles. S is used to denote the presence of solid surfactant, which is present as a two-phase mixture of solid surfactant with the closest phase.

6.2.1 Phase Behaviour of $Gem_{20}E_{10}$

The partial phase diagram for $Gem_{20}E_{10}$ is shown in Figure 6.1 from room temperature to ~60°C. It exhibits only two mesophases. At room temperature only a L_α phase forms. The L_α phase forms a coexistence region with a dilute surfactant solution (W) on one side and solid surfactant on the other (S). The boundary for W was not determined, but solutions prepared at 10^{-3} M (< 0.001 wt%) during CMC studies were noticeably turbid, indicating extension of the two-phase region to very low concentrations. The W/L_α boundary is at 30 wt%. From flooding experiments the L_α phase melts at ~63°C.

As the temperature is increased a narrow, isotropic phase (L_3) forms between W and L_α. The L_3 phase is a fluid phase (unlike cubic phases). Turbidity measurements on a 1 wt% showed a sharp increase in scattering at 32°C, caused by entering the W + L_3 region. The increase in turbidity is probably because of the change in volume fractions of the coexisting phases W + L_α and W + L_3 at 32°C. DIT-NIR at 37°C and 45°C measured L_3 to be at 10 wt% and 16 wt% respectively, but was not sensitive enough to determine the width of the narrow composition range. The L_3 phase exhibits shear birefringence (i.e. became birefringent when shaken between crossed polarisers), which has been reported for L_3 phases in many conventional surfactant systems.[69]

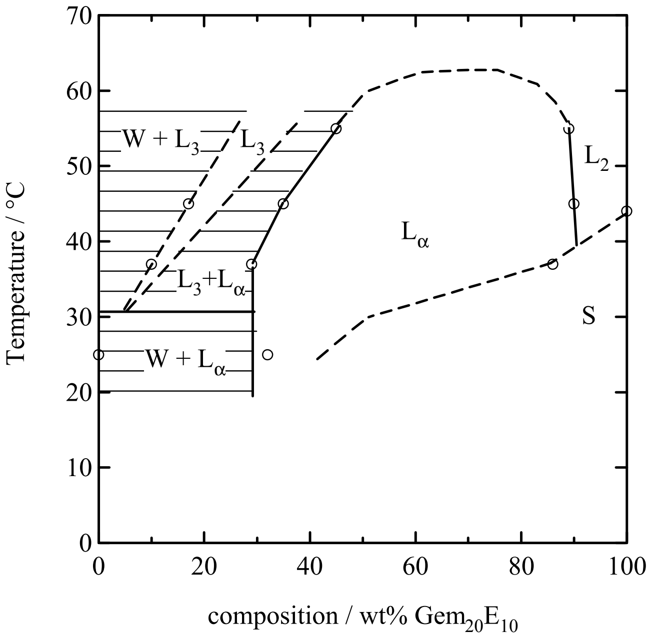

Figure 6.1: Partial phase diagram for Gem$_{20}$E$_{10}$, from room temperature to 60°C. A L$_\alpha$ phase forms in coexistence with W at room temperature and 29 wt%. At 32°C a L$_3$ phase forms on the low concentration side of the L$_\alpha$ phase. No other phases where observed.

The formation of the L$_\alpha$ phase in preference to H$_1$ and I$_1$ phases indicates that a_o for Gem$_{20}$E$_{10}$ is small and can thus only form bilayers. The formation of bilayers is consistent with SANS results, which showed that micelle curvature increased with ethoxylation number giving rod-like micelles for Gem$_{20}$E$_{15}$ and spherical micelles for both Gem$_{20}$E$_{20}$ and Gem$_{20}$E$_{30}$. The formation of the two phase region (W + L$_\alpha$) is due to *secondary aggregation*,[71] where van der Waals attractions between bilayers are strong enough to overcome entropy and repulsions to bring the bilayers together and form a separate L$_\alpha$ phase. The boundary of the W/L$_\alpha$ phase is determined by the balance of attractive and repulsive forces between bilayers.[71]

The L$_3$ phase has been observed in many conventional nonionic surfactant systems[71,129] and occurs when the miscibility gap (i.e. the cloud region) intersects a mesophase.[69] The L$_3$ phase has also been observed in many three and four component surfactant mixtures. [69] For cetylpyridiniumchloride/hexanol/brine Porte *et al.*[130,131] proposed a flexible bilayer with a disordered, isotropic “sponge like” morphology (Figure 6.3), where the bilayer divides the water into two channels. This “sponge phase” morphology was confirmed for the L$_3$ phase in conventional nonionic surfactants by Strey *et al.*,[132] working with $C_{12}E_5$ (Figure 6.2). This structure is shear birefringent because the shear forces align the bilayers to form a L_α phase.[133]

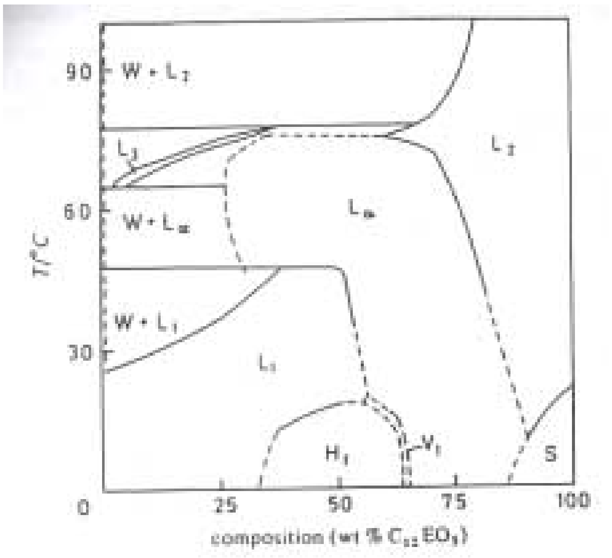

Figure 6.2: Phase diagram of $C_{12}E_5$ from Mitchell *et al.*.[71]

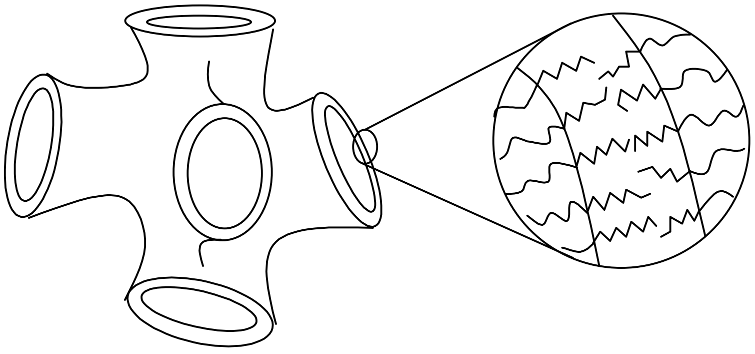

Figure 6.3: Possible "sponge phase" (L_3) morphology. The bilayer (shown on right) divides the water into two channels.

6.2.2 Phase Behaviour of $Gem_{20}E_{15}$

The partial phase diagram for $Gem_{20}E_{15}$ is shown in Figure 6.4. A H_1 phase forms from L_1 at 25 wt%, and coexists with solid surfactant at higher concentration. Between 35°C and 36°C a V_1 phase forms and at a higher concentration a L_α phase forms. Thermodynamically these must form at different temperatures[69] but the temperature difference could not be resolved. The solid surfactant also begins to melt, forming L_2. Both H_1 and V_1 melt below 76°C, while L_α survives beyond this to an undetermined temperature. The V_1 phase forms next to the H_1 phase at 65 wt% and extends to the formation of the L_α phase at 74 wt%. The L_α phase extends from 74 wt% to 80 wt%, before the formation of L_2.

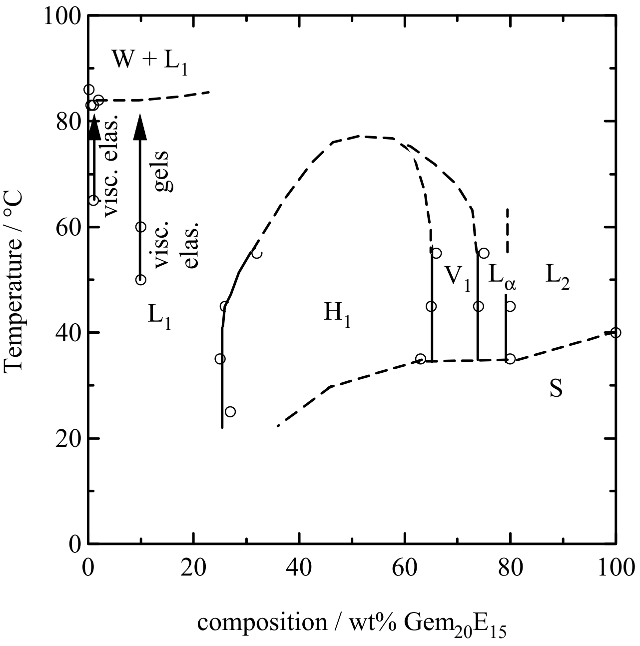

Figure 6.4: Partial phase diagram for $Gem_{20}E_{15}$. A H_1 phase forms at room temperature, V_1 and L_α phases form at ~34°C. None of the phases melt before 62°C. The cloud point is at 83°C. A 1wt% solution becomes viscoelastic at ~65°C, and a 10 wt% solution becomes viscoelastic at 50°C and gels at 60°C.

The cloud temperature is 83°C as measured from solutions at 0.1, 0.2, 0.5, 1.0, 2.0, 5.0 and 10 wt%. As the cloud temperature was approached the viscosity increased dramatically (see Figure 5.11). At 65°C a 1 wt% solution became viscoelastic (i.e. bubbles recoil when the solution is rotated), which is previously unreported for nonionic surfactants. At 50°C a 10 wt% solution became viscoelastic and at 60°C it formed a gel. The formation of the gel greatly increased the time of separation and the clouding temperature for the 5 and 10 wt% solutions could not be determined with accuracy. However, they both separated below 85°C and this region is indicated with a dashed line.

The formation of the H_1 phase is a *disorder/order transition*,[71] where disordered rod-like micelles in L_1 order into a close packed hexagonal array. This occurs when the volume fraction of surfactant becomes too large to support disordered micelles.

The transitions of H_1 to V_1 and V_1 to L_α with increased concentration are *shape transitions*[54,71] of rod-like micelles in H_1 to bilayers in L_α. The structure of the V_1 phase was not determined but must have an intermediate curvature between rods and bilayers, such as in Figure 2.13b. The shape transition occurs because a_0 decreases with increasing surfactant composition until a rod to bilayer transition occurs.

The phase separation at the cloud point (W + L_1) is due to *secondary aggregation*,[71] producing a surfactant rich solution (L_1) coexisting with a surfactant lean solution (W).[71]

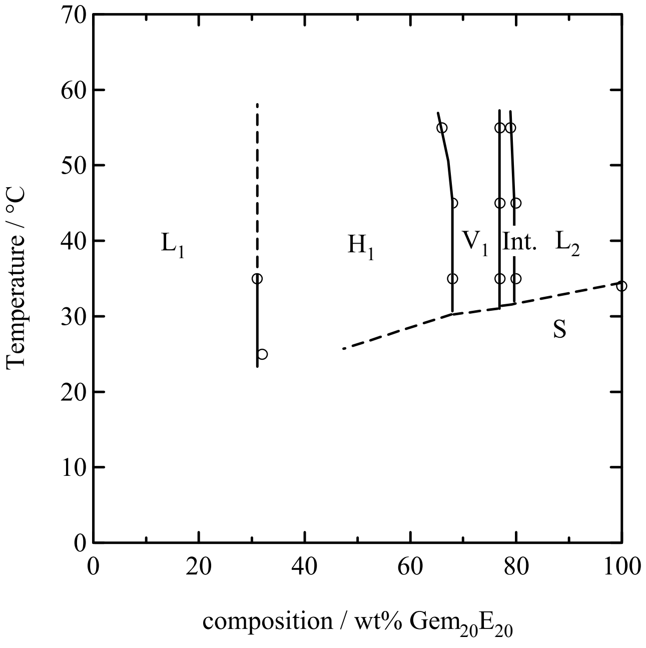

Figure 6.5: Partial phase diagram for $Gem_{20}E_{20}$. At room temperature a H_1 phase forms at 32 wt%. At 31°C a V_1 phase forms at 68 wt% and an intermediate phase (Int.) at 77 wt%.

6.2.3 Phase Behaviour of $Gem_{20}E_{20}$

The partial phase diagram for $Gem_{20}E_{20}$ is shown in Figure 6.5. A H_1 phase forms from the L_1 phase at 32 wt%.[71] At 31°C a V_1 phase forms next to H_1 and extends from 68 wt% to 77 wt%. Another phase forms next to V_1 at only a slightly higher temperature and extends over a narrow range of 77 wt% to 80 wt%, before the formation of L_2. The optical texture of this phase from flooding experiments does not correspond to L_α, (see Figure 6.6). The phase was labelled as an intermediate phase,[69] which has been used previously for phases that form between H_1 and L_α. This texture does not appear to be reported in the literature and no further attempt was made to solve its structure.

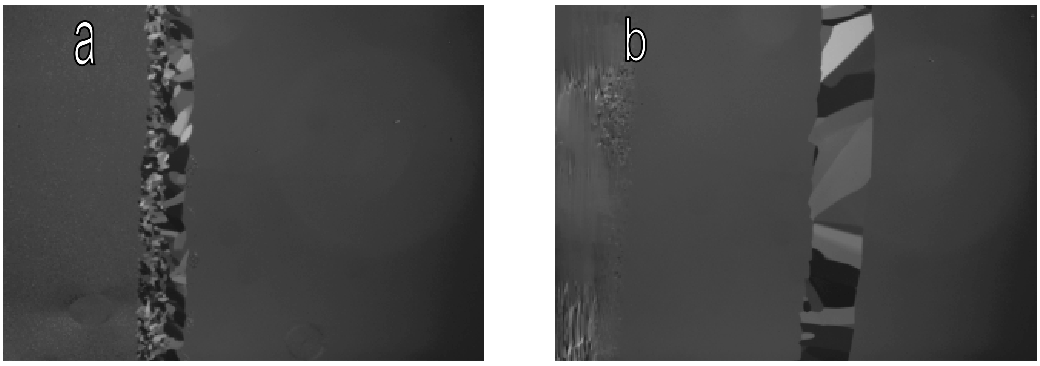

Figure 6.6: Intermediate phase (int.) observed in flooding experiments of $Gem_{20}E_{20}$ at a) 35°C and b) 40°C. The surfactant concentration increases from left to right giving only the V_1/int./L_2 phases (c.f. Figure 6.5).

None of the phases melted below 80°C and no cloud point was observed below 100°C for 1 wt% and 10 wt% solutions.

The L_1/H_1 transition is a *disorder/order transition*,[71] as in $Gem_{20}E_{15}$. The H_1/V_1 transition indicates a *shape transition*[71] from rod-like micelles to micelles with an intermediate curvature (possibly branched rods), as in $Gem_{20}E_{15}$. The formation of the intermediate phase and the lack of a L_α phase is unusual, although the formation of intermediate phases have been reported for several nonionic surfactants such as $C_{16}E_6$,[134,135] $C_{22}E_6$,[136] and nonaethylene glycol mono(11-oxa-14, 18, 22, 26-tetramethylheptacosyl) ether ($C_{30}E_9$)[137,138]. A wide variety of structures have been reported, such as the L_α^H phase, consisting of bilayers pierced with uncorrelated defects[136,139] and the tetragonal phase, consisting of bilayers pierced with regular holes, correlated between layers.[140,141] Intermediate phases are observed mainly in long tail surfactant systems,[136] which is consistent with its formation in a $Gem_{20}E_m$ surfactant.

6.2.4 Phase Behaviour of $Gem_{20}E_{30}$

The partial phase diagram for $Gem_{20}E_{30}$ is shown in Figure 6.7. The phases are $L_1/I_1/H_1$. The I_1 phase was identified from flooding experiments by the presence of deformed bubbles in an isotropic region, while the hexagonal phase produced the usual birefringent texture. The boundaries between L_1/I_1 and I_1/H_1 during flooding experiments where not sharp and thus their compositions could not be determined accurately using DIT-NIR. Equilibration times where too slow to determine the phase diagram with bulk samples, however, a 30 wt% solution flows and is L_1, while a 50 wt% sample is birefringent and is H_1, thus I_1 is between these two concentrations. Neither phase melted below 80°C. No cloud point was measured below 100°C for 1 wt% or 10 wt% solutions and no V_1, intermediate or L_α phases where found.

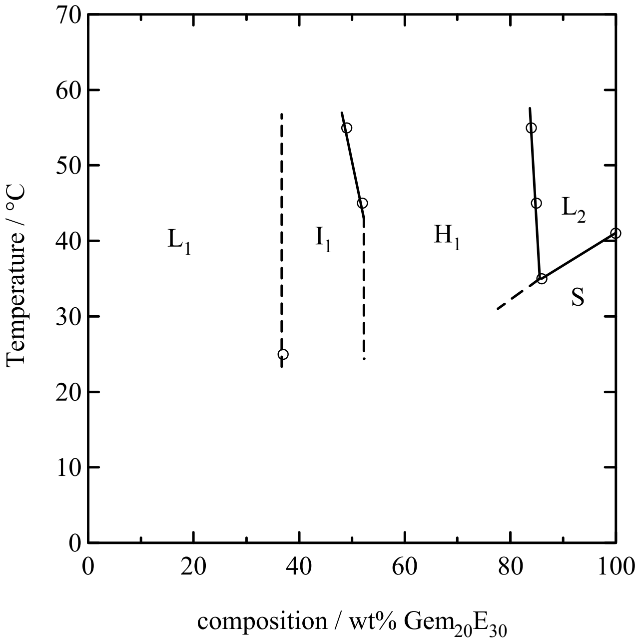

Figure 6.7: Partial phase diagram for Gem$_{20}$E$_{30}$. The phase sequence is $L_1/I_1/H_1$.

I_1 forms due to a *disorder/order transition*[71] of spherical micelles in L_1 to a close packed structure, similar to the formation of H_1 in Gem$_{20}$E$_{15}$ and Gem$_{20}$E$_{20}$. The formation of I_1, in preference to H_1 or L_α, is due to the larger a_o of Gem$_{20}$E$_{30}$. Further, a_o is too large to support the small curvature of bilayers as evidenced by the absence of V_1 and L_α phases.

6.3 Discussion

6.3.1 Phase Behaviour with Increasing EO

The effect of increasing ethoxylation number on phase behaviour is best seen in Table 6.1, which shows the lowest concentration that each phase forms at. For Gem$_{20}$E$_{10}$ a L_α forms at 29 wt% revealing low curvature. Gem$_{20}$E$_{15}$ forms a H_1 phase at 25 wt%, then a V_1 phase at 65 wt% and finally a L_α phase at 75 wt%. $Gem_{20}E_{20}$ forms a H_1 phase at 32 wt% a V_1 phase at 65 wt% and an intermediate phase at 75 wt%. $Gem_{20}E_{30}$ forms a I_1 phase at just over 30 wt% and a H_1 phase at 50 wt%. Thus the progression from bilayers with no curvature in Gem20E10 at 29 wt% to spheres in $Gem_{20}E_{30}$ at just over 30 wt% is observed, as expected for increasing a_o.

The effect of ethoxylation number is also observed with the cloud point. For E_{10} the cloud point meets the L_α phase and is approximately 32°C, for E_{15} the cloud point is 83°C and for E_{20} and E_{30} the cloud point is greater than 100°C. The increase of the cloud point with ethoxylation number is also observed with conventional nonionic surfactants.[71] The increase in cloud temperature with EO is attributed to dehydration of the head groups. This leads either to reduced repulsions between micelles,[71] or a reduction in a_o, which induces a rod to branched-rod transition as discussed in Section 6.1.

EO_n	**L_1**	**I_1**	**H_1**	**V_1**	**Int**	**L_α**
10	—	—	—	—	—	29 %
15	0	—	25 %	65 %	—	75 %
20	0	—	32 %	65 %	75%	—
30	0	> 30 %	50 %	—	—	—

Table 6.1: Lowest concentration that mesophases form for $Gem_{20}E_m$ surfactants. The columns are in order of increasing curvature (except the int. phase, which has an undetermined structure).

6.3.2 Comparison of Conventional and Gemini Surfactant Phase Behaviour

Comparison of the gemini surfactant to conventional nonionic surfactant phase behaviour seeks to answer two questions. Do the nonionic gemini surfactants behave differently from conventional nonionic surfactants? And if so, is this because they are gemini surfactants or can it be explained by other structural differences? Each gemini surfactant is compared below to conventional $C_{12}E_m$ surfactants and the similarities discussed.

Firstly, $Gem_{20}E_{10}$ may be compared to $C_{12}E_3$ and $C_{12}E_4$ (Figure 6.8a and b), which both form a W + L_α at low temperatures and a L_3 phase at higher temperatures (forming at 34°C and 46°C respectively).[71] The only major difference is that solid surfactant forms to a much higher concentration in the gemini surfactant. However, this can be attributed to the longer alkyl tail of the gemini surfactant, which is expected to have a higher melting point.[6]

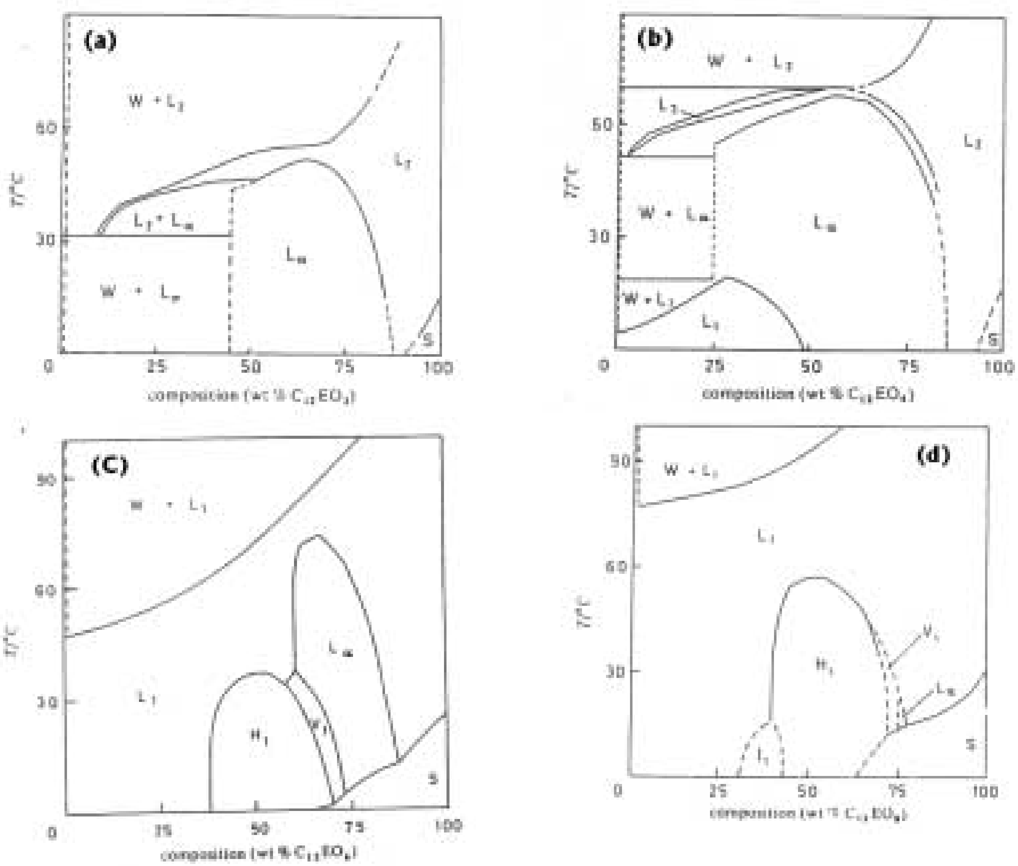

Figure 6.8: Phase diagrams for conventional surfactants: a) $C_{12}E_3$, b) $C_{12}E_4$, c) $C_{12}E_6$ and d) $C_{12}E_8$, taken from Mitchell *et al.*.[71]

$Gem_{20}E_{15}$ may be compared with $C_{12}E_6$ (Figure 6.8d), which has the phase sequence $H_1/V_1/L_\alpha$. The cloud point is at 48°C and the mesophases melt at 37°C (H_1), 38°C (V_1) and 73°C (L_α).[71] Although these temperatures are all lower than the gemini surfactant, the general trends are the same. That is, H_1 and V_1 melt before L_α. This is due to the higher stability of bilayers over more curved structures since a_o is so small. One noticeable difference is that H_1 forms at 25 wt% for $Gem_{20}E_{15}$ and at 38 wt% for $C_{12}E_6$. Mitchell *et al.*[71] have pointed out that since the L_1/H_1 transition is a disorder/order transition, depending predominantly on the volume fraction of surfactant, this boundary should not change much for different surfactants. However, SANS showed that the shell for $Gem_{20}E_{15}$ contains ~3.4 waters per EO, which is large compared to the 1.2 calculated by Hayter for the shorter EO surfactant, C_8E_5.[105] The large swelling of the gemini surfactant head groups effectively increases the volume fraction of the micelles forcing the L_1/H_1 transition to lower concentrations.

$Gem_{20}E_{20}$ does not compare directly with any conventional surfactant phase diagram available, but increasing EO from $Gem_{20}E_{15}$ to $Gem_{20}E_{20}$ reveals three major differences that can be compared to conventional behaviour: 1. the cloud point increases (to above 100°C), 2. H_1 becomes stable to higher temperatures, and 3. L_α is replaced with a different (intermediate) mesophase. These first two differences are also seen when EO is increased for the conventional nonionic surfactant $C_{12}E_6$ to $C_{12}E_8$ (Figure 6.8c and d).[71] The formation of the intermediate phase, however, appears to be unique to the gemini surfactant. Although intermediate phases have been observed in conventional nonionic surfactants (as mentioned previously in Section 6.2.3) they typically replace the V_1 phase, leaving L_α.[134,135,137] This is not the case here and the formation of the intermediate phase appears to be a property of the gemini surfactant.

$Gem_{20}E_{30}$ may be compared with $C_{12}E_{12}$, which forms a I_1 phase to 48°C and a H_1 phase to 76°C.[71] V_1 and L_α do not form. Although the melting point of I_1 could not be measured for $Gem_{20}E_{30}$ the presence of the cubic phase as the head group is increased and the disappearance of V_1 and L_α and in agreement with the behaviour of conventional surfactant behaviour.

In summary, the behaviour of the gemini surfactants is very similar to the behaviour of conventional nonionic surfactant with a few notable exceptions. These are the increased stability of the solid expected due to the longer tail length, the lower concentration of the L_1/H_1 transition due to the larger head groups and the formation of an intermediate phase in $Gem_{20}E_{20}$ next to V_1. The intermediate phase does not appear to form in the same manner as in conventional nonionic surfactants with long alkyl tails, suggesting that it is may be unique to gemini surfactant phase behaviour.

Chapter 7: Conclusions

The aims of this work were to systematically study nonionic gemini surfactants with polyoxyethylene head groups ($Gem_{20}E_m$) as a function of ethoxylation number (m), and to compare their behaviour to conventional nonionic surfactants. These surfactants are direct analogues of conventional alkyl polyoxyethylene surfactants, having a two alkyl tails connected with a six methylene spacer. The CMCs, micelle morphologies and phase behaviour of the gemini surfactants were investigated and compared to the behaviour of conventional surfactants.

7.1 Critical Micelle Concentrations

The CMCs were all ~2×10^{-7} M and revealed no change (within experimental error) with ethoxylation number. These values are smaller than previously recorded for conventional surfactant CMCs by at least one order of magnitude (c.f. the CMC of $C_{12}E_6$ ~1×10^{-6} M)[5]. However, these CMCs are much higher than predicted by simple theory (Equation 2.17) and comparison to conventional surfactants suggest that such low CMCs could be achieved with conventional surfactants with larger alkyl tails (say C_{18} or C_{20}), except for limits in the solubility of these surfactants.[6] This discrepancy was attributed to the formation of dimers at low concentrations, which lowers the free energy of micelle formation and increases the CMC.

The mixing behaviour of the gemini surfactants with both conventional an ionic and nonionic surfactants revealed ideal mixing. With the addition of only a small amount of surfactant this produces a large drop in the mixed CMC, a feature that makes these surfactants appealing for industrial applications.

A much larger CMC advantage was observed for the $Gem_{12}E_m$ and $Gem_{14}E_m$ surfactants studied by Dr Tim Davey. These surfactants have slightly higher CMCs

(4×10^{-7} to 6×10^{-7} M) than the $Gem_{20}E_m$ surfactants, but a much greater gain compared to conventional nonionic surfactants. For industrial applications these smaller surfactants show the most promise because of their much lower molecular weights.

7.2 Micelle Morphologies and Phase Behaviour

The micelle morphologies and mesophase behaviour of the nonionic gemini surfactants were in qualitative agreement with the behaviour of conventional nonionic surfactants. This behaviour was explained well with theories developed for those systems by Israelachvili *et al.*[54] and Mitchell *et al.*[71].

1 wt% $Gem_{12}E_{15}$, $Gem_{14}E_{15}$, $Gem_{20}E_{20}$ and $Gem_{20}E_{30}$ all form spherical micelles at 25°C. $Gem_{12}E_{10}$ formed *short* rod-like micelles, while the longer tailed $Gem_{14}E_{10}$ (which has a larger packing parameter value) formed *long* rod-like micelles, as expected. $Gem_{20}E_{15}$ (which has a longer tail and thus a larger packing parameter than $Gem_{12}E_{15}$) forms short rod-like micelles, also as expected.

Increasing the temperature of the $Gem_{12}E_{10}$, $Gem_{14}E_{10}$ and $Gem_{20}E_{15}$ from 20°C to the cloud temperature produced a sphere-to-rod transition. This is due to a decrease in a_o, which increases $v/a_o l_c$.[54]

Increasing the concentration of $Gem_{20}E_{30}$ created strong particle correlations due to excluded volume interactions. At just over 30 wt% the micelles undergo a disorder/order transition[71] to form a micellar cubic phase (I_1). With a further increase in concentration the micelles undergo a sphere-to-rod transition[54] to form a hexagonal phase.

Increasing the concentration of $Gem_{20}E_{20}$ also produced strong correlations between micelles. Instead of forming a I_1 phase though, the micelles undergoes a sphere-to-rod transition in the micellar phase (L_1) to form a H_1 phase. This is due to the smaller head group being unable to maintain spherical micelles as in $Gem_{20}E_{30}$. With a further increase in concentration the curvature of the micelles is reduced producing a bicontinuous cubic phase and then an intermediate phase. The intermediate phase forms in place of the normally observed lamellar phase (L_α), which is previously unreported, as intermediate phases typically form *between* H_1 and L_α phases.[134,141] Understanding this behaviour would require determination of the intermediate phase structure (possibly by x-ray crystalography), but was not pursued because it was secondary to the main aims of this project.

Increasing the concentration of $Gem_{20}E_{15}$ produced a hexagonal phase at 25 wt%. Increasing the concentration further produced a bicontinuous cubic phase and then a L_α phase.

$Gem_{20}E_{10}$ forms a L_α phase at room temperature and a L_3 (sponge phase) at 32°C. Both these phases are constructed from bilayers, suggesting lower curvature than $Gem_{20}E_{15}$, as expected.

7.3 Final Remarks

This work is the first direct comparison of gemini surfactants to the industrially and academically important[7,71] alkyl polyoxyethylene surfactants.

The CMCs were lower than conventional surfactants, although the decrease is smaller than expected, becoming less noticeable as the tail length is increased.

The micelle morphologies and phase behaviour agree quantitatively with the behaviour of conventional nonionic surfactants. Two noticeable exceptions are the onset of viscoelasticity in $Gem_{20}E_{15}$ when heated towards its cloud point (which is previously unreported for nonionic surfactants), and the formation of the intermediate phase in the place of the L_α phase in $Gem_{20}E_{20}$, which is also previously unreported.

References

(1) Rosen, M. J. *CHEMTECH* 1993, 30.

(2) Menger, F. M.; Littau, C. A. *J. Am. Oil Chem. Soc.* 1993, *115*, 10083.

(3) Rosen, M. J.; Tracy, D. J. *Journal of Surfactants and Detergents* 1998, *1*, 547.

(4) Menger, F. M.; Keiper, J. S. *Angew. Chem. Int. Ed.* 2000, *39*, 1906.

(5) Mukerjee, P.; Mysels, K. J. *Critical Micelle Concentrations of Aqueous Surfactant Systems*, 1971.

(6) Tanford, C. *The Hydrophobic Effect*; 2nd ed.; Wiley: New York, 1980.

(7) Schick, M. J. In *Nonionic Surfactants*; Schick, M. J., Ed.; Marcel Dekker: New York, 1967.

(8) Zana, R. *Langmuir* 1996, *12*, 1208.

(9) Rosen, M. J.; Zhu, Z. H.; Gao, T. *J. Colloid Interface Sci.* 1993, *157*, 254.

(10) Rosen, M. J.; Gao, T.; Nakatsuji, Y.; Masuyama, A. *Colloids and Surfaces A: Physicochemical and Engineering Aspects* 1994, *88*, 1.

(11) Liu, L.; Rosen, M. J. *J. Colloid Interface Sci.* 1996, *179*, 454.

(12) Zana, R.; Lévy, H.; K, K. *J. Colloid Interface Sci.* 1998, *197*, 370.

(13) Alargova, R. G.; Kochijashky, I. I.; Sierra, M. L.; Kwetkat, K.; Zana, R. *J. Colloid Interface Sci.* 2001, *235*, 119.

(14) Zhu, Y.-p.; Masuyama, A.; Okahara, M. *J. Am. Oil Chem. Soc.* 1990, *67*, 459.

(15) Zhu, Y.-p.; Masuyama, A.; Kirito, Y.-i.; Okahara, M.; Rosen, M. J. *J. Am. Oil Chem. Soc.* 1992, *69*, 626.

(16) Zhu, Y.-p.; Masuyama, A.; Kobata, Y.; Nakatsuji, Y.; Okahara, M.; Rosen, M. J. *J. Colloid Interface Sci.* 1993, *158*, 40.

(17) Zhu, Y.-p.; Masuyama, A.; Okahara, M. *J. Am. Oil Chem. Soc.* 1991, *68*, 268.

(18) Menger, F. M.; Littau, C. A. *J. Am. Oil Chem. Soc.* 1991, *113*, 1451.

(19) Devínsky, F.; Lacko, I.; Bittererová, F.; Tomecková, L. *J. Colloid Interface Sci.* 1986, *114*, 314.

(20) Zana, R.; Benrraou, M.; Rueff, R. *Langmuir* 1991, *7*, 1072.

(21) Rosen, M. J.; Liu, L. *J. Am. Oil Chem. Soc.* 1996, *73*, 885.

(22) Menger, F. M.; Keiper, J. S.; Azov, V. *Langmuir* 2000, *16*, 2062.

(23) Tsubone, K.; Nishio, H.; Kusumaru, M. 1996, JP 08291040 "Cosmetics containing fatty amide nonionic surfactants"

(24) Medina, S. W. 1997, US 5650543 "Ethoxylated acetylenic glycols having low dynamic surface tension"

(25) Tracy, D. J.; Li, R.; Dahanayake, M. S.; Yang, J. 1998, US 5811384 "Nonionic gemini surfactants"

(26) Tracy, D. J.; Li, R.; Yang, J. 1998, US 5846926 "Nonionic gemini surfactants of aromatic compounds having three hydrophilic heads and two lipophilic tails"

(27) Tracy, D. J.; Li, R. 1999, US 5900397 "Nonylphenol nonionic gemini surfactants"

(28) Lassila, K. R.; Uhrin, P. A. 2001, US 6313182 "Acetylenic diol ethylene oxide/propylene oxide adducts and processes for their manufacture"

(29) Renouf, P.; Mioskowski, C.; Lebeau, L.; Hebrault, D.; Desmurs, J.-R. *Tetrahedron Lett.* 1998, *39*, 135.

(30) Song, L. D.; Rosen, M. J. *Langmuir* 1996, *12*, 1149.

(31) van Os, N. M.; Haak, J. R.; Rupert, L. A. M. *Physico-Chemical Properties of Selected Anionic, Cationic and Nonionic Surfactants*; Elsevier Science: Amsterdam, 1993.

(32) Rösch, M. In *Nonionic Surfactants*; Schick, M. J., Ed.; Marcel Dekker: New York, 1967.
(33) Eastoe, J.; Rogueda, P.; Harrison, B. J.; Howe, A. M.; Pitt, A. R. *Langmuir* 1994, *10*, 4429.
(34) Eastoe, J.; Rogueda, P.; Howe, A. M.; Pitt, A. R.; Heenan, R. K. *Langmuir* 1996, *12*, 2701.
(35) Briggs, C. B. A.; Newington, I. M.; Pitt, A. R. *J. Chem. Soc., Chem. Commun.* 1995, 379.
(36) Castro, M. J. L.; Kovensky, J.; Cirelli, A. F. *Tetrahedron Lett.* 1997, *38*, 3995.
(37) Castro, M. J. L.; Kovensky, J.; Cirelli, A. F. *Tetrahedron* 1999, *55*, 12711.
(38) Chierici, S.; Marronbrignone, P. B. L.; Morelis, R. M.; Coulet, P. R. *Chem. Phys. Lipids* 1997, *87*, 91.
(39) Pestman, J. M.; Terpstra, R.; Stuart, M. C. A.; van Doren, H. A.; Brisson, A.; Kellogg, R. M.; Engberts, J. B. F. N. *Langmuir* 1997, *13*, 6857.
(40) Shibata, A.; Kamiyama, H.; Kuraishi, T.; Kukita, K.; Katori, T. 1986, JP 61130298 "6,6'-Bis(acylamino)-6,6'-dideoxy-x,x'-trehalose analogs as antitumour agents"
(41) Connor, D. S.; Fu, Y. C.; Scheibel, J. J. 1996, US 5512699 "Amides of fatty acids and polyhydroxy amines for use as surfactants"
(42) Wong, S.-m. 1997, US 5622938 "Sugar base surfactant for nanocrystals"
(43) Tracy, D. J.; Li, R.; Yang, J. 1998, WO 9845308 "Manufacture of nonionic gemini surfactants having two hydrophilic sugar groups linked by a bridge"
(44) Camilleri, P.; Engberts, J. B. F. N.; Fielden, M. L.; Kremer, A. 2000, WO 0076954 "Carbohydrate-based polyhydroxy diamine surfactants for gene transfer"
(45) Tracy, D. J.; Li, R.; Yang, J. 1999, US 5863886 "Nonionic gemini surfactants having multiple hydrophobic and hydrophilic sugar groups and their use in cleaning"
(46) Scheibel, J. J.; Connor, D. S.; Fu, Y. C. 1996, US 5534197 "Gemini polyhydroxy fatty acid amide surfactants for detergents and personal care compositions"
(47) Adams, K. E.; Newington, I. M.; Pitt, A. R. 1995, EP 688781 "Nonionic surfactants containing amino and polysaccharide groups, especially for use in photographic emulsions"
(48) Tracy, D. J.; Ruoxin, L. 1998, WO 9823365 "Nonionic gemini surfactants and their blends"
(49) Tracy, D. J.; Li, R. 1998, WO 9837062 "Manufacture of novel nonionic alkylphenol gemini surfactants"
(50) Tracy, D. J.; Li, R.; Dahanayake, M. S.; Yang, J. 1999, US 5945393 "Nonionic gemini surfactants"
(51) Tracy, D. J.; Li, R.; Dahanayake, M. S.; Yang, J. 2001, US 6204297 "Nonionic gemini surfactants"
(52) Paddon-Jones, G.; Regismond, S.; Kwetkat, K.; Zana, R. *J. Colloid Interface Sci.* 2001, *243*, 496.
(53) Schachat, N.; Greenwald, H. L. In *Nonionic Surfactants*; Schick, M. J., Ed.; Marcel Dekker: New York, 1967.
(54) Israelachvili, J. N.; Mitchell, J. D.; Ninham, B. W. *Faraday Trans. II* 1976, *72*, 1525.
(55) Tanford, C. In *The Hydrophobic Effect*; 2nd ed.; Wiley: New York, 1980.

(56) Rosen, M. J.; Cohen, A. W.; Dahanayake, M.; Hua, X.-y. *J. Phys. Chem.* 1982, *86*, 541.
(57) Elworthy, P. H.; Mac Pharlane, C. B. *J Pharm. Pharmacol. Suppl.* 1962, *14*, 100.
(58) Bailey Jr, F. E.; Koleske, J. V. In *Nonionic Surfactants*; Schick, M. J., Ed.; Marcel Dekker: New York, 1967, pp 794.
(59) Goates, J. R.; Ott, J. B. *Chemical Thermodynamics*; Hardcourt Brace Jovanovich: New York, 1971.
(60) Hartley, G. S. *Aqueous Solutions of Paraffin Chain Salts*; Hermann & Cie.: Paris, 1936.
(61) Murray, R. C.; Hartley, G. S. *Trans. Farraday Soc.* 1935, *31*, 183.
(62) Vold, M. J. *J. Colloid Sci.* 1950, *5*, 506.
(63) Phillips, J. N. *Trans. Farraday Soc.* 1955, *51*, 561.
(64) Corkill, J. M.; Goodman, J. F.; Harrold, S. P. *Trans. Farraday Soc.* 1964, *60*, 202.
(65) Stainsby, G.; Alexander, A. E. *Trans. Farraday Soc.* 1950, *46*, 587.
(66) Matijevic, E.; Pethica, B. A. *Trans. Farraday Soc.* 1958, *54*, 587.
(67) Shinoda, K.; Hutchinson, E. *J. Phys. Chem.* 1962, *66*, 577.
(68) Clint, J. *J. Chem. Soc.* 1975, *71*, 1327.
(69) Laughlin, R. G. *The Aqueous Phase Behaviour of Surfactants*; Academic Press: London, 1994.
(70) Becher, P. In *Nonionic Surfactants*; Schick, M. J., Ed.; Marcel Dekker: New York, 1967.
(71) Mitchell, J. D.; Tiddy, G. J. T.; Waring, L.; Bostock, T.; McDonald, M. P. *Faraday Trans. II* 1983, *79*, 975.
(72) Balmbra, R. R.; Clunie, J. S.; Corkill, J. M.; Goodman, J. F. *Trans. Farraday Soc.* 1962, *58*, 1661.
(73) Hyde, S. T. In *Handbook of Applied Surface and Colloid Chemistry*; Holmberg, K., Ed.; John Wiley & Sons: New York, 2001.
(74) Fontell, K. *Colloid and Polym. Sci.* 1990, *268*, 264.
(75) Lindman, B.; Wennerström, H. In *Topics in Current Chemistry*; Springer: Berlin, 1980; Vol. 87.
(76) Hunter, R. J. *Foundations of Colloid Science, pg 435*; 2nd ed.; Oxford University Press: Oxford, 2001.
(77) Lindman, B.; Brun, B. *J. Colloid Interface Sci.* 1973, *42*, 388.
(78) Hiemenz, P. C. *Principles of Colloid and Surface Chemistry*; Marcel Dekker Inc.: New York, 1977.
(79) Kalyanasundaram, K.; Thomas, J. K. *J. Am. Chem. Soc.* 1997, *99*, 2039.
(80) Schwarz, F. P. *J Chem. Eng. Data* 1977, *22*, 273.
(81) Almgren, M.; Grieser, F.; Thomas, K. *J. Am. Chem. Soc.* 1979, *101*, 279.
(82) Ananthapadmanabhan, K. P.; Goddard, E. D.; Turro, N. J.; Kuo, P. L. *Langmuir* 1985, *1*, 352.
(83) Lindner, P.; Zemb, T. N. *Neutron, X-Ray and Light Scattering: Introduction to an Investigative Tool for Colloid and Polymeric Systems*; North-Holland: Amsterdam, 1991.
(84) Guinier, A.; Fournet, G. *Small-Angle Scattering of X-Rays*; John Wiley and Sons: New York, 1955.
(85) Kostorz, G. *Treatise on Materials Science and Technology*; Academic Press: New York, 1979; Vol. 15.
(86) Glatter, O.; Kratky, O. *Small Angle X-ray Scattering* New York, 1982.

(87) Hayter, J. B. In *Physics of Amphiphiles: Micelles, Vesicles, and Microemulsions*; Degiorgio, V., Corti, M., Eds.; Elsevier Science: New York, 1983, pp 59.

(88) Kostorz, G.; Lovesey, S. W. In *Treatise on Materials Science and Technology*; Kostorz, G., Ed.; Academic Press: New York, 1979.

(89) Sears, V. F. *Neutron News* 1992, *2*, 26.

(90) Rayleigh, L. *Proc. Roy. Soc. (London)* 1914, *A90*, 219.

(91) Schulz, G. V. *Z. Phys. Chem.* 1935, *43*, 25.

(92) Choi, S. "SANS Experimental Methods," National Institute of Standards and Technology, 2000.

(93) Rosevear, F. B. *J. Am. Oil Chem. Soc.* 1954, *31*, 628.

(94) Laughlin, R. G.; Munyon, R. L. *J. Phys. Chem.* 1987, *91*, 3299.

(95) Laughlin, R. G.; Lynch, M. L.; Marcott, C.; Munyon, R. L.; Marrer, A. M.; Kochvar, K. A. *J. Phys. Chem. B* 2000, *104*, 7354.

(96) Herzburg, G. In *Infrared and Raman Specta*; Van Nostrand Reindhold: New York, 1945.

(97) Buckingham, S. A.; Garvey, C. J.; Warr, G. G. *J. Phys. Chem.* 1993, *97*, 10236.

(98) McGary, C. W. *Journal of Polymer Science* 1960, *46*, 54.

(99) Desbène, P. L.; Portet, F. I.; Goussot, G. J. *Journal of Chromatography A* 1996, *730*, 209.

(100) McAuliffe, C. *J. Phys. Chem.* 1966, *70*, 1267.

(101) Herman, R. B. *J. Phys. Chem.* 1972, *76*, 2754.

(102) Reynolds, J. A.; Gilbert, D. B.; Tanford, C. *Proc. Nat. Acad. Sci. U.S.A.* 1974, *71*, 2925.

(103) Mukerjee, P. *Adv. Colloid Interface Sci.* 1967, *1*, 242.

(104) Zana, R. *J. Colloid Interface Sci.* 2002, *246*, 182.

(105) Hayter, J. B.; Zulauf, M. *Colloid and Polymer Science* 1982, *260*, 1023.

(106) Magid, L. J.; Triolo, R.; Johnson Jr, J. S. *J. Phys. Chem.* 1984, *88*, 5730.

(107) Triolo, R.; Magid, L. J.; Johnson Jr, J. S.; Child, H. R. *J. Phys. Chem.* 1982, *86*, 3689.

(108) Bernheim-Groswasser, A.; Tlusty, T.; Safran, S. A.; Talmon, Y. *Langmuir* 1999, *15*, 5448.

(109) Tlusty, T.; Safran, S. A.; Menes, R.; Strey, R. *Physical Review Letters* 1997, *78*, 2616.

(110) Lum Wan, J. A.; Warr, G. G.; White, L. R.; Grieser, F. *Colloid and Polymer Science* 1987, *265*, 528.

(111) de Gennes, P.-G. *Scalling Concenpts in Polymer Physics*; Cornell University Press: Ithaca, 1979.

(112) Cotton, J. P. In *Neutron, X-Ray and Light Scattering: Introduction to an Investigative Tool for Colloid and Polymeric Systems*; Lindner, P., Zemb, T. N., Eds.; North-Holland: Amsterdam, 1991.

(113) Zimm, B. H. *J. Chem. Phys.* 1948, *16*, 1093.

(114) Porod, G. In *Small Angle X-ray Scattering*; Glatter, O., Kratky, O., Eds.: New York, 1982.

(115) Glatter, O.; Fritz, G.; Lindner, H.; Brunner-Popela, J.; Mittelbach, R.; Strey, R.; Egelhaaf, S. U. *Langmuir* 2000, *16*, 8692.

(116) Percus, J. K.; Yevick, G. J. *Phys. Rev.* 1958, *110*, 1.

(117) Hayter, J. B.; Penfold, J. *Molecular Physics* 1981, *42*, 109.

(118) Einstein, A. *Investigations on the Theory of the Brownian Movement*; Dover Publications: New York, 1956.

(119) Davey, T., Personal Com.

(120) Rehage, H.; Hoffmann, H. *Faraday Discuss. Chem. Soc.* 1983, *76*, 363.

(121) Balmbra, R. R.; Clunie, J. S.; Corkill, J. M.; Goodman, J. F. *Trans. Faraday Soc.* 1962, *58*, 1661.

(122) Nakagawa, T. In *Nonionic Surfactants*; Schick, M. J., Ed.; Marcel Dekker: New York, 1967.

(123) Zulauf, M.; Rosenbusch, J. P. *J. Phys. Chem.* 1983, *87*, 856.

(124) Zulauf, M.; Weckström, K.; Hayter, J. B.; Degiorgio, V.; Corti, M. *J. Phys. Chem.* 1985, *89*, 3411.

(125) Brunner-Popela, J.; Glatter, O. *J. Appl. Crystallogr.* 1997, *30*, 431.

(126) Weyerich, B.; Brunner-Popela, J.; Glatter, O. *J. Appl. Crystallogr.* 1999, *32*, 197.

(127) Hoover, W. G.; Ree, F. H. *J. Chem. Phys.* 1968, *19*, 3609.

(128) Bernheim-Groswasser, A.; Wachtel, E.; Talmon, Y. *Langmuir* 2000, *16*, 4131.

(129) Lang, J. C.; Morgan, R. G. *J. Chem. Phys.* 1980, *73*, 5849.

(130) Porte, G.; Marignan, J.; Bassereau, P.; May, R. *J. Phys. (France)* 1988, *49*, 511.

(131) Porte, G.; Appell, J.; Bassereau, P.; Marignan, J. *J. Phys. (France)* 1989, *50*, 1335.

(132) Strey, R.; Schomäcker, R.; Roux, D.; Nallet, F.; Olsson, U. *Faraday Trans.* 1990, *86*, 2253.

(133) Yamamoto, J.; Tanaka, H. *Physical Review Letters* 1996, *77*, 4390.

(134) Funari, S. S.; Holmes, M. C.; Tiddy, G. J. T. *J. Phys. Chem.* 1994, *98*, 3015.

(135) Fairhurst, C. E.; Holmes, M. C.; Leaver, M. S. *Langmuir* 1997, *13*, 4964.

(136) Funari, S. S.; Holmes, M. C.; Tiddy, G. J. T. *J. Phys. Chem.* 1992, *96*, 11029.

(137) Burgoyne, J.; Holmes, M. C.; Tiddy, G. J. T. *J. Phys. Chem.* 1995, *99*, 6054.

(138) Fairhurst, C. E.; Holmes, M. C.; Leaver, M. S. *Langmuir* 1996, *12*, 6336.

(139) Holmes, M. C.; Charvolin, J. *J. Phys. Chem.* 1984, *88*, 810.

(140) Luzzati, V.; Tardieu, A.; Gulik-Krywicki, T. *Nature* 1968, *217*, 1028.

(141) Kékicheff, P.; Tiddy, G. J. D. *J. Phys. Chem.* 1989, *93*, 2520.

(142) Porod, G. *Kolloid-Z.* 1951, *124*, 83.

(143) Porod, G. *Kolloid-Z.* 1952, *125*, 51.

(144) *CRC Handbook of Chemistry and Physics*; CRC Press: Cleveland, Ohio, 1977-.

Appendix

A.1 Synthesis for Nonionic Gemini Surfactants (Gem_nE_m)

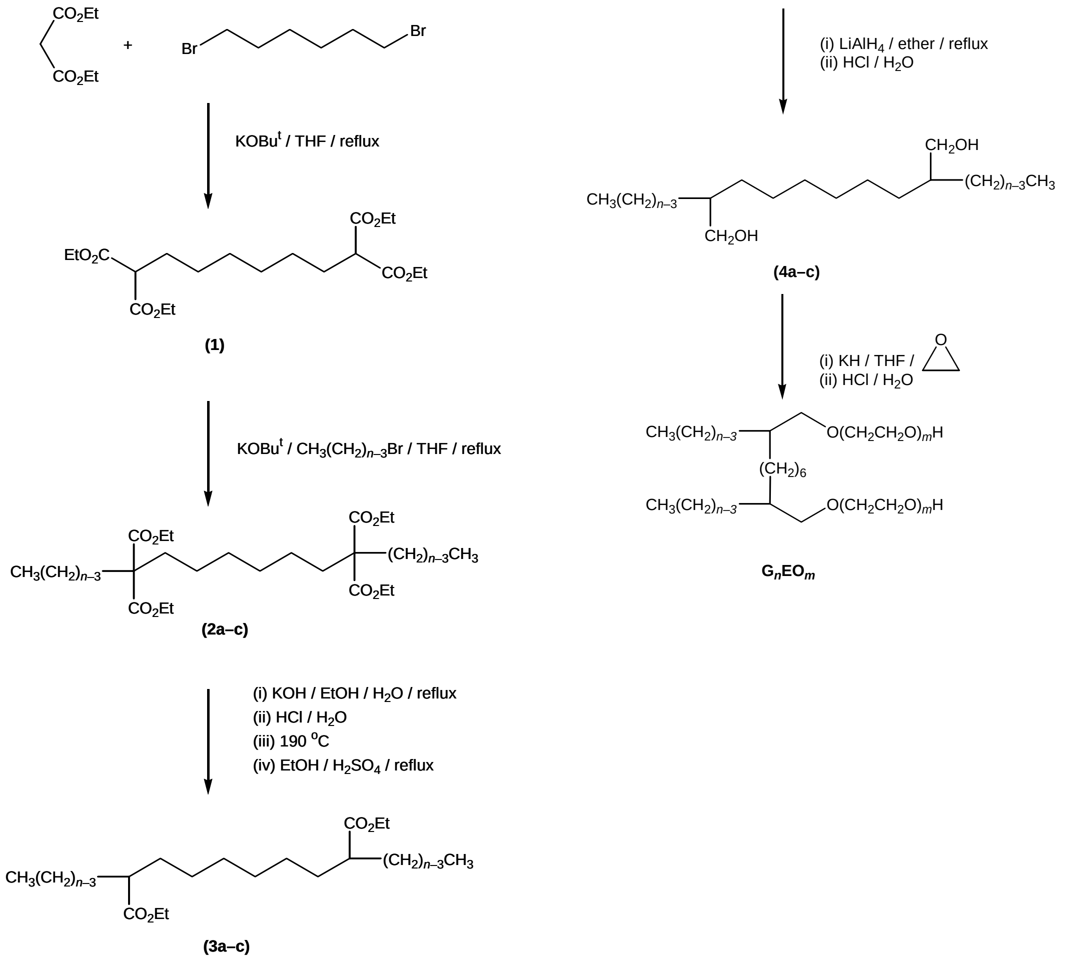

A.2 The Classical Chemical Potential

The chemical potential for a surfactant in solution is given by:[6]

$$\mu_i = \mu_i^{\mathrm{o}} + RT \ln x_i + RT \ln \gamma_i$$

where μ_i^{o} is the standard chemical potential, R is the ideal gas constant, x_i is the concentration of solute in solution and γ_i is called the *activity coefficient*. The standard chemical potential (μ_i^{o}) includes all interactions between the solute and the solution as well as the solute internal energy. All solute-solute interactions are accounted for in $RT\ln\gamma_i$, which can often be set equal to zero at low concentrations, or more precisely as the solute concentration approaches infinite dilution. $RT\ln x_i$ is a purely statistical term arising from the entropy of mixing solute and solvent. The great advantage of using mole fraction units is that all of the entropy is accounted for in this term and the standard chemical potential contains *only* the solute-solvent free energy and the solute internal free energy.

A.3 Examples of Microscopic Textures for H_1 and L_α Phases

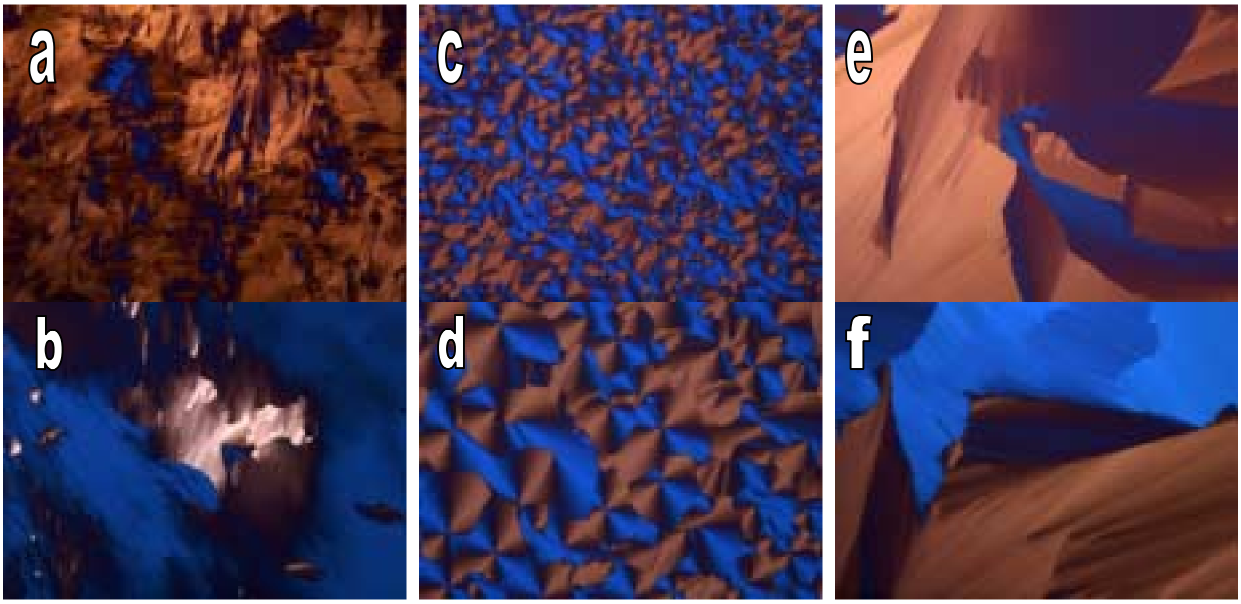

Figure A.2: Examples of microscopic textures of the H_1 phase. a and b has a striated texture in several different domains. c and d has a fan like texture. e and f has a more disordered fan like texture. Note that all of these textures are from the same $C_{12}E_8$ surfactant. Many textures can be produced for the same surfactant dependent on the preparation of the sample. Magnifications are a) x 50, b) x 100, c) x 200, d) x 200, e) x 200 and f) x 100.

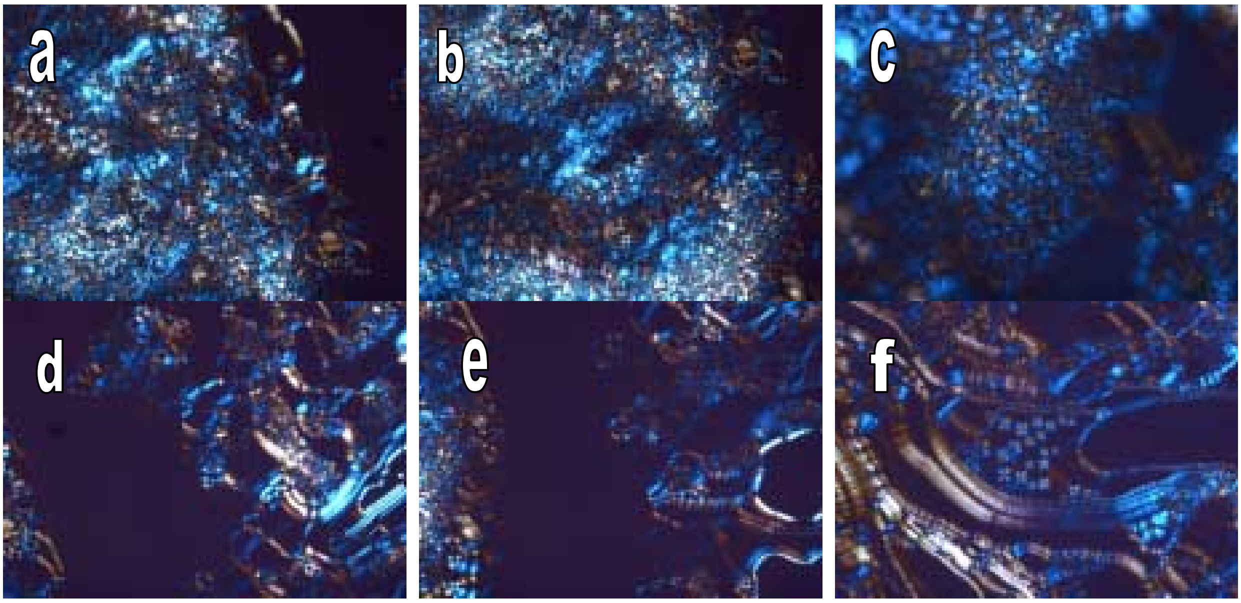

Figure A.3: Examples of microscopic textures of the L_α phase. a-c show a very fine mosaic texture. d-f show a "oily-streak" texture. The dark areas of the images are caused by the lamellar sheets of the La phase aligning with microscope cover slip. In this orientation the phase can not be identified. Great care must be taken when identifying La phases because of this affect. Note the spheres with crosses in the centre of f. These are caused by scattering from multi-lamellar vesicles and are a clear sign of a lamellar phase. All images where collected from $C_{12}E_3$. Magnifications are a) x 50, b) x 50, c) x 200, d) x 50, e) x 50 and f) x 100.

A.4 Operation of Capillary Viscometer

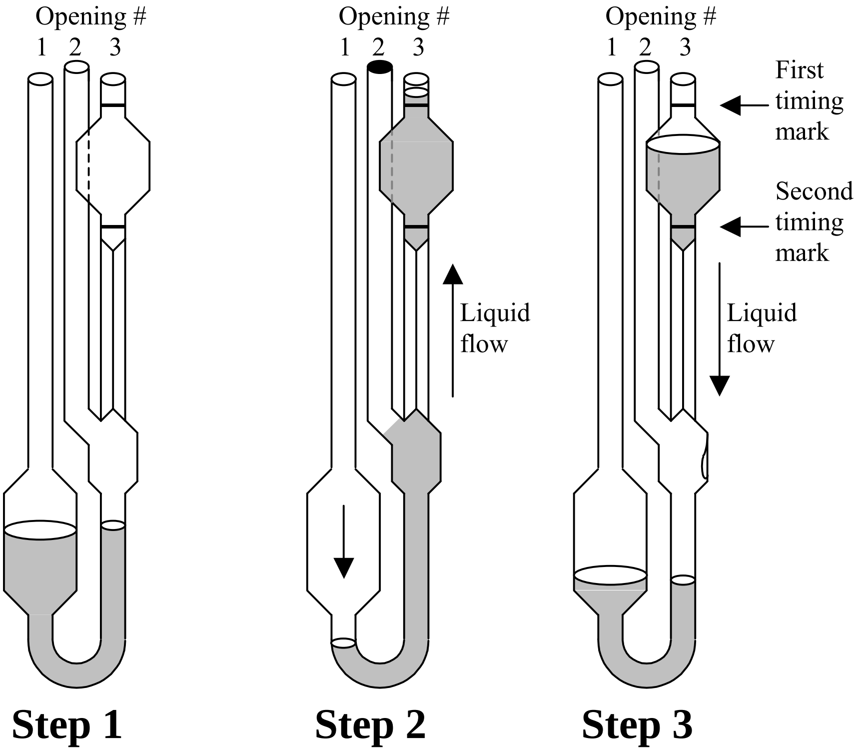

Figure A.4: The operation of a capillary viscometer:

***Step 1*: The viscometer reserve is filled with approximately 15 ml of solution**

***Step 2*: Opening #2 is stoppered and air is pumped down opening #1 to force solution through the capillary and into the bulb above it**

***Step 3*: The pressure is removed from opening #1 and then opening #2 is quickly unstoppered. The solution is allowed to flow through the capillary under the force of gravity and the flow time is recorded as the solution bulb empties from the first timing mark to the second timing mark. The flow time is related to the viscosity as mentioned in the text.**

A.5 Difference Between R = 4.5/Q_{min} and $R_{micelle}$ for Core-Shell Micelles

The scattering function for a core-shell sphere is (see Equation 3.5)

$$I(Q) = \frac{N_{\mathrm{P}}}{V_{\mathrm{tot}}} F^2(Q)$$

where:

$$\begin{aligned} F(Q) &= F_{\mathrm{core}}(Q) + F_{\mathrm{shell}}(Q) \\ &= \frac{3V_{\mathrm{core}}(\rho_{\mathrm{core}} - \rho_{\mathrm{shell}})\,\mathrm{j}_1(QR_{\mathrm{core}})}{QR_{\mathrm{core}}} \\ &\quad + \frac{3V_{\mathrm{micelle}}(\rho_{\mathrm{shell}} - \rho_{\mathrm{solv}})\,\mathrm{j}_1(QR_{\mathrm{micelle}})}{QR_{\mathrm{micelle}}} \end{aligned} \qquad \text{A.1}$$

If ρ_{core} = 6.38 x 10^{-6} Å^{-2} (i.e. pure hydrocarbon), ρ_{solv} = -0.30 x 10^{-6} Å^{-2} (i.e. pure D_2O) and ρ_{shell} = 3.4 x 10^{-6} Å^{-2} (i.e. the maximum expected hydration number of 2D_2O per EO) then the percentage difference between R = 4.5/Q_{min} and the actual radius of a spherical core-shell micelle can be calculated by solving for the first minimum in Equation A.1. This is shown in Figure A.5 as a function of shell thickness divided by the core radius. The maximum difference is about 19.2% when the shell thickness is 80% the radius of the core radius.

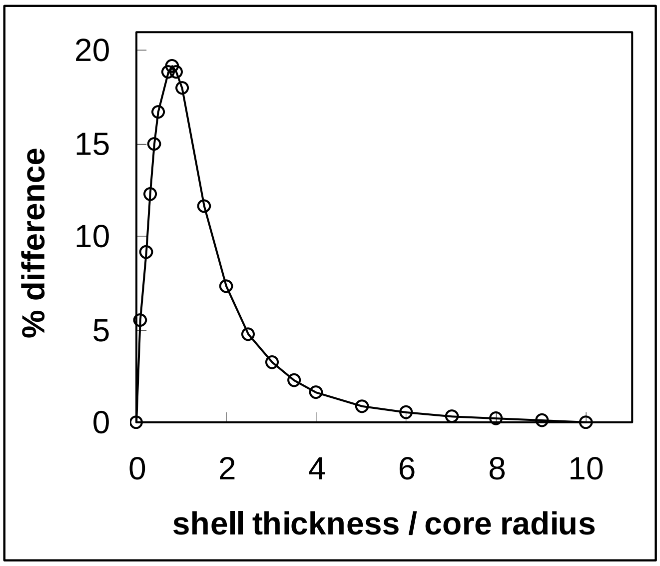

Figure A.5: % difference between R = 4.5/Q_{min} and the actual radius of a spherical core-shell micelle when ρ_{shell} = 3.4 x 10^{-6} Å^{-2} (i.e. 2 x D_2O per EO). The maximum difference is ~19% when the shell is ~80% the thickness of the core.

A.6 R_{sphere} Calculated from R_G for Core-Shell Micelles

The micelle geometry and scattering length density profile determine R_G. For the idealised case of a spherical micelle with a single, uniform, scattering length density R_G is uniquely determined by the micelle radius (R_{sphere}):

$$R_G = \sqrt{\tfrac{3}{5}} R_{\text{sphere}} \qquad \text{A.2}$$

For a core-shell sphere R_G is given by (see below):

$$R_G^2 = \frac{3}{5}\frac{(\rho_{\text{core}} - \rho_{\text{shell}})R_{\text{core}}^5 + (\rho_{\text{shell}} - \rho_{\text{solv}})R_{\text{tot}}^5}{(\rho_{\text{core}} - \rho_{\text{shell}})R_{\text{core}}^3 + (\rho_{\text{shell}} - \rho_{\text{solv}})R_{\text{tot}}^3} \qquad \text{A.3}$$

where ρ_{core}, ρ_{shell} and ρ_{solv} are the scattering length densities of the core, the shell and the solvent respectively, and R_{core} and R_{tot} are the radius of the core and the total micelle respectively.

The first equation is clearly much easier to solve than the second equation and does not require knowledge of the scattering length densities. The % difference between the actual micelle radius and the radius of a uniform sphere with the same R_G is plotted in Figure A.6 as a function of shell thickness over core radius. This assumes the same scattering length densities values used in Section A.5.

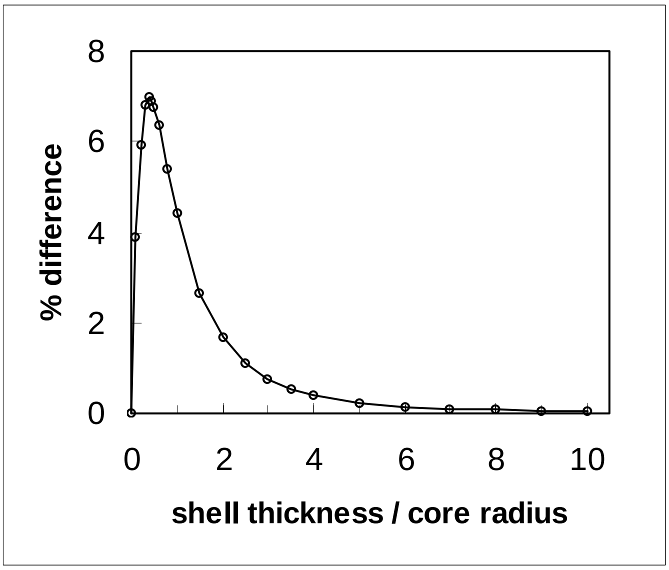

Figure A.6: % difference between the total micelle radius of a core-shell sphere with $\rho_{\text{shell}} = 3.4 \times 10^{-6}$ Å^{-2} (i.e. 2 x D_2O per EO) and the radius of a uniform sphere with the same R_G. The maximum difference is ~7% when the shell is ~40% the thickness of the core.

Equation A.3 is derived from the definition of R_G as follows:

$$R_{\mathrm{G}}^{2}=\frac{\int_{0}^{\infty}\rho(r)r^{4}dr}{\int_{0}^{\infty}\rho(r)r^{2}dr}$$

$$R_{\mathrm{G}}^{2}=\frac{\left(\rho_{\mathrm{core}}-\rho_{\mathrm{shell}}\right)\int_{0}^{R_{\mathrm{core}}}r^{4}dr+\left(\rho_{\mathrm{shell}}-\rho_{\mathrm{solv}}\right)\int_{0}^{R_{\mathrm{tot}}}r^{4}dr}{\left(\rho_{\mathrm{core}}-\rho_{\mathrm{shell}}\right)\int_{0}^{R_{\mathrm{core}}}r^{2}dr+\left(\rho_{\mathrm{shell}}-\rho_{\mathrm{solv}}\right)\int_{0}^{R_{\mathrm{tot}}}r^{2}dr}$$

$$R_{\mathrm{G}}^{2}=\frac{\left(\rho_{\mathrm{core}}-\rho_{\mathrm{shell}}\right)\frac{R_{\mathrm{core}}^{5}}{5}+\left(\rho_{\mathrm{shell}}-\rho_{\mathrm{solv}}\right)\frac{R_{\mathrm{tot}}^{5}}{5}}{\left(\rho_{\mathrm{core}}-\rho_{\mathrm{shell}}\right)\frac{R_{\mathrm{core}}^{3}}{3}+\left(\rho_{\mathrm{shell}}-\rho_{\mathrm{solv}}\right)\frac{R_{\mathrm{tot}}^{3}}{5}}$$

giving:

$$R_{\mathrm{G}}^{2}=\frac{3}{5}\frac{\left(\rho_{\mathrm{core}}-\rho_{\mathrm{shell}}\right)R_{\mathrm{core}}^{5}+\left(\rho_{\mathrm{shell}}-\rho_{\mathrm{solv}}\right)R_{\mathrm{tot}}^{5}}{\left(\rho_{\mathrm{core}}-\rho_{\mathrm{shell}}\right)R_{\mathrm{core}}^{3}+\left(\rho_{\mathrm{shell}}-\rho_{\mathrm{solv}}\right)R_{\mathrm{tot}}^{3}}$$

A.7 Background Subtraction from SANS data

The reduced experimental scattering can be written as:

$$I_{\text{exp}}(Q) = I(Q) + \text{bkg}$$

where $I_{\text{exp}}(Q)$ is the experimental scattering with the background to be subtracted, $I(Q)$ is the corrected scattering and bkg is the background. The Porod law states that $I(Q)$ scatters as a constant times Q^{-4} giving:[142,143]

$$I_{\text{exp}}(Q) = AQ^{-4} + \text{bkg}$$

where A is a constant. Multiplying both sides by Q^4 gives:

$$Q^4 I_{\text{exp}}(Q) = A + \text{bkg}Q^4$$

If there is no background then a plot of $Q^4I_{\text{exp}}(Q)$ vs Q will level off at a constant value (A) in the region where the Porod limit is applicable. If there is a background then this curve will rapidly increase due to the Q^4 dependence attached to bkg. This is a very sensitive way to determine if there is even a small background superimposed on the scattering data. This is shown in Figure A.7a for $\text{Gem}_{12}\text{E}_{10}$. The corrected data (open circles) increases up to a maximum, then decreases and then begins to oscillate about the constant value A. The uncorrected data (solid circles) increases up to a local maxima, begins to turn down and then increases rapidly due to the Q^4 term in the above expression.

The background is calculated by plotting $Q^4I_{\text{exp}}(Q)$ vs Q^4. From the above expression the slope is equal to the background, as shown in Figure A.7b. The background values are given in Table A.1.

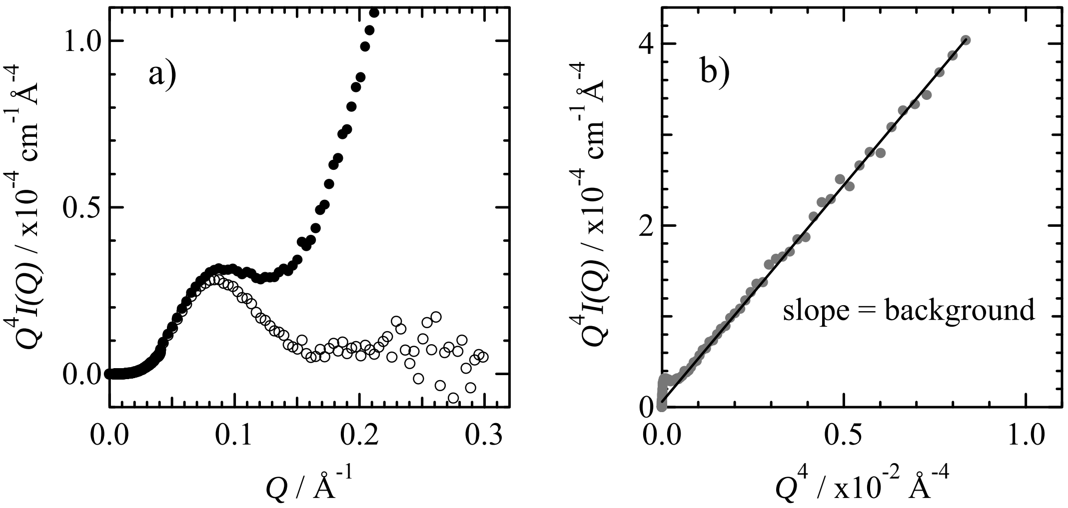

Figure A.7: a) Plot of $Q^4I(Q)$ vs Q for the uncorrected scattering of $\mathrm{Gem_{12}E_{10}}$ (solid circles) and the corrected scattering (open circles). b) Plot of $Q^4I(Q)$ vs Q^4 for the same data. The slope of the line gives the scattering background.

Surfactant	1 wt%	2 wt%	5 wt%	10 wt%
$\mathrm{Gem_{12}E_{10}}$	0.047	—	—	—
$\mathrm{Gem_{12}E_{15}}$	0.048	—	—	—
$\mathrm{Gem_{14}E_{10}}$	0.051	—	—	—
$\mathrm{Gem_{14}E_{15}}$	0.048	—	—	—
$\mathrm{Gem_{20}E_{15}}$	0.054	0.0609	0.0793	0.138
$\mathrm{Gem_{20}E_{20}}$	0.053	—	0.0859	—
$\mathrm{Gem_{20}E_{30}}$	0.052	—	0.0922	—

Table A.1: Experimental backgrounds from Porod plots for the gemini surfactant SANS data at 25°C.

A.8 Radius of Gyration Calculations for Gemini Surfactants

Surfactant	R_G	Plot type	slope	intercept	Q Range
$Gem_{12}E_{10}$	69 ± 5	Zimm	200.95	0.1262	0.009 – 0.015
$Gem_{12}E_{15}$	27 ± 3	Guinier	236.18	—	0.009 – 0.03
$Gem_{14}E_{10}$	208 ± 20	Zimm	308.39	0.0213	0.004 – 0.01
$Gem_{14}E_{15}$	26 ± 6	Guinier	225.74	—	0.009 – 0.03
$Gem_{20}E_{15}$	80 ± 50	Zimm	119.94	0.0565	0.009 – 0.014
$Gem_{20}E_{20}$	38 ± 3	Guinier	468.92	—	0.004 – 0.03
$Gem_{20}E_{30}$	54 ± 5	Guinier	969.89	—	0.004 – 0.02

Table A.2: Radius of gyration calculations for 1wt% gemini surfactants at 25°C using either the Guinier or Zimm approximation.

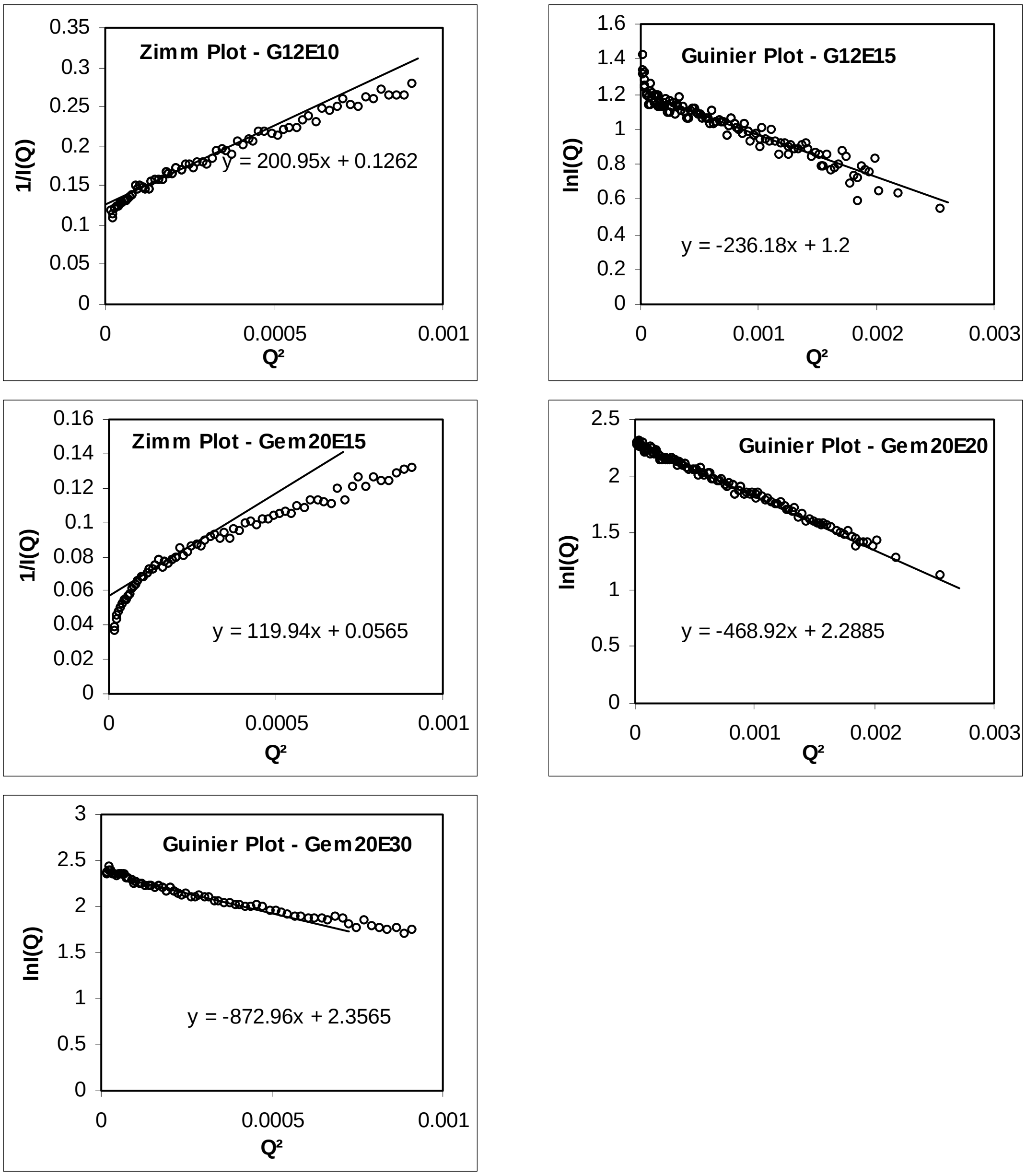

Figure A.8: Slopes for calculating the radius of gyration using either the Guinier or Zimm plots. Note the poor fit for Gem$_{20}$E$_{15}$, which gives rise to a large error for R_G (i.e. 80 ± 50 Å). This is probably due to interparticle interactions at very low Q.

A.9 Mean Chord Length Calculations for 1wt% Gemini Surfactants

Surfactant	$\langle l \rangle$	**invariant (q^*)**	$q^*\langle l \rangle/\pi$
$\mathrm{Gem_{12}E_{10}}$	61.3 ± 3.2	4.03 ± 0.19	0.79 ± 0.02
$\mathrm{Gem_{12}E_{15}}$	54.0 ± 2.9	3.95 ± 0.18	0.68 ± 0.02
$\mathrm{Gem_{14}E_{10}}$	74.3 ± 3.2	5.30 ± 0.21	1.25 ± 0.02
$\mathrm{Gem_{14}E_{15}}$	57.3 ± 3.0	4.04 ± 0.19	0.74 ± 0.02
$\mathrm{Gem_{20}E_{15}}$	72.6 ± 2.7	6.08 ± 0.20	1.41 ± 0.02
$\mathrm{Gem_{20}E_{20}}$	71.4 ± 3.1	4.91 ± 0.19	1.12 ± 0.02
$\mathrm{Gem_{20}E_{30}}$	75.4 ± 3.5	3.86 ± 0.16	0.93 ± 0.02

Table A.3: Mean chord length for 1wt% gemini surfactants at 25°C calculated by dividing column 3 by the invariant in column 2.

A.10 Data Fitting of 1wt% Gemini Surfactants at 25°C

The scattering from core-shell spheres is given by:

$$I_{\text{sphere}}(Q) = \frac{N_{\text{P}}}{V_{\text{tot}}} F^2(Q)$$

$$F(Q) = \frac{3V_{\text{core}}(\rho_{\text{core}} - \rho_{\text{shell}})\,\mathrm{j}_1(QR_{\text{core}})}{QR_{\text{core}}} + \frac{3V_{\text{micelle}}(\rho_{\text{shell}} - \rho_{\text{solv}})\,\mathrm{j}_1(QR_{\text{micelle}})}{QR_{\text{micelle}}}$$

where $\mathrm{j}_1(x) = (\sin x + x\cos x)/x^2$, $V_{\text{core}} = \frac{4}{3}\pi R^3_{\text{core}}$, $V_{\text{micelle}} = \frac{4}{3}\pi R^3_{\text{micelle}}$, ρ_{core} = -0.29 x 10^{-6} Å^{-2} for a pure hydrocarbon core, ρ_{solv} = 6.4 x 10^{-6} Å^{-2} for pure D_2O. The only fitting parameters are the radius of the hydrocarbon core (R_{core}) and the shell thickness (t_{shell}) used to calculate the total micelle radius ($R_{\text{micelle}} = R_{\text{core}} + t_{\text{shell}}$). $N_{\text{P}}/V_{\text{tot}}$ is the number of micelles divided by the total sample volume and is calculated from:

$$\frac{N_{\text{P}}}{V_{\text{tot}}} = \frac{\phi_{\text{vol, HC}}}{V_{\text{core}}}$$

where $\phi_{\text{vol, HC}}$ is the volume fraction of hydrocarbon cores in the sample:

$$\phi_{\text{vol, HC}} = \frac{\dfrac{\phi_{\text{m, HC}}}{d_{\text{HC}}}}{\dfrac{\phi_{\text{m, HC}}}{d_{\text{HC}}} + \dfrac{\phi_{\text{m, EO}}}{d_{\text{EO}}} + \dfrac{\phi_{\text{m, solv}}}{d_{\text{solv}}}}$$

where $\phi_{\text{m, HC}}$, $\phi_{\text{m, EO}}$ and $\phi_{\text{m, solv}}$ are the mass fractions in the sample of hydrocarbon tails, EO head groups and D_2O solvent respectively and d_{HC}, d_{EO} and d_{solv} are the densities of the hydrocarbon tails, the EO head groups and D_2O respectively, calculated from bulk densities. The mass fractions where calculated from:

$$\phi_{\text{m, HC}} = \frac{\text{surfactant concentration in wt\%}}{100} \times \frac{\text{Mw}_{\text{tail}}}{\text{Mw}_{\text{surf}}}$$

$$\phi_{\text{m, EO}} = \frac{\text{surfactant concentration in wt\%}}{100} \times \frac{\text{Mw}_{\text{head groups}}}{\text{Mw}_{\text{surf}}}$$

$$\phi_{\text{m, solv}} = 1 - \left(\phi_{\text{m, HC}} + \phi_{\text{m, EO}}\right)$$

where Mw_{tail}, $\text{Mw}_{\text{head groups}}$ and Mw_{surf} are the molecular weights of the tail, the combined head groups and the total surfactant. All values required for calculation are given in Table A.4. ρ_{shell} was calculated from:

$$\rho_{\text{shell}} = \frac{\sum b_{\text{EO}} + n_{\text{D}_2\text{O/EO}} \sum b_{\text{D}_2\text{O}}}{v_{\text{EO}} + n_{\text{D}_2\text{O/EO}} v_{\text{D2O}}}$$

$$\rho_{\text{shell}} = \frac{4.1\times10^{-5} + 1.9\times10^{-4} \times n_{\text{D}_2\text{O/EO}}}{64.7 + 30.0 \times n_{\text{D}_2\text{O/EO}}}$$

where $n_{\text{D2O/EO}}$ was calculated by taking the volume of the shell that was not EO and dividing by the volume of D_2O:

$$n_{\text{D}_2\text{O/EO}} = \left(\left(\frac{V_{\text{shell}}}{N_{\text{agg}} 2m_{\text{EO}}} \right) - v_{\text{EO}} \right) \frac{1}{v_{\text{D}_2\text{O}}}$$

where N_{agg} is the aggregation number, m_{EO} is the number of EOs per surfactant, v_{EO} = 64.7 Å^{-3} and v_{D2O} = 30.0 Å^{-3}. This expression reduces to:

$$n_{\text{D}_2\text{O/EO}} = \left(\left(\frac{V_{\text{tot}}}{V_{\text{core}}} - 1 \right) \frac{v_{\text{tail}}}{2m_{\text{EO}}} - v_{\text{EO}} \right) \frac{1}{v_{\text{D}_2\text{O}}}$$

with the required values for each surfactant given in Table A.4.

Surfactant	**d_{HC} / g.cm^{-3}**	**Mw$_{\text{tail}}$ / g.mol^{-1}**	**Mw$_{\text{surf}}$**	**m_{EO}**	**v_{tail} / Å^3**
Gem$_{12}$E$_{10}$	0.750	420.8	1335.8	10	866.5
Gem$_{12}$E$_{15}$	0.750	420.8	1776.3	15	866.5
Gem$_{14}$E$_{10}$	0.763	476.9	1391.9	10	974.8
Gem$_{14}$E$_{15}$	0.763	476.9	1832.4	15	974.8
Gem$_{20}$E$_{15}$	0.780	645.2	2000.7	15	1299.8
Gem$_{20}$E$_{20}$	0.780	645.2	2441.2	20	1299.8
Gem$_{20}$E$_{30}$	0.780	645.2	3322.2	30	1299.8

Table A.4: Values used for calculation of N_P/V_{tot} and ρ_{shell} for gemini surfactants. d_{HC} was calculated from v_{tail}, which was calculated by extrapolation of densities of liquid hydrocarbons (Figure A.8).

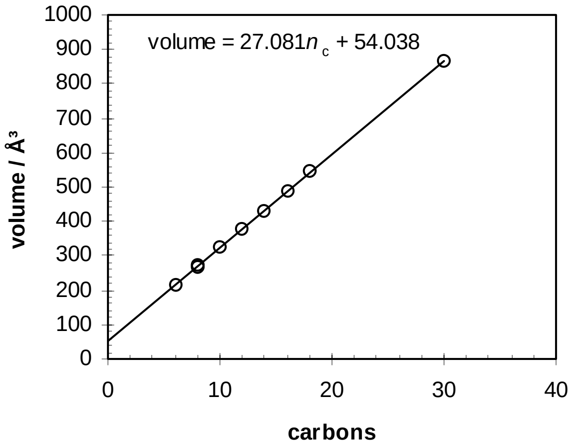

Figure A.9: Extrapolation of volumes from liquid hydrocarbons, calculated from molecular weights and published densities (Table A.5).[144]

Compound	number of carbons	density (g.mol^{-1})	molecular weight	molecular volume (Å^3)
hexane	6	0.659	86.2	217.1
isooctane	8	0.692	114.2	274.1
octane	8	0.703	114.2	269.8
decane	10	0.730	142.3	323.6
dodecane	12	0.750	170.3	377.1
tetradecane	14	0.763	198.4	431.7
hexadecane	16	0.773	226.4	486.4
octadecane	18	0.777	254.5	543.8
squalene	30	0.810	422.8	866.7

Table A.5: Densities and molecular weights used to calculate molecular volumes of hydrocarbons.[144]

Fitting was conducted using modified Igor Pro fitting procedures written by National Institute of Standards and Technology (NIST). Fitting was performed by minimising χ^2, which is defined as

$$\chi^2 = \sum \left(I(Q)_{theory} - I(Q)_{\exp} \right)^2$$

where $I(Q)_{theory}$ and $I(Q)_{\exp}$ are the calculated and experimental scattering values respectively and the sum is over all values of Q. χ^2 is 0 for perfect agreement becoming larger as the fit becomes poorer.

A.11 Determination of Gem$_{20}$E$_m$ Phase Behaviour

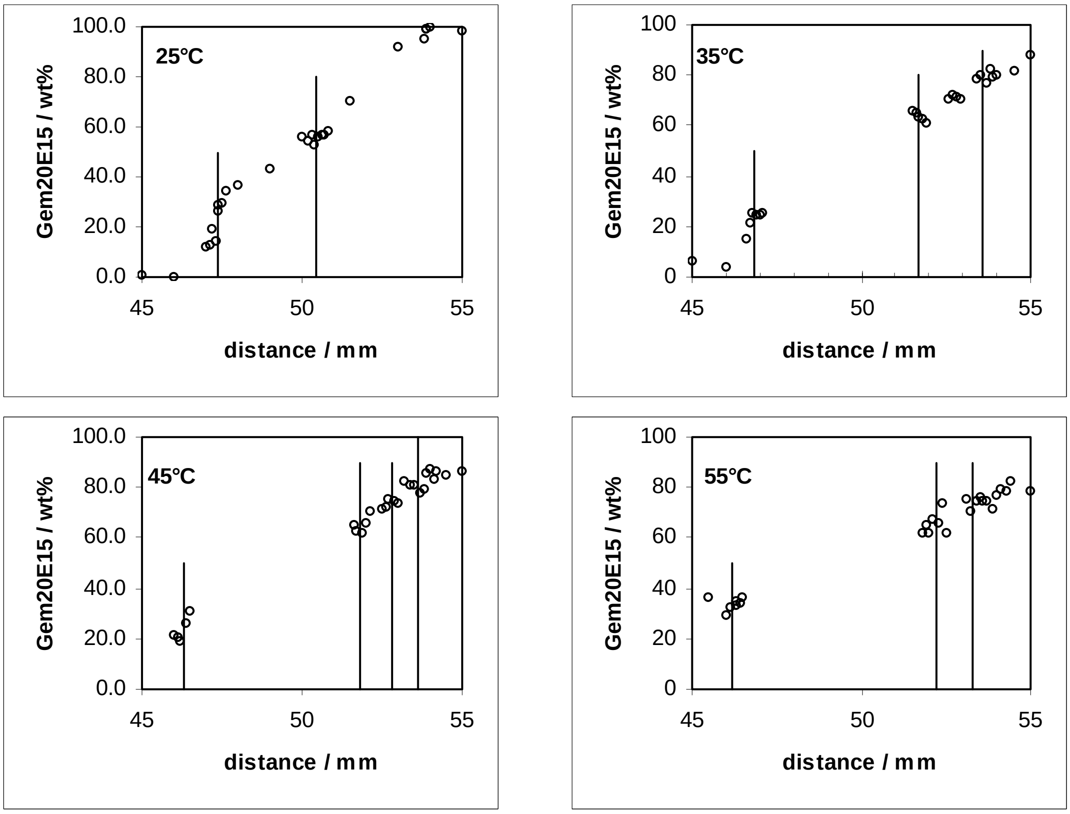

Figure A.10: DIT results for Gem$_{20}$E$_{15}$.

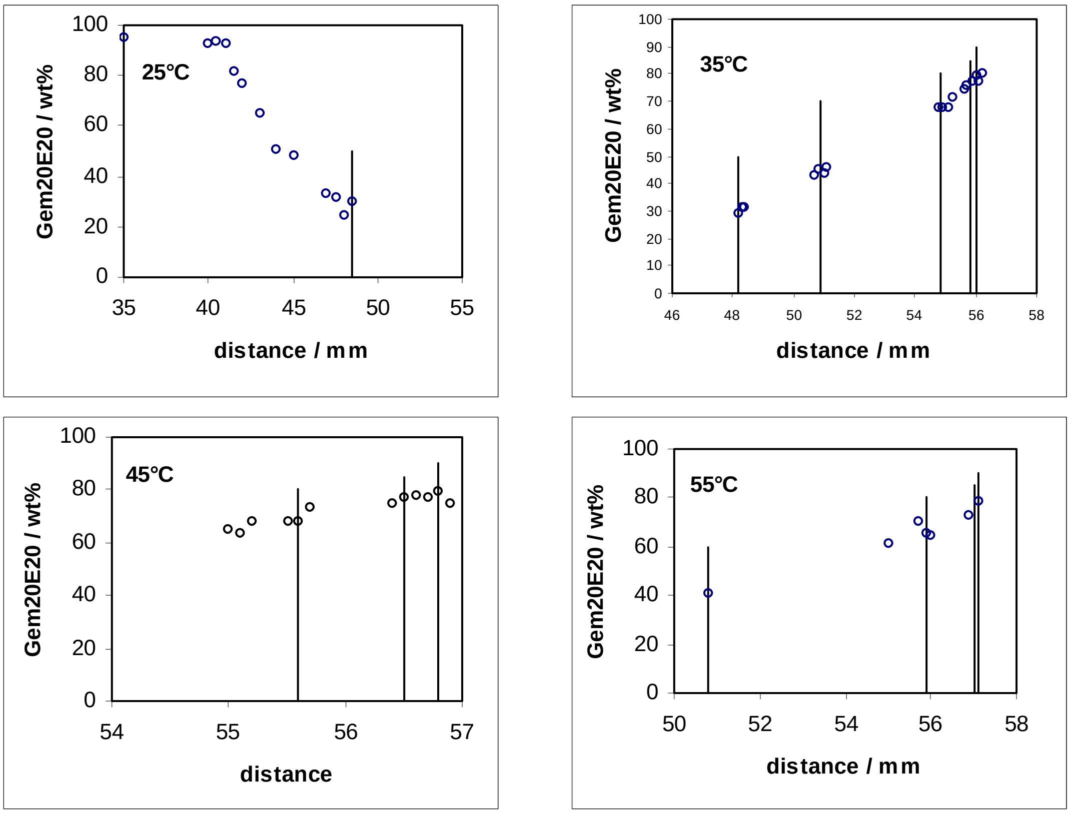

Figure A.11: DIT results for Gem$_{20}$E$_{20}$.

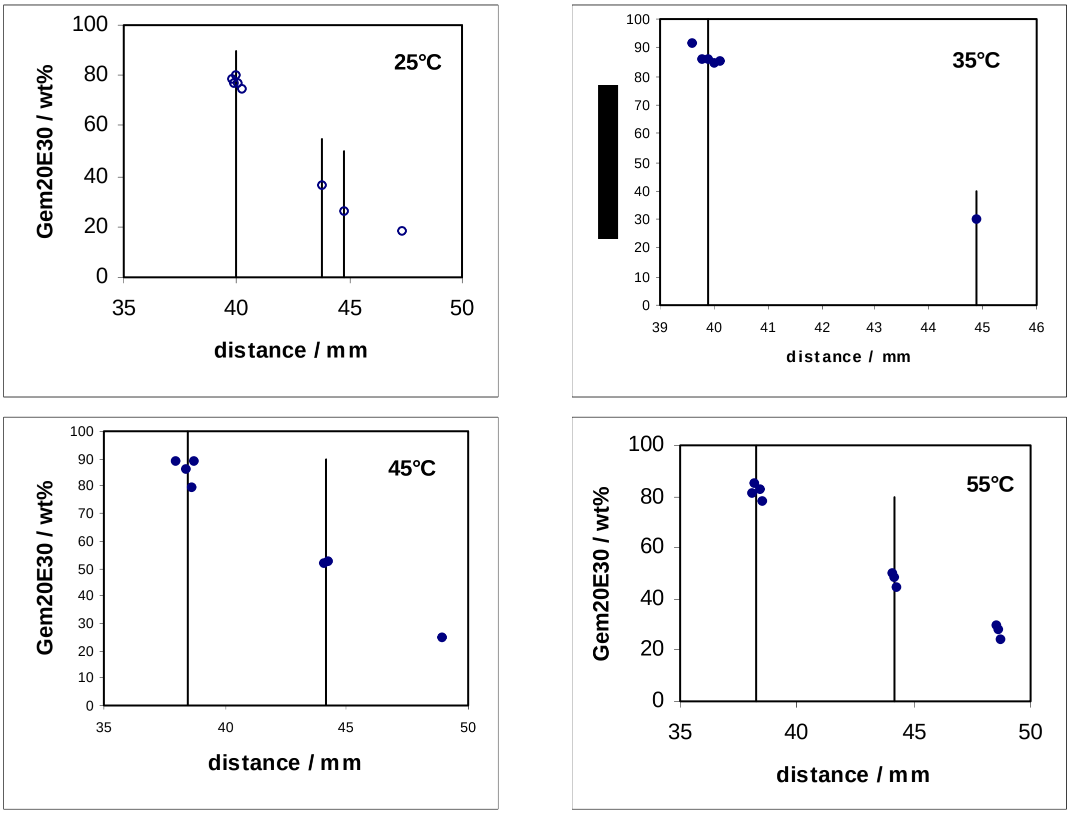

Figure A.12: DIT results for Gem$_{20}$E$_{30}$.

A.12 SANS Data for 1wt% Gemini Surfactants at Elevated Temperatures

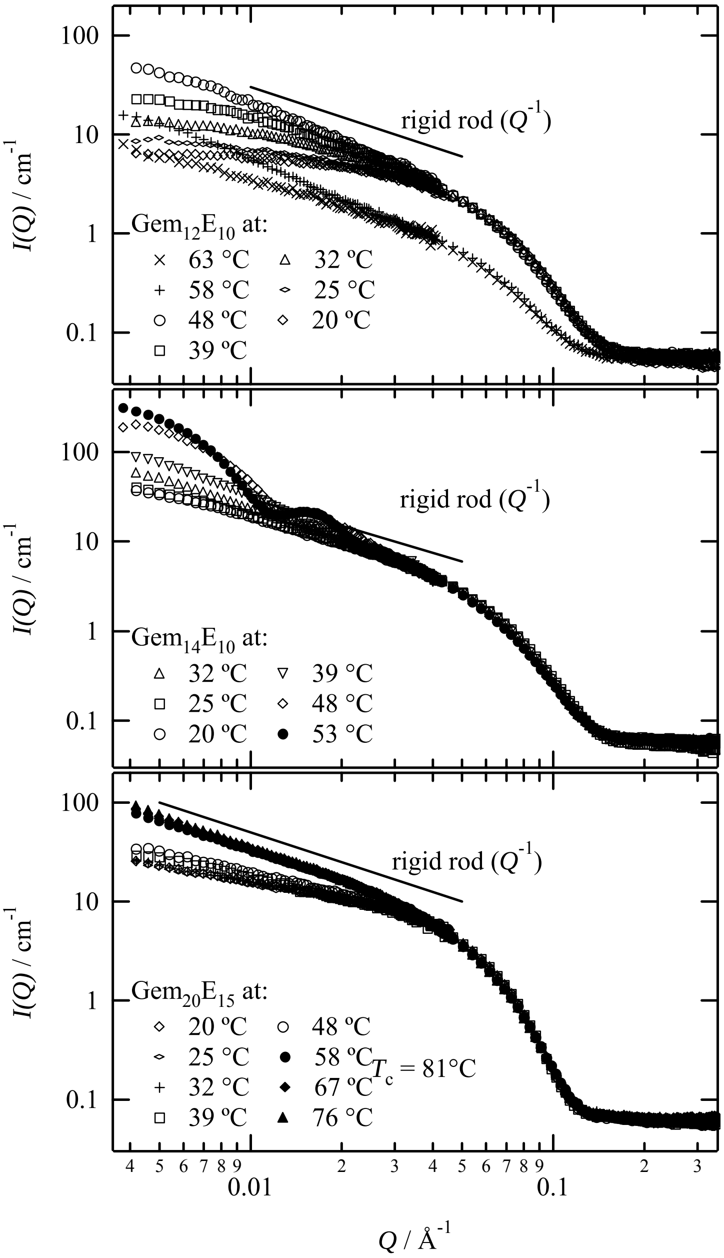

Figure A13: Complete data for 1 wt% $Gem_{12}E_{10}$, $Gem_{14}E_{10}$ and $Gem_{20}E_{15}$ in D_2O.